

NUMERICAL MODELS OF MULTIPHASE FLOWS WITH STICKY PARTICLES

**Doctoral Dissertation by
Nazerke Saparbayeva**

Thesis submitted for
the degree of Philosophiae Doctor (PhD)
in

Computer Science:
Software Engineering, Sensor Networks and Engineering Computing



Department of Mechanical Engineering and Maritime Studies
Faculty of Technology, Environmental and Social Sciences
Western Norway University of Applied Sciences

March 8, 2024

©Nazerke Saparbayeva, 2024

The material in this report is covered by copyright law.

Series of dissertation submitted to
the Faculty of Technology, Environmental and Social Sciences,
Western Norway University of Applied Sciences.

ISBN: 978-82-8461-079-5

Author: Nazerke Saparbayeva

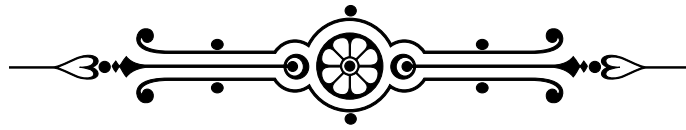
Title: Numerical models of multiphase flows with sticky particles

Printed production:

Molvik Grafisk / Western Norway University of Applied Sciences

Bergen, Norway, 2024

TO MY HERO
Mama, thank you for everything!



PREFACE

The author of this thesis has been employed as a Ph.D. research fellow in the Nanofluids for Energy and Process Technology research group at the Department of Mechanical Engineering and Maritime Studies at Western Norway University of Applied Sciences, Norway.

The research presented in this thesis has been accomplished in cooperation with the Department of Physics and Technology of the University of Bergen, the Energy and Technology division of NORCE, and the SPIN Centre for Chemical Engineering in Mines Saint-Etienne, France.

The author has been enrolled into the PhD program in Computer Science: Software Engineering, Sensor Networks, and Engineering Computing, specializing in Engineering Computing.

This thesis is organized in two parts. Part I is an overview describing the numerical and machine learning methods used and a brief summary of the obtained results. Part II consists of a collection of published and peer-reviewed research articles and submitted papers.

- Paper A** Nazerke Saparbayeva, Pawel Kosinski, Guillaume Dumazer, Marc Fischer, and Boris V. Balakin. Simulation of horizontal hydraulic conveying and dune formation based on CFD-DEM. In AIP Conference Proceedings of ICNAAM 2022 (in press).
- Paper B** Nazerke Saparbayeva, Yu-Fen Chang, Pawel Kosinski, Alex C. Hoffmann, Boris V. Balakin, Pavel G. Struchalin. Cohesive collisions of particles in liquid media studied by CFD-DEM, video tracking, and Positron Emission Particle Tracking. Powder Technology, Elsevier. 426, 118660 (2023)
- Paper C** Nazerke Saparbayeva and Boris V. Balakin. CFD-DEM model of plugging in flow with cohesive particles. Scientific Reports, Nature. 13, 17188 (2023).
- Paper D** Nazerke Saparbayeva, Boris V. Balakin, Pavel G. Struchalin, Talal Rahman and Sergey Alyaev. Application of machine learning to predict blockage in multiphase flow. Submitted to Computation, MDPI.

ACKNOWLEDGMENTS

I am writing these words of gratitude and feel incredibly fortunate. I had everything I needed to enjoy my PhD life over these three years: a passion for my work, supportive colleagues, and the beautiful Bergen with incredible mountains and people!

I would like to express my deep respect for my main scientific supervisor, Professor Boris Balakin. Words cannot express my gratitude for your contribution to my professional development. Under your guidance, I defended my master's thesis, and now I am submitting my doctoral dissertation. I am grateful for your trust in me and your excellent guidance. I would never have taken this step without you as my supervisor. Thank you for this exciting journey into the world of multiphase flows and computational fluid dynamics!

I also want to thank the author of the best book on multiphase flow and my co-supervisor, Professor Pawel Kosinski. Thanks to the rest of the research group members, particularly Dr. Pavel Struchalin, who was responsible for the experimental part of the project during his postdoc. Thank you, Pavel, for the interesting discussions during the experiments and your support. I am also grateful to Professor Alex Hoffman and Yu-Fen Chang for their invaluable contributions to our joint work. Special thanks to my co-supervisor, Sergey Alyaev, Senior Researcher at the Norce Norwegian Research Centre, for providing professional guidance in the machine learning part of the project. I acknowledge the PhD candidate Jon-Thøger Hagen for his help working out the "sammendrag".

I am thankful to the assistant head of the department, Nils Ottar Antonsen, for administrative support and to the PhD program coordinator, Håvard Helstrup, for clear instructions. Also, thanks to Janina Juranek for making the organization of all my international trips much easier.

During spring 2022, I conducted research as a visiting PhD student at Mines Saint-Etienne in France. I'm grateful to Professor Jean-Michel Herri and the entire team at the SPIN Centre. I thank Associate Professors Guillaume Dumazer and Marc Fischer, with whom I worked directly. Thank you for the productive work we accomplished in a short time. Madina Naukanova deserves special thanks for making my stay in Saint-Etienne interesting.

My sincere thanks to my second home in Bergen, the PhD Island, Fabrikkgaten. I was incredibly lucky to work in an office full of positivity. Thanks to my chai team, Amir and Mira, and everyone in room R202-01: Gerard, Aurora & Aika, Nanthini, Keila, Thanh, Daniel aka Danya and Ivan aka Vanya. A big thank you to the entire Fabrikkgaten team. I took the baton from Michele and passed it on to Tim!

Thank you to my family and friends in my hometown, Almaty. Even thousands of kilometres away, I always felt your support, and the time spent with you during the vacations has always energized me.

And finally, thank you to the most important person in my life - my Mom. Thank you for not giving up after our loss 23 years ago and for doing everything for our future. You are everything to us - a mother, a father, a teacher, a doctor, and a best friend. Rakhmet, Mama!

ABSTRACT

Plugging caused by adhesive particles remains an important problem in multiphase fluid dynamics for decades and needs extensive theoretical research. This work aims to investigate this problem using a coupled Computational Fluid Dynamics-Discrete Element Method (CFD-DEM) approach, which allows for detailed tracking of particles and their interactions. The study is methodically divided into four main stages, each corresponding to a research paper.

The initial phase introduces the application of CFD-DEM to simulate the hydraulic transportation of non-cohesive glass beads in a pipe. The simulations were conducted after experimental data using the commercial software Star-CCM+. This step is essential to evaluate how well the model predicts changes in the flow regime and validate these predictions against experimental results.

The primary goal of this research is to simulate plug formation in a multiphase flow with sticky ice particles. Before progressing to this complex stage, the study's second phase focuses on the cohesive collisions of individual particles. For this purpose, sticky ice particles immersed in a subcooled oil phase are simulated. New data on the collisional dissipation of energy and the ice particle coefficient of restitution were obtained using three methods for velocity measurement: high-speed experimental video recording, Positron Emission Particle Tracking (PEPT), and numerical simulations. The cohesive collision process was simulated by considering particle cohesion, size, and shape, providing information on the mechanical properties of particles for the following research steps.

The third stage holds key importance, applying the CFD-DEM model to simulate plugging in a slurry of ice in decane, using the foundational information gained from the previous stages. This part of the research includes a detailed parametric evaluation, focusing on the changes in the flow system's characteristics, particularly the Reynolds number, particle concentration, and surface energy. This section also compares the simulation results with flow maps based on experiments.

Finally, the fourth stage presents the application of a machine learning classifier to predict blockages at a given flow regime, indicating a relatively new and developing approach in this field. A random forest classifier was applied using both experimental and simulation data. Experimental data were obtained from a lab-scale flow loop with ice slurry in decane, and the simulations are based on the CFD-DEM method. The results of this research include a flow regime map with blockage formation boundaries and its changes with variations in cohesion.

This thesis contributes not only to a better understanding of plugging in multiphase flow with sticky particles but also offers practical insights through a CFD-DEM approach. Additionally, it demonstrates the potential of advanced predictive models based on machine learning.

SAMMENDRAG

Proppdannelse forårsaket av kohesive partikler er forblitt et viktig problem i flerfasefluidmekanikk i flere tiår og trenger omfattende teoretisk undersøkelse. Denne avhandlingen har som mål å undersøke proppdannelsen ved hjelp av en kombinert Computational Fluid Dynamics-Discrete Element Method (CFD-DEM), som tillater detaljert sporing av partikler og deres interaksjoner. Avhandlingen er metodisk delt inn i fire hoveddeler, hver tilsvarende en forskningsartikkel.

Den innledende delen introduserer utvikling og bruk av CFD-DEM for å simulere hydraulisk transport av ikke-kohesive glasskuler i et rør. Simuleringene ble utført basert på eksperimentelle data ved hjelp av den kommersielle programvaren Star-CCM+. Dette forsøket er viktig for å vurdere hvor godt modellen forutsier endringer i strømningsregimet og validere disse prediksjoner med eksperimentelle resultater.

Det primære målet med dette doktorgradsprosjektet er å simulere proppdannelsen i en flerfase strømning med kohesive ispartikler. Før man kommer til denne komplekse oppgaven, fokuserer forsøket videre på kollisjoner av individuelle partikler. For dette formålet simuleres kohesive ispartikler nedsenket i en nedkjølt olje. Nye data om kollisjonell dissipasjon av energi og ispartikkelens restitusjonskoeffisient ble oppnådd ved hjelp av tre metoder: høyhastighets videoopptak, Positron Emission Particle Tracking (PEPT), og CFD-DEM simuleringer. Den kohesive kollisjonsprosessen ble simulert ved å vurdere kohesive krefter, størrelse og form, som gir informasjon om partiklenes mekaniske egenskaper for de følgende forsøkene.

Den tredje fasen av stor betydning, har vært å anvende CFD-DEM-modellen for å simulere proppdannelse i en slurry av is i oljen. Dette er gjort ved hjelp av den grunnleggende informasjonen oppnådd fra de foregående stadiene. Denne delen av forskningen inkluderer en detaljert parametrisk evaluering, med fokus på endringer i strømningsystemets egenskaper, spesielt Reynolds-tallet, partikkelkonsentrasjonen og overflateenergien. Denne delen sammenligner også simuleringresultatene med strømningskart basert på eksperimenter.

Til slutt presenterer den fjerde delen anvendelsen av en maskinlæringsklassifikator for å forutsi blokkeringer ved et gitt strømningsregime, noe som indikerer en relativt ny og utviklende metode i flow assurance. En "random forest" - type klassifikator ble opplært ved hjelp av både eksperimentelle- og simuleringdata. Eksperimentelle data ble produsert i en lab-skala strømningsløyfe med isslurry i dekan, og simuleringene er basert på CFD-DEM-metoden. Resultatene av denne forskningen inkluderer et strømningsregimekart med grenser som viser til proppdannelse og beskriver hvordan dette kartet forandres ved endring i kohesive krefter.

Denne avhandlingen bidrar ikke bare til en bedre forståelse av proppdannelsen i flerfasestrømning med kohesive partikler, men tilbyr også praktiske innsikt gjennom CFD-DEM metoden. I tillegg, demonstrerer den potensialet av avanserte prediktive modeller basert på maskinlæring.

Contents

Preface	i
Acknowledgments	iii
Abstract	v
Sammendrag	vii
I OVERVIEW	1
1 Introduction	3
1.1 Methods and challenges	4
1.2 Objectives	6
1.3 Outline	7
2 Multiphase computational fluid dynamics	9
2.1 CFD-DEM method	9
2.2 Model description	10
2.2.1 Continuous phase	10
2.2.2 Dispersed phase	11
2.2.3 Contact model	12
2.2.4 Coefficient of restitution	15
2.3 SIMPLE algorithm	16
2.4 Two-way coupling scheme	17
2.5 Contact detection	18
2.6 Discrete element method collision time scale	20
3 Machine learning application	23
4 Summary of the results	27
4.1 Paper A: Simulation of horizontal hydraulic conveying and dune formation based on CFD-DEM	28
4.2 Paper B: Cohesive collisions of particles in liquid media studied by CFD-DEM, video tracking, and Positron Emission Particle Tracking	29
4.3 Paper C: CFD-DEM model of plugging in flow with cohesive particles	30
4.4 Paper D: Application of machine learning to predict blockage in multi-phase flow	31

5	Efficiency and applicability of the CFD-DEM model	33
5.1	Notes on computational costs	33
5.2	Applicability of different multiphase CFD methods	34
5.2.1	Eulerian-Eulerian approach	34
5.2.2	Comparative analysis	35
6	Conclusions and Future Work	39
	Bibliography	41
II	ARTICLES	47
Paper A:	Simulation of horizontal hydraulic conveying and dune formation based on CFD-DEM	49
Paper B:	Cohesive collisions of particles in liquid media studied by CFD-DEM, video tracking, and Positron Emission Particle Tracking	57
Paper C:	CFD-DEM model of plugging in flow with cohesive particles	71
Paper D:	Application of machine learning to predict blockage in multiphase flow	83

Part I

OVERVIEW

INTRODUCTION

The issue of plugging in multiphase flow systems with adhesive particles presents a significant challenge for industrial pipelines. The problem arises from multiple contributing factors, including interactions inside the particulate phase, particle-wall collisions, and complex interactions between different phases of the transported medium. These combined factors can lead to deposit formation and prevent the smooth movement of liquids, impacting both fluid flow dynamics and the operational efficiency of the systems. The cohesive nature of particles increases their tendency to adhere to surfaces, leading to agglomeration and plug formation. This could completely block the system in critical scenarios, leading to substantial financial losses. Only the oil and gas industry spends over \$200 millions annually to prevent plug formation and maintain smooth operations [1].

In oil and gas production, the presence of hydrates, paraffin, asphaltenes, or sand can lead to severe plugging issues in pipelines. Hydrate formation in subsea pipelines remains a major flow assurance challenge today. In addition to mechanical pigging, there are different available solutions for this case. In Norway, methanol or monoethylene glycol are frequently used inhibitors to change hydrate formation conditions by increasing temperature and pressure thresholds. Other options include insulation, heating (limited by length), and low-dosage hydrate inhibitors effective at low concentrations but less efficient at lower temperatures [2]. However, such control strategies can be very expensive. For example, the insulation of subsea pipelines to prevent hydrate formation during offshore operations costs about \$1 million per mile [3]. Interestingly, the industry has shifted focus from completely preventing hydrate formation to managing hydrate slurry transport. This approach enables hydrate formation but as a transportable solid suspension. With ongoing projects, Sintef, Equinor, Chevron [4], Schlumberger [5], and other companies are actively involved in this topic.

Paraffin deposition is also a common problem, where sticky wax-like substances solidify and adhere to pipeline walls. Wax deposition blockages are recognized as a billion-dollar problem in the oil and gas sector, with annual economic impacts ranging from \$14.74 to \$330.59 billion [6]. Moreover, this issue is also relevant in sand production, especially in reservoirs characterized by weak and unconsolidated sandstone. In extreme cases, a high sand influx can abruptly clog or shut down the well [7].

This problem extends beyond the oil and gas industry, where sticky particles present

Introduction

blockage challenges. These fields include medicine, chemicals, and food production, among others.

In the medical sector, particularly in hemodynamics, conditions like thrombosis, involving blood clots formed by adhesive platelets, present big concerns, obstructing blood vessels and leading to health complications including stroke, heart infarction, pulmonary embolism, etc. [8]. According to the World Health Organization report, stroke stands as the second leading cause of death, responsible for approximately 11% of total deaths [9]. In pharmaceutical manufacturing, solid particles can agglomerate and cause blockages in processing equipment. Tubes in these systems often get blocked by particles sticking to the walls or forming crystals [10]. Similarly, in consumer products manufacturing, adhesive materials or particles in adhesives, coatings, or formulations can disrupt the production line, necessitating thorough equipment cleaning, preventive maintenance, and material reformulation for smoother operations. Moreover, the blockage caused by sticky interactions is relevant to the food processing field [11].

The chemical industry faces plugging challenges due to the deposition of various adhesive particles inside pipelines and reactors, such as polymers, resins, or solid products. These particles agglomerate and adhere to surfaces, leading to reduced flow rates, equipment damage, and production interruptions. Furthermore, sticky ore particles or mineral slurries in mining operations can agglomerate and cause blockages in transportation systems, affecting the efficiency of mineral extraction and processing. Solutions for the aforementioned cases might involve advanced filtration systems, anti-fouling agents, and high-pressure flushing methods [12].

In water treatment facilities, the accumulation of biofilms, sediments, or precipitates on surfaces can lead to clogging in pipes and filtration systems [13]. These blockages affect water flow and purification processes. In wastewater treatment, sticky substances such as grease or oils can clog pipes and filtration systems, demanding specialized treatment methods and filtration systems to prevent blockages and maintain operational efficiency [14].

1.1 Methods and challenges

Across these diverse sectors, early detection of potential blockage events enables timely preventive measures, reducing mortality, risk of system shutdowns, equipment damage, and financial losses. These predictive methods support informed decision-making and the formulation of efficient strategies. Hence, it is important to study this complex process fundamentally and experimental studies play a crucial role as the foundation for predictive methods.

Experiments or pilot studies can verify the accuracy of risk-assessing models and refine their parameters for real-world application. In particular, flow loop-based experiments are essential for understanding multiphase flow as they recreate real conditions, enabling observation of phase interactions, flow behaviour, and material performance. A series of studies are dedicated to examining the transport and agglomeration of hydrate slurry using flow loops. Work by Vijayamohan et al. [15] presents a flow loop study of the gas hydrate formation and transportability in water-continuous and partially dispersed systems. Similarly, Majid et al. [16] used a high-pressure flow loop to study gas hydrate formation and plugging under different

conditions. A high-pressure flow loop to study hydrate slurry rheology was also utilized by Ding et al. [17]. Moreover, different methods are also employed to study slurry transport. For example, a transparent pipe was used to visualize the flow of isothermal ice slurry in the study by Bordet et al. [18]. Hirochi et al. [19] used a tube orifice to study the ice-particle/water slurry blockage, examining threshold values of velocity and ice fraction for blockage. The range of experimental studies discussed and other experimental works [20] in this field provides valuable insights into various critical physical aspects of the process. However, experiments in this area usually struggle to capture all the fine details of the processes and accurately recreate real-world conditions.

Multiphase flow simulators are powerful tools that can be used to prevent and mitigate pipe plugging problems with the ability to analyze and optimize the operation of multiphase flow systems. The multiphase flow simulators OLGA [5] and LedaFlow [21] are two of the most popular simulators available. The OLGA dynamic multiphase flow simulator was developed by Schlumberger and can assist in mitigating flow assurance challenges such as hydrate formation, wax deposition, and sand erosion, which can affect the efficiency and safety of production systems. Similarly, LedaFlow is highly regarded for its ability to simulate and predict transient multiphase flow phenomena, such as hydrate formation, wax deposition, and other flow assurance issues. In order to use simulators, it is necessary to provide information about the geometry of the system, the properties of the phases, the operating conditions, and the desired outcome. The simulation results can be useful in taking steps to prevent or mitigate the blockage. They are both based on fundamental principles of fluid dynamics to predict and analyze the behaviour of multiphase flow and, consequently, flow assurance issues.

CFD (Computational Fluid Dynamics) is key in complementing experimental studies, enabling the visualization and analysis of complex flow patterns, and predicting potential agglomeration areas. Additionally, CFD models can help optimize system designs by exploring various parameters without the cost and limitations of physical experiments. Numerical models, highlighted in works by Eskin et al. [22] and Labois et al. [23], focus on predicting the deposition of substances like asphaltenes and hydrates in pipelines. In their study, Rukhlenko et al. [24] demonstrate CFD's capability to model phenomena like blood coagulation and particle flow modes, showcasing the diverse applications of this technique in understanding blockage mechanisms. Furthermore, studies by Yang et al. [25] and Ma et al. [26] provide details on modelling particle plugging, considering how different particles interact and potentially lead to blockages. Flow simulators and CFD have proven effective for predicting model depositions and analyzing pressure gradients, but their application in accurately modelling plugging phenomena requires further exploration.

By employing coupled simulations CFD-DEM (Discrete Element Method), it is possible to provide a better understanding of hydrodynamic bridging, pore blockage, and orifice jamming, as highlighted in studies by Mondal et al. [27], Shao et al. [28] and Xu et al. [29]. Moreover, specific to hydrate blockage prevention, studies by Duan et al. [30] and Wang et al. [31] utilize CFD-DEM methods to simulate the hydrate blockage process, considering factors such as system characteristics and diameter reduction in pipes. These simulations aid in understanding the deposition and accumulation

Introduction

of hydrate particles, thus contributing to strategies to prevent blockages in pipeline systems handling hydrate slurry.

Flow regime maps, based on system conditions such as flow rate, viscosity, and density of the phases, provide a graphical representation of the different flow patterns that can occur in a pipeline. These maps are crucial for predicting the conditions under which various flow regimes, such as stratified, slug, or annular flow, might occur, aiding in preventing blockages. Flow regime maps can be used in system design to enhance safety and efficiency.

Machine learning algorithms have become instrumental in predicting and managing various aspects of multiphase flow systems, particularly in understanding multiphase flow regimes. For instance, studies by Manikonda et al. [32] and Alhashem [33] demonstrate the use of machine learning classification algorithms to identify different gas-liquid flow regimes. These algorithms analyze flow patterns and characteristics, aiding in the real-time identification and classification of flow regimes in pipelines. Similarly, research by Chaari et al. [34] presents an optimized artificial neural network model for estimating steady-state liquid holdup, contributing to a better understanding of flow behaviour. Furthermore, the works by Qin et al. [35] and Wang et al. [36] utilize machine learning models to predict gas hydrate plugging risks and understand blockage mechanisms due to hydrate formation in transmission pipelines. These models use flow loop data and field observations, providing insights into potential blockage occurrences.

In addition, the research of Kim et al. [37], and Amar et al. [38] focus on machine learning-based models to predict wax deposition in oil pipelines. These models aim to predict the location and quantity of wax deposition. Ahmadi's [39] work highlights data-driven approaches for predicting wax deposition, emphasizing the role of ML techniques in understanding and managing deposition risks in energy systems. Overall, these works collectively demonstrate the increasing utilization of machine learning algorithms in predicting multiphase flow behaviours and identifying flow regimes. However, using machine learning algorithms to solve blockage-related issues is relatively rare in research. The machine learning models developed require specialized training sets and are suited to specific system contexts, limiting their universal application. For instance, a model for flow loops may not adapt well to hemodynamics.

1.2 Objectives

Despite numerous studies on cohesive agglomeration, a comprehensive understanding of how sticky particles contribute to blockage processes remains lacking. This project aims to improve this understanding by applying the CFD-DEM technique to simulate the plugging process in multiphase flow.

The project's objectives can be divided into the following points.

Objective 1

The first goal of this research is to build a CFD-DEM model for a basic case study before considering a more complex process of plugging with adhesive particles. To

achieve this, simulate a case with hydraulic conveying involving glass bead particles using the CFD-DEM model. This step aims to evaluate the model's capacity to accurately represent transitional flow regimes, such as dune flow, as a fundamental step toward understanding particulate behaviour in various flow conditions.

Objective 2

This stage introduces cohesive interactions into the CFD-DEM model and simulates cohesive interactions of ice particles in an oil phase. The model is then validated using experimental videos and Positron Emission Particle Tracking [40]. This provides essential details for the subsequent modelling of the entire flow in a similar medium, representing the project's next objective.

Objective 3

Having covered the first two objectives, the project's main goal is to simulate the plugging process in multiphase flow using the CFD-DEM method. Specifically, simulation of ice slurry in decane in the flow loop test section and validating the data against experimental results.

Objective

The final goal is to apply a machine learning classifier to predict blockages using experimental flow loop data and CFD-DEM modelling data. Additionally, the aim is to construct a flow map with a blockage boundary for a specific concentration range.

1.3 Outline

The thesis is divided into two main parts: the overview and the articles. The overview section includes six main chapters. Following the introductory chapter, the second chapter focuses on the physical principles related to the research. It discusses the chosen method, model description with equations, and numerical algorithms.

The third chapter describes the machine learning part, explicitly discussing the application of the random forest classifier. The fourth chapter summarizes the results of four papers. The fifth section covers computational analysis, focusing on computational time and methodology comparison. The overview part concludes with a sixth chapter on conclusions and future work.

The second part of the thesis presents the full articles from A to D, which are referenced in the summary of the results.

MULTIPHASE COMPUTATIONAL FLUID DYNAMICS

This chapter is an important starting point for fully understanding the construction of models and their fundamental principles.

Initially, the chapter presents the model description, introducing core concepts like contact force and restitution coefficient through governing equations. The subsequent section explains algorithms used, like SIMPLE (Semi-Implicit Method for Pressure-linked Equations) algorithm and the two-way coupling scheme. Contact detection and the discrete element method particle time scale are also considered in the final sections of this chapter.

2.1 CFD-DEM method

The Computational Fluid Dynamics-Discrete Element Method (CFD-DEM) approach combines Eulerian-Lagrangian methodologies because of their advantages in simulating multiphase flows with particles compared to the other methods. CFD-DEM's clear advantage is its detailed treatment of particles as discrete objects compared to other multiphase modelling methods. Consequently, compared to the Eulerian-Eulerian approach, CFD-DEM offers a more detailed description of particulate flows.

The CFD-DEM method unites the advantages of both CFD and DEM. CFD, which solves the Navier-Stokes equations, provides a detailed representation of fluid flow dynamics. On the other hand, DEM simulates the motion and interaction of individual particles based on Newton's laws of motion and contact mechanics. By integrating these two methods, CFD-DEM can simultaneously handle the fluid flow and particle dynamics in parallel.

An essential feature of CFD-DEM is the two-way coupling between the fluid and solid phases, allowing for an exchange of information where the fluid's impact on particles and vice versa are continuously updated and integrated into the simulation through calculating drag forces, momentum transfer, and other interactions at each time step. It allows the model to adjust as the simulation progresses dynamically [41].

The iterative process of the simulation continues with time-stepping, where both fluid dynamics and particle movements are updated until the solution converges or reaches the desired simulation finale. Post-processing then allows the analysis and visualization of the complex dynamics of fluid-particle interactions. This combination

of CFD and DEM provides detailed and accurate modelling of complex multiphase flows, making CFD-DEM a powerful method in this research area.

Below is a detailed method description with governing equations that explains all the parameters for simulating different cases presented in the research papers.

2.2 Model description

2.2.1 Continuous phase

The continuous phase in this research framework is analyzed using a system of Navier-Stokes equations that are averaged over the volume of the fluid. These equations are used to model unsteady, isothermal, and incompressible flow.

$$\frac{D\phi}{Dt} = 0, \quad (2.1)$$

where ϕ represents the volume fraction of the continuous phase, and D/Dt is the substantial derivative. The volume fraction is calculated as $1 - V_p/V_c$, where V_p is the total volume of particles in a computational cell and V_c is the volume of the computational cell.

The momentum equation [42]:

$$\frac{D(\rho\phi\vec{u})}{Dt} = -\phi\nabla p + \phi(\mu + \mu^t)\nabla^2\vec{u} + \phi\rho\vec{g} - \vec{F}_p, \quad (2.2)$$

where \vec{u} represents the velocity of the continuous phase, ρ signifies the density of the continuous phase, p denotes the pressure, μ and μ^t refer to the molecular and turbulent viscosity, and \vec{g} stands for the acceleration due to gravity. The collective influence of the inter-phase forces exerted by particles in the continuous phase is summarized by the vector \vec{F}_p scaled with the volume of the computational cell.

The standard k - ϵ turbulence model calculates turbulent viscosity. This means that for turbulent cases in the momentum equation, the turbulent viscosity term μ^t depends on two additional scalars k (turbulent kinetic energy) and ϵ (turbulent energy dissipation rate), that are introduced in two additional transport equations. Consequently, the governing equations would be simplified for laminar flow by removing the terms related to turbulent viscosity μ^t .

The turbulent viscosity concept accounts for the turbulent flow behaviour in an average form. The parameter is given by the proportionality between the turbulent kinetic energy k and the dissipation rate of turbulent energy ϵ [43]:

$$\mu_t = 0.09\rho k \cdot \max\{k/\epsilon, \sqrt{\mu/\rho\epsilon}\}, \quad (2.3)$$

The transport equations for k and ϵ are given as [43]:

$$\frac{D(\rho k)}{Dt} = \nabla \cdot ((\mu + \mu^t/\sigma_k)\nabla k) + P_k, \quad (2.4)$$

$$\frac{D(\rho\epsilon)}{Dt} = \nabla \cdot ((\mu + \mu^t/\sigma_\epsilon)\nabla\epsilon) + 1.44\frac{\epsilon}{k}P_\epsilon - 1.92\rho(\epsilon^2/k + \epsilon_0/T_0) \quad (2.5)$$

where P_k and P_ϵ are the production and dissipation terms, ϵ_0 is the turbulent dissipation at ambient conditions, $T_0 = \max\{k_0/\epsilon_0, \sqrt{\mu/\rho\epsilon_0}\}$, $\sigma_k=1$, and $\sigma_\epsilon=1.3$. It is important to note that, in the multiphase CFD model, terms in Equations 2.4-2.5 should be scaled with the volume fraction of the continuous phase ϕ . However, this parameter is reduced for the simplified notation presented in the thesis.

2.2.2 Dispersed phase

Newton's second law describes the linear movement of discrete objects [42]:

$$m_i \frac{d\vec{v}_i}{dt} = \vec{f}_{p,i} + \vec{f}_{ls,i} + \vec{f}_{\Sigma,i} + m_i \vec{g} + \vec{f}_{b,i} + \sum_{j=1,N} \vec{F}_{i,j}, \quad (2.6)$$

where m_i is the mass of the particle and \vec{v}_i is the particle velocity. The right-hand side of Equation 2.6 includes the buoyancy $\vec{f}_{b,i}$, the strongest inter-phase momentum coupling terms represented by the drag force \vec{f}_p , the Saffman lift force \vec{f}_{ls} , and the rest of the forces applied from the fluid to the particles \vec{f}_Σ . They may include the virtual mass force accounting for the additional resistance a particle experiences when it accelerates in a fluid. As it accelerates, the continuous phase around the particle is also agitated. The interaction with the moving fluid increases the resistance faced by the particle, which requires additional force. It is also known as added mass [44]. This force plays a rather minor role in the problems the thesis considers and is not covered in great detail. More information on this term is given in e.g. [44, 45]. Another example of \vec{f}_Σ is the Magnus lift force [45] applied to intensively rotating objects immersed in the continuous phase. Finally, $\vec{F}_{i,j}$ refer to the interactions affecting the i^{th} particle due to its contact with N particles and solid walls [46].

The rotational motion of an individual particle is described as follows [46]:

$$\frac{d}{dt}(I_i \vec{\omega}_{p,i}) = \sum_k \vec{T}_{i,k}, \quad (2.7)$$

where I is the moment of inertia of the particle, $\vec{\omega}_p$ is the angular velocity of the particle rotation, and \vec{T} is the torque given by the forces from the right-hand-side of Equation 2.6.

This section presents the most frequently used expressions for the major inter-phase momentum coupling terms below. The classical expression for the drag force reads as [45]:

$$\vec{f}_{p,i} = \frac{\pi}{2} r_i^2 c_{D,i} \rho (\vec{u} - \vec{v}_i) |\vec{u} - \vec{v}_i|, \quad (2.8)$$

where $c_{D,i}$ is the drag coefficient, and $r=1/2d_p$. This coefficient is, in many cases, determined using the Schiller-Naumann's expression [45]:

$$c_{D,i} = \begin{cases} (24/\text{Re}_{p,i}) \cdot (1 + 0.15\text{Re}_{p,i}^{0.687}) & \text{Re}_{p,i} \leq 10^3 \\ 0.44 & \text{Re}_{p,i} > 10^3, \end{cases} \quad (2.9)$$

where $\text{Re}_p = 2\rho|\vec{u} - \vec{v}_i|r_i/\mu$ is the particle Reynolds number.

The model for the Magnus lift force determines the force for the case of a spinning particle as it moves through a fluid. The particle's rotation creates a difference in velocity between the fluid on one side of the particle and the fluid on the other. Because of this velocity difference, there is a corresponding difference in pressure, leading to a force that acts perpendicular to the direction of motion and the axis of rotation [44]:

$$\vec{f}_{lr,i} = 1/2\rho\pi r_i^2 c_{lr} |\vec{u} - \vec{v}_i| \frac{\vec{\Omega}_i \times (\vec{u} - \vec{v}_i)}{|\vec{\Omega}_i|}, \quad (2.10)$$

where $\vec{\Omega}_i$ represents the angular velocity of the particle relative to the fluid as follows [45]:

$$\vec{\Omega}_i = 1/2\nabla \times \vec{u} - \vec{\omega}_{p,i}, \quad (2.11)$$

The respective force coefficient $c_{lr,i}$ is given as [47]:

$$c_{lr,i} = 0.45 + \left(\frac{\text{Re}_{R,i}}{\text{Re}_{p,i}} - 0.45 \right) \exp(-0.5684 \text{Re}_{R,i}^{0.4} \text{Re}_{p,i}^{0.3}), \quad (2.12)$$

with $\text{Re}_{R,i} = 4\rho r_i^2 |\vec{\Omega}_i| / \mu$.

The Saffman force, also called the shear lift force, is relevant for a particle moving relative to a fluid when there is a perpendicular velocity gradient in the fluid to the direction of the particle's movement. This force is calculated as follows:

$$\vec{f}_{ls,i} = c_{ls} \rho \pi r_i^3 (\vec{u} - \vec{v}_i) \times \vec{\omega}_i, \quad (2.13)$$

where $\vec{\omega}_i = \nabla \times \vec{u}$ is the curl of the fluid velocity and c_{ls} is the lift coefficient [47]:

$$c_{ls,i} = \frac{4.1126}{\text{Re}_{s,i}^{0.5}} f_i(\text{Re}_{p,i}, \text{Re}_{sl,i}), \quad (2.14)$$

where $\text{Re}_{sl,i} = 4\rho r_i^2 |\vec{\omega}_i| / \mu$ is the Reynolds number for the shear flow, and function f is computed as [43]:

$$f_i = \begin{cases} (1 - 0.3314\beta^{0.5}) e^{-0.1\text{Re}_{p,i}} + 0.3314\beta^{0.5} & \text{Re}_{p,i} \leq 40 \\ 0.0524 (\beta \text{Re}_{p,i})^{0.5} & \text{Re}_{p,i} > 40, \end{cases} \quad (2.15)$$

where $\beta = 0.5\text{Re}_{sl,i} / \text{Re}_{p,i}$.

2.2.3 Contact model

The Hertz-Mindlin contact model proposes a helpful technique for problems in contact mechanics. The model, illustrated in Figure 2.1, describes the elastic behaviour of particles and computes the resulting deformations of particles in contact. This model clarifies how the contact zone behaves, how the contact forces are distributed, and the dynamics of deformations. The Hertz-Mindlin contact model calculates the contact forces in normal (denoted n) and tangential (denoted t) directions relative to the contact plane between the objects. The model assumes that the particles deform and overlap

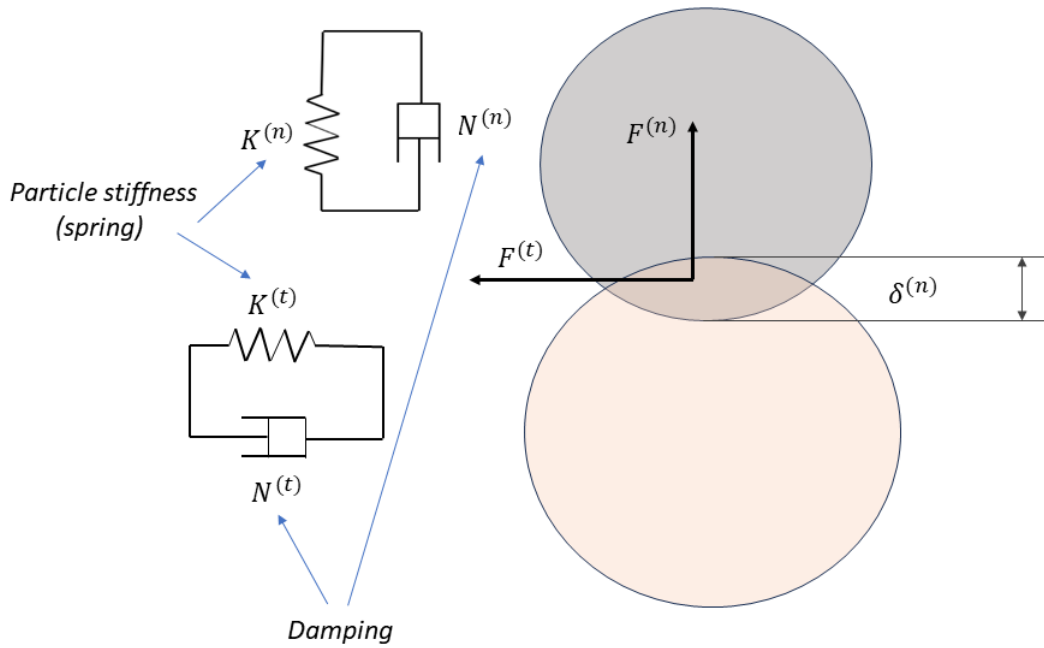


Fig. 2.1: Schematic description of Hertz-Mindlin contact model for two colliding particles.

upon the collision and resist the deformation following two mechanisms: the "spring" resistance proportional to the deformation and the "dashpot" resistance dependent on deformation dynamics.

The contact forces are computed as [43, 48]:

$$\vec{F}_{i,j} = F_{i,j}^{(n)} \vec{n} + F_{i,j}^{(t)} \vec{t}. \quad (2.16)$$

The normal component of the force [43]:

$$F_{i,j}^{(n)} = -K^{(n)}\delta^{(n)} - N^{(n)}v_{r,i}^{(n)}, \quad (2.17)$$

where $\delta^{(n)}$ is the particle-to-wall overlap distance, v_r is the relative velocity between the particle centres, $K^{(n)}$ is the "spring's" stiffness in the normal direction employed in the soft-sphere approach. It is dependent on $\delta^{(n)}$ as:

$$K^{(n)} = \frac{4}{3}E_e\sqrt{r_{e,i}\delta^{(n)}}, \quad (2.18)$$

where E_e is the equivalent of Young's modulus [43] dependent on the Poisson ratio ν_i of the particles, and r_e is the equivalent radius of the particles. $N^{(n)}$ is the damping

coefficient in the normal direction [43]:

$$N^{(n)} = \sqrt{5K^{(n)}m_{e,i}} \frac{-\ln(\epsilon_{(n)})}{\sqrt{\pi^2 + (\ln \epsilon_{(n)})^2}}, \quad (2.19)$$

where $\epsilon_{(n)}$ is the coefficient of the particle material restitution in the normal direction, and m_e is the equivalent mass of the particles. To account for the cohesive interactions, the cohesive force may be added on the right-hand side of Equation 2.17. The force is often expressed using the Johnson-Kendall-Roberts (JKR) model [49]. Developed by Johnson, Kendall, and Roberts in 1971, this model is a theoretical approach to describe the contact mechanics of elastic bodies with cohesion and adhesion. It describes how elastic particles stick together, considering their elasticity and surface energy. The JKR model calculates the contact area and the adhesion force, making it useful for studying materials with elastic deformation at the contact point [43]:

$$F_c = 3/2 \cdot \pi r_{c,i} W, \quad (2.20)$$

where r_c is the minimum radius of the contact surface, and W is the work of cohesion. In this thesis, the cohesion work values at various experimental temperatures were obtained from the research by Yang et al. [50]. It is important to note that F_c in the Hertz-Mindlin contact model equation will be absent for the non-cohesive cases.

The tangential component of the contact force is computed as [43]:

$$F_{i,j}^{(t)} = -K^{(t)}\delta^{(t)} - N^{(t)}v_{r,i}^{(t)} \quad (2.21)$$

The stiffness coefficient in the tangential direction [43]:

$$K^{(t)} = 8G_e\sqrt{r_{e,i}\delta^{(n)}}, \quad (2.22)$$

with the equivalent shear modulus G_e .

$N^{(t)}$ is the damping coefficient in the tangential direction:

$$N^{(t)} = \sqrt{5K^{(t)}m_{e,i}} \frac{-\ln(\epsilon_{(t)})}{\sqrt{\pi^2 + (\ln \epsilon_{(t)})^2}}, \quad (2.23)$$

where $\epsilon_{(t)}$ is the particle restitution coefficient in the tangential direction.

In case $|K^{(t)}\delta^{(t)}| \geq f_s|K^{(n)}\delta^{(n)}|$, the tangential component comes above the sliding limit, a constant $F^{(t)}$ applies as follows:

$$F^{(t)} = -f_s|K^{(n)}\delta^{(n)}|\text{sign}\left(v_{r,i}^{(t)}\right), \quad (2.24)$$

where f_s is the Coulomb friction coefficient.

The final element of the model involves rolling resistance μ_r , which contributes a resisting torque as shown in Equation 2.7:

$$\vec{T}_{i,j}^r = -r_{e,i}\mu_r F_{i,j}^{(n)} \frac{\vec{\omega}_{r,i}}{|\vec{\omega}_{r,i}|}, \quad (2.25)$$

where ω_r is the relative angular velocity. It is to be noted that the equivalent size r_e and mass m_e of the particles turn to their actual parameters r and m for collisions with walls, which are considered as objects with infinite mass and curvature [43]. In other cases, the equivalent properties for the collision of particles 1 and 2 are defined as:

$$r_e = \frac{r_1 \cdot r_2}{r_1 + r_2} \quad (2.26)$$

$$m_e = \frac{m_1 \cdot m_2}{m_1 + m_2} \quad (2.27)$$

$$E_e = \left(\frac{1 - \nu_1^2}{E_1} + \frac{1 - \nu_2^2}{E_2} \right)^{-1}, \quad (2.28)$$

where E is the Young's modulus of the particle.

$$G_e = \left(\frac{(2 - \nu_1)(1 + \nu_1)}{E_1} + \frac{(2 - \nu_2)(1 + \nu_2)}{E_2} \right)^{-1} \quad (2.29)$$

2.2.4 Coefficient of restitution

The coefficient of restitution characterizes an energy share that is conserved in a particulate collision [44]. As shown in Fig 2.2 it compares the velocity of an object after it bounces off a surface v_1 (the rebound velocity) to the velocity it had before the impact v_0 (the approach velocity). A simplified definition valid for low particle velocities follows below:

$$\epsilon = -\frac{v_1}{v_0}. \quad (2.30)$$

For perfectly elastic collisions, where energy is completely conserved, the coefficient is 1, meaning the object bounces back with the same velocity as it hits the surface. However, some energy is lost due to the deformation of particles, resulting in a coefficient between 0 (no bounce back) and 1. The coefficient can vary depending on the materials involved and the impact angle.

The method devised by Joseph et al. [51] was applied to account for lubrication forces present in the continuous phase when the particles are about to touch each other. It is based on a reduction of the coefficient of restitution (COR) for wet particles based on the COR observed under "dry" conditions (in air or vacuum) and accounting for the viscous dissipation [45] in a fluid gap between the colliding particles:

$$\epsilon_{(n)} = \epsilon_{(n),dry} + \frac{1 + \epsilon_{(n),dry}}{St_0} \ln \frac{x_c}{x_0}, \quad (2.31)$$

where $St_0 = m_{e,i} v_i / 6\pi\mu r_{e,i}^2$ is the particle Stokes number before contact. The ratio of the inter-particle distance at the point of contact, x_c , to the terminal position outside the lubrication force range, x_0 , is typically around 10^{-3} [52]. Following the approach by Reitter et al. [53], we propose that the coefficient of restitution in the tangential direction remains largely unaffected by lubrication, thus $\epsilon_{(t)} = \epsilon_{(t),dry}$. In this work,

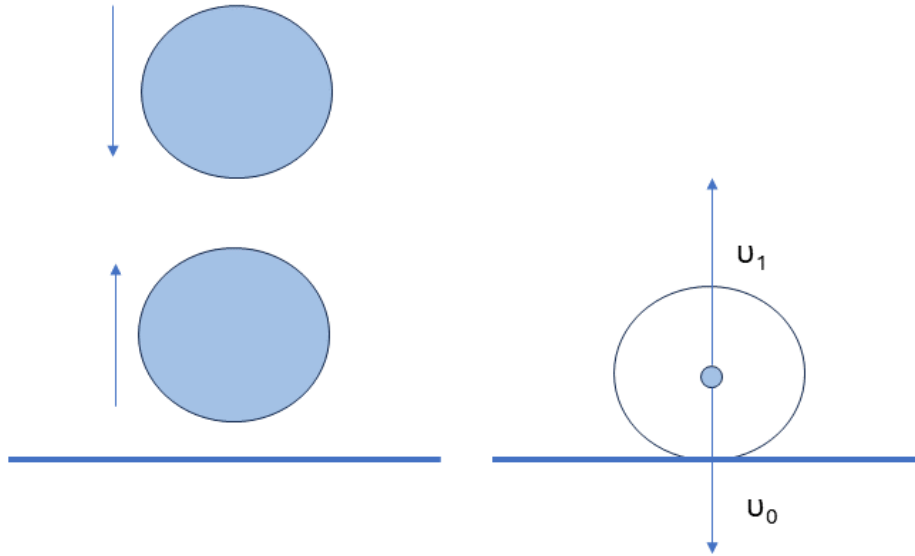


Fig. 2.2: Schematic view of restitution coefficient.

the temperature-dependent molecular properties of ice and decane were determined using the NIST database [54]. The static friction coefficient values for ice are derived from Sukhorukov's recent experiments [55].

2.3 SIMPLE algorithm

In simulations, the Semi-Implicit Method for Pressure-Linked Equations (SIMPLE) is applied as a numerical technique in Computational Fluid Dynamics (CFD) to solve the Navier-Stokes equations. The strength of SIMPLE is its effectiveness in simulating situations where the fluid is incompressible. This algorithm iteratively adjusts the pressure and velocity fields in a flow to satisfy the Navier-Stokes and continuity equations simultaneously.

The process starts with an initial guess for the pressure field p^* to solve the Navier-Stokes equations for incompressible flows [56]. This guessed pressure estimates the fluid's velocities by solving discretized momentum equations. The momentum equation calculates these intermediate velocities, u^* , in a staggered grid format from the assumed pressure field.

$$\frac{D(\rho\phi\vec{u}^*)}{Dt} = -\phi\nabla p^* + \phi(\mu + \mu^{*,t})\nabla^2\vec{u}^* + \phi\rho\vec{g} - \vec{F}_p^*, \quad (2.32)$$

A pressure correction equation [56], derived from the continuity equation, checks how the current velocity field satisfies the continuity equation:

$$\nabla^2 p' \sim \frac{\rho}{\Delta t} \nabla \cdot \vec{u}^*, \quad (2.33)$$

where p' is the pressure correction, and Δt is the time step.

Next, the pressure field is updated using the pressure correction.

$$p^{new} = p + \alpha p', \quad (2.34)$$

where α is an under-relaxation factor often applied to ensure numerical stability. Then, the new velocity field \vec{u}^{new} is found again. At this stage, the rest of the transport equations, e.g. the turbulence model, are resolved.

The entire process, from the solution of the momentum equation to correcting the pressure, is repeated iteratively. Each iteration adjusts the velocity and pressure fields to satisfy the momentum and continuity equations more closely. The iteration continues until the differences in the fields between successive iterations become very small, showing that a consistent solution has been reached.

2.4 Two-way coupling scheme

The methodology outlined in Fig. 2.3 is a numerical approach to resolving the interactions between the fluid and dispersed particulate phases in a multiphase system.

The fluid flow field and particle dynamics are interdependent in multiphase flow simulations. The fluid affects the motion of the particles through drag forces and pressure gradients, while the particles can exert feedback on the fluid through these forces. The iterative process described in the diagram accounts for these two-way interactions.

During each iteration, the velocity of the particles is calculated based on the current state of the fluid flow. Then, the source terms representing the momentum exchange between the particles and the fluid are evaluated and used to adjust the fluid velocity in the next step. The algorithm checks for the satisfaction of the continuity equation to verify that the simulation respects the conservation of mass in the system. If continuity is not satisfied, fluid velocity and pressure corrections are made.

Below, more detailed steps are provided.

The methodology begins by establishing initial conditions that define the state of the fluid and particles. Quantities such as velocity and pressure are specified for the fluid phase, while initial positions and velocities are determined for the particle phase.

Following initialization, the process progresses to a detailed CFD analysis where the fluid flow field is computed. This calculation is based on solving the Navier-Stokes equations to determine the velocity and pressure distributions in the fluid domain. This step is the foundation for understanding how the fluid will interact with the particles.

In the next step, the method measures how fluid and particles interact by considering the forces on the particles, especially the drag force that results from the flow of the fluid. This calculation may also include additional forces derived from specific fluid-particle interaction models.

Using the calculated forces, the DEM simulation phase updates the positions and

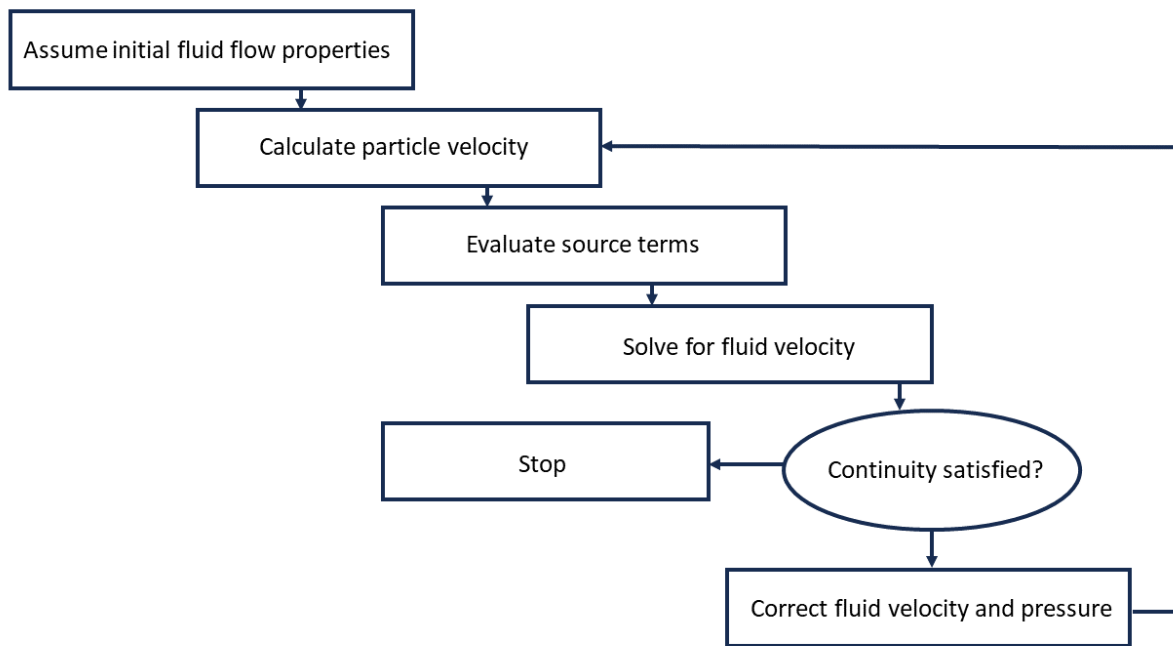


Fig. 2.3: Solution scheme for two-phase coupling. Reproduced from Crowe [45].

velocities of the particles following Newton’s laws of motion. This phase is particularly complex as it considers interactions between particles and between particles and walls.

An important part of the coupling process involves a feedback mechanism to the CFD analysis. This mechanism utilizes updated information about particles to refine the properties of the fluid domain. Because the particle movements impact fluid velocity and pressure fields, it is necessary to adjust the fluid field precisely to account for these changes.

The process is iterative, with the cycle of force calculation, DEM simulation, and feedback to CFD being repeated to ensure that the fluid flow and particle dynamics are continuously updated based on their ongoing interaction. This iterative coupling is essential for achieving a converged solution that represents the coupled behaviour of the fluid and particles, describing their interaction and the mutual influence on each other in the system.

2.5 Contact detection

In particulate flow modelling, collision detection is critical for determining when and how particles in motion will interact.

Figure 2.4 illustrates a key concept in the dynamics of particle collision in a simulation. Two particles are depicted, each with a specific diameter and an initial location in space. Their locations at the start of a discrete-time step are defined by the position vectors r_{10} and r_{20} . In addition to these position vectors, each particle is characterized by velocity vectors v_{10} and v_{20} , representing each particle’s movement’s initial speed and direction. The model assumes that the particles will move following straight trajectories at these initial velocities throughout the time step, predicting

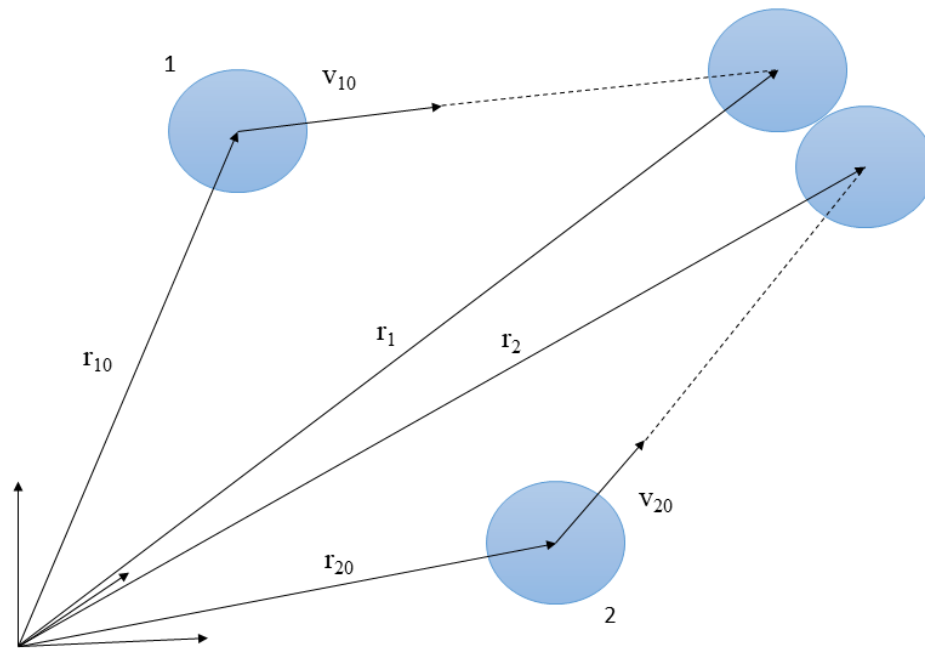


Fig. 2.4: Collision detection principle reproduced from Kosinski [44].

collisions more simply by treating the motion as linear and uniform.

Using the starting positions r_{10} and r_{20} and the initial velocities v_{10} and v_{20} the figure provides a scheme for calculating the potential intersection of the particles' trajectories. If their final positions suggest an intersection, the model calculates the collision time, which is the moment in the time step when the two particles are expected to collide. This aspect of collision timing is important for simulations that analyze how particles interact in a fluid, as these interactions can affect the system's overall behaviour.

Fundamentally, this process is about calculating the time until collision, known as the collision time. This is computed using the relative positions and velocities of the particles and applying the physical laws governing their interactions. Once the collision time is determined, it checks if this collision is likely to happen in the current step of the simulation. If a collision is predicted, the simulation algorithm adjusts the positions of the particles to the point of collision, simulating the physical contact between them.

Following the collision detection, the simulation must compute the resulting outcome of the collision. This includes updating the velocities and trajectories of the particles post-collision by conserving momentum and energy principles. Next, the simulation updates its time settings based on the collision's length and prepares for the next time step.

The general goal of collision detection algorithms is to accurately and efficiently simulate the interactions of particles in a given system, providing information into the

dynamics of systems.

The process is iterative and involves the following steps:

• **Initiation of the Time Step.**

The simulation begins a new cycle, initializing variables that will track the progression of time and the number of collisions.

• **Prediction of Upcoming Collision.**

The simulation computes the time for two particles to collide based on their current trajectories and velocities.

• **Determination of Collision Occurrence.**

The simulation checks if the calculated time until collision is in the current time step interval.

• **Adjustment of Particle Positions.**

If a collision is about to occur, the particles are moved to the collision point according to the calculated time until the collision. Otherwise, they are moved according to the remaining time in the step.

• **Collision Dynamics Processing.**

If a collision is detected, the simulation uses the relevant contact model (e.g. Hertz-Mindlin) to calculate the post-collision velocities and directions.

• **Update of Time Variables.**

The simulation updates the time to account for the duration of the collision.

Using the calculated forces, the DEM simulation updates the positions and velocities of the particles following Newton's laws of motion.

• **Progression to the Next Cycle.**

The simulation proceeds to the next time step, ready to repeat the process.

2.6 Discrete element method collision time scale

In the Discrete Element Method, the choice of the time step is important. The collision time scale, and therefore the time step, depends on one of three times associated with the particle: Rayleigh wave propagation time, impact duration, and particle transit time [43].

The collision simulation is based on the principle that a particle's force interactions are influenced by its nearest neighbours within a single time step. During the time step, the deformation Rayleigh wave is supposed to cross the particle's surface. In this case, the time of the Rayleigh wave propagation in a spherical particle is computed as [43]:

$$\tau_1 = \frac{\pi r}{V_R}, \quad (2.35)$$

where V_R is the Rayleigh wave velocity, which depends on material properties. In Simcenter STAR-CCM+, to reduce computational costs, this parameter is estimated using a simplified expression [57, 58].

The second criterion for determining the appropriate time step in DEM simulations involves the collision duration between two elastic spheres. Based on Hertz's contact mechanics theory, Timoshenko provided a suitable expression for this time scale [59]. The calculation of the parameter involves the radius of the particle and the elastic

properties of the material. This rule helps keep the simulation realistic by considering the important details of particle collision:

$$\tau_2 = 2.94 \left(\frac{5\sqrt{2\pi}\rho_p}{4} \frac{1 - \nu^2}{E} \right)^{\frac{2}{5}} \frac{r}{\sqrt[5]{\nu_r}}. \quad (2.36)$$

The last rule for realistic simulations refers to a limitation of how far a particle can move in one step of the simulation. If a particle moved too fast, it might skip past another particle or a wall without ever "noticing" it. To prevent this, we set up the simulation so that a particle can only travel the distance of its radius for 10 steps. In this way, the interactions between particles and between particles and walls are accounted for properly. The equation for the impact duration [43]:

$$\tau_3 = 0.1 \frac{r}{v}, \quad (2.37)$$

In CFD-DEM simulations, the time step is typically chosen based on the smallest of the mentioned three time scales to ensure that all significant physical processes are accurately captured. Therefore, the time step is defined as $\min(k_D \tau_1, 0.1\tau_2, \tau_3)$, where $k_D < 1$ is the scaling pre-factor tuning up the model. It is to be noted that τ_1 is often the minimum number and, therefore, the major limiting factor, while the rest of the time scales filter the fast particles. If the time step is too large to resolve the Rayleigh wave propagation, the model may fail to capture critical aspects of particle interactions during collisions. If the time step is longer than the impact duration, the model might incorrectly calculate the energy transfer and momentum change during collisions.

MACHINE LEARNING APPLICATION

This chapter provides a theoretical description of the machine learning part of the thesis, particularly the random forest classifier. Using machine learning-based predictions of physical phenomena is a relatively new approach and is being actively implemented in fluid dynamics and heat transfer, as discussed in the thesis introduction. Less information is available on using machine learning methods in multiphase and, particularly, on ML models of plugging and clogging of flow channels. This data-driven approach is a time-efficient solution, capable of making predictions in several seconds on ordinary machines. In contrast, a CFD-DEM case takes 2-4 hours to run on a 30-core AMD-based PC, while a typical flow loop experiment takes about 3 hours. In this research, the motivation to use the random forest classifier is based on its flexibility with multidimensional datasets, making it a suitable method for the studied cases involving multiple parameters and features.

Random forest is a machine learning algorithm in the supervised learning category. This method applies to both classifying data and predicting continuous values. The fundamental building block of a Random forest technique is the decision tree. Decision trees are a helpful method used in decision-making processes. Their logical structure of the blocks is similar to trees, featuring branches and leaves that represent different decisions and outcomes [60]. Random forest classifier combines multiple trees to improve predictive performance and control over-fitting. A group of trees, known as an ensemble with unique trees constructed by various strategies, improves the overall decision-making process.[61].

Figure 3.1 illustrates the Random Forest algorithm. The process starts with a complete input dataset divided into two parts: the training set and the test set. The training set is used to build the model, while the test set is used to evaluate its performance. Using the training set, the algorithm begins the process of bootstrap sampling. Multiple subsets of the training data are created, each selected randomly with replacement. This allows the individual decision trees in the forest to be trained on different data, providing a diversity that makes the model more robust. Each subset of the training data is then used to create a decision tree. These trees are grown by splitting them based on the data's features. The trees are grown until they reach a specified stopping criterion: a certain depth, a limiting number of samples in a leaf, or another predefined threshold. After all the decision trees are constructed, they collectively make predictions on new data. Each tree in the forest gives its prediction, which is then combined through voting. The test set is then used to evaluate the model's

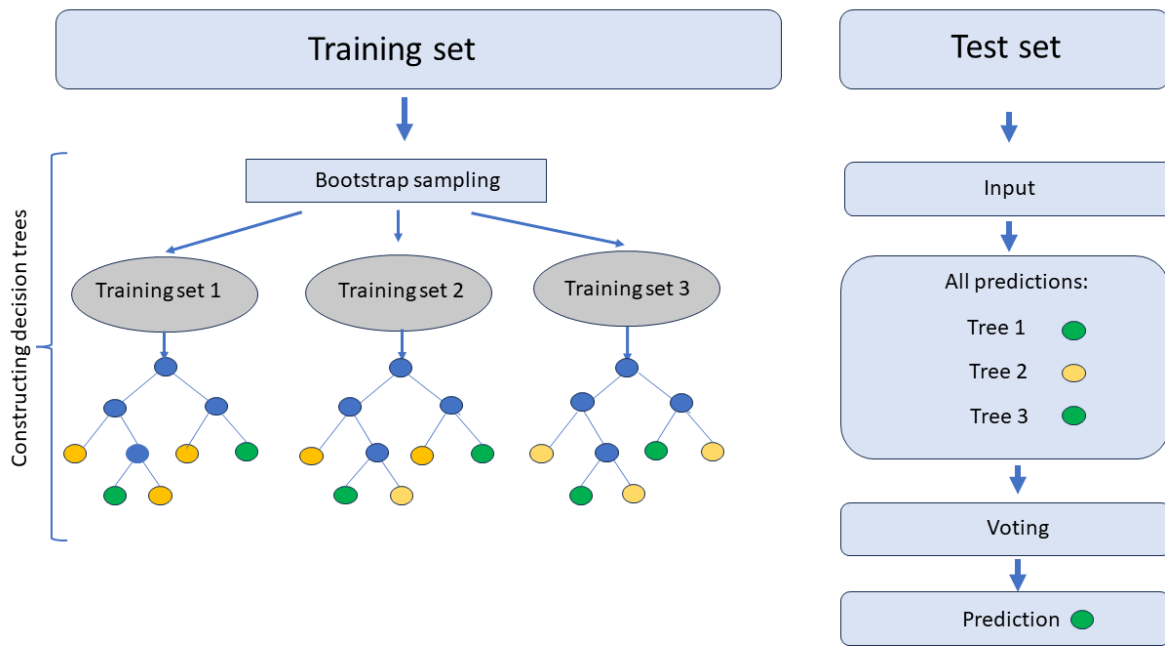


Fig. 3.1: The flowchart of the Random Forest algorithm.

performance, providing an unbiased assessment of its predictive power. The final goal of the Random Forest algorithm is to achieve high accuracy while also preventing overfitting.

Training a predictive model using the same data for learning and testing is flawed because the model might memorize the data without learning to generalize. This issue, known as overfitting, means the model performs well on data it has seen but poorly on new data. To counter this, it's standard practice in machine learning to set aside some data as a test set.

In the Random Forest classifier, the feature importance indicates the relative importance of each parameter in predicting the target variable. It shows how much they contribute to the model's decision-making process. The importance is calculated at the model training stage when each tree in the forest evaluates how much adding a specific parameter improves node cleanliness and how well it can help make a correct prediction. Functions that lead to a significant increase in the model's accuracy will receive a higher importance score. This information is valuable because it helps to understand the data better, optimize the choice of functions, and make informed decisions about allocating resources for further data collection. This study considered a case with three parameters, but for cases with larger sets, this is an essential aspect for optimizing data and the model.

The classifier's parameters define how the model behaves during the training process. Each parameter serves a specific purpose, following a brief description of some main parameters for the Random Forest Classifier in Scikit Learn. In Scikit Learn's Random Forest Classifier, the parameter "n_estimators" refers to the number of decision trees included in the forest. The "max_depth" parameter specifies the maximum number of levels allowed in each decision tree. The "random_state" parameter is used to set seed to ensure consistent results across multiple simulation runs, which aids in

the reproducibility of the results [62]. The parameters can be finely tuned to optimize the model's performance for specific datasets and problems.

SUMMARY OF THE RESULTS

This chapter presents a brief overview of four papers, covering objectives discussed in the introductory section. Initially, the focus was on validating the CFD-DEM method, accomplished using experimental data. The first validation case provided a foundation for further application of this method. However, since the initial investigation only involved glass bead particles and did not model cohesive interactions, which is a key aspect of the research, it was essential to understand how the CFD-DEM model handles cohesive particle behaviour before proceeding with the simulation of blockage with sticky ice particles. As a result, the second article presents the findings of this investigation, where the model was validated using experimental high-speed video recordings and the Positron Emission Particle Tracking (PEPT) method. Subsequently, the third article presents a simulation of the blockage process in the experimental flow loop test section. Finally, with all available data collected, a machine learning classifier was applied to predict blockage in the considered concentration range. The results, including the flow regime map, are detailed in the fourth article.

At the very beginning of the project, the cohesive CFD-DEM model of STAR-CCM+ [43] was tested to simulate plugs blocking the entire cross-section of the flow channel. As a referent model, the work by Mondal et al. [27] was used for the case settings. In their work, the authors simulated the flow of particulate suspension in a rectangular channel with a constriction, varying the particle concentration to study the jamming process at a contraction of the flow channel. The focus was on how the probability of jamming depends on particle concentration and the impact of various parameters on the process. The current CFD-DEM simulations aimed to reproduce the process by changing the particle concentration until jamming was observed using flow parameters similar to those presented in the study. For the simulations, the case-settings with the neutrally buoyant particles were reproduced. As follows from the referent work [27], the particles jammed the contraction at the inlet volume fraction of 18%. In the cohesive CFD-DEM with the surface energy of 824 mJ/m^2 , the particles blocked the contraction at a lower inlet concentration of 5%, confirming the technical possibility and qualitative realism of the simulation set-up.

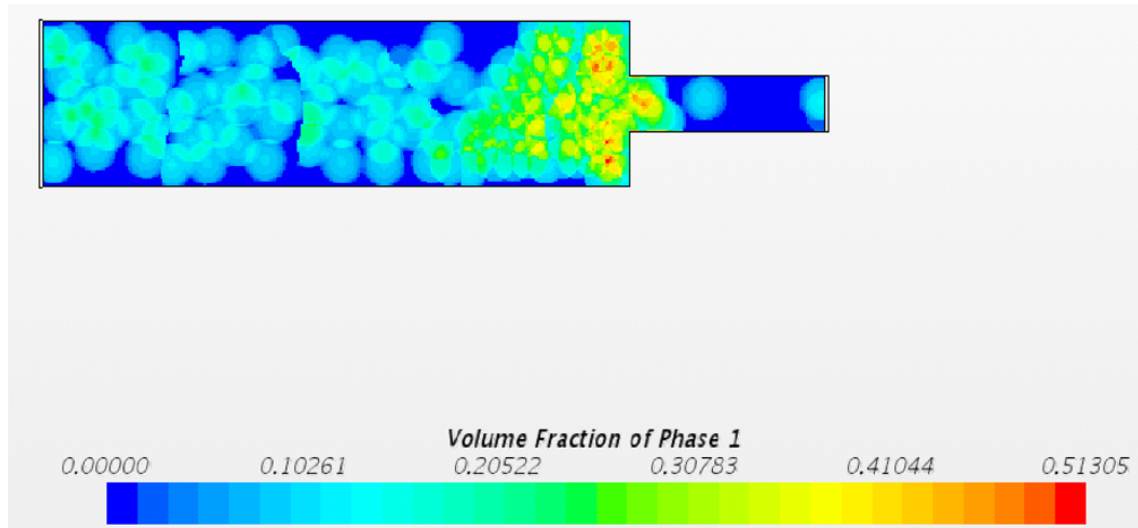


Fig. 4.1: Cohesive particles blocking the flow channel for flow conditions as in Mondal et al. [27]. Scalar contours denote the volume fraction of particles.

4.1 Paper A: Simulation of horizontal hydraulic conveying and dune formation based on CFD-DEM

In this phase of applying the CFD-DEM for analyzing non-cohesive particles, the CFD-DEM model was successfully implemented to simulate the hydraulic transportation of glass bead particles, each with a diameter of 100 μm , through a horizontal cylindrical millifluidic tube that measures 2 mm in diameter and 20 cm in length. The simulations were validated against experimental data from [63], showing the model's accuracy in predicting particle flow dynamics in a laminar regime. The focus was on the interaction between the water flow and the glass bead particles under standard conditions, reproducing a case where the particle concentration was 28%, and the flow rate was set at 2 ml/min. Additionally, the simulations considered how the results are sensitive to the variation of the restitution coefficient (0.70-0.98) to observe different results in particle behaviour and dune formation in the flow.

The important result of the simulations was the ability to predict the formation of dunes and to understand the behaviour of particles in hydraulic transport systems. The model's predictions of the velocity and the length of the dunes were then compared to experimental data. The comparison demonstrated a discrepancy of approximately 10.7% from the observed experimental data for the velocity of the dunes.

The combined CFD-DEM method showed the ability to simulate complex regimes in the particulate multiphase flow. This study also showed the potential of CFD-DEM for simulating and analyzing hydraulic transport systems. With the implementation of the CFD-DEM approach to predict dune formation, this work was an important initial step in verifying the method's performance with the particulate multiphase flow.

4.2 Paper B: Cohesive collisions of particles in liquid media studied by CFD-DEM, video tracking, and Positron Emission Particle Tracking

In this part, the study extended toward investigating the cohesive collision of ice in an oil-based continuous phase using the CFD-DEM approach. This paper presents research on the ice-ice interactions under different temperatures, focusing on the dynamics of their collision. The study combines high-speed video recording, Positron Emission Particle Tracking (PEPT), and coupled CFD-DEM simulations.

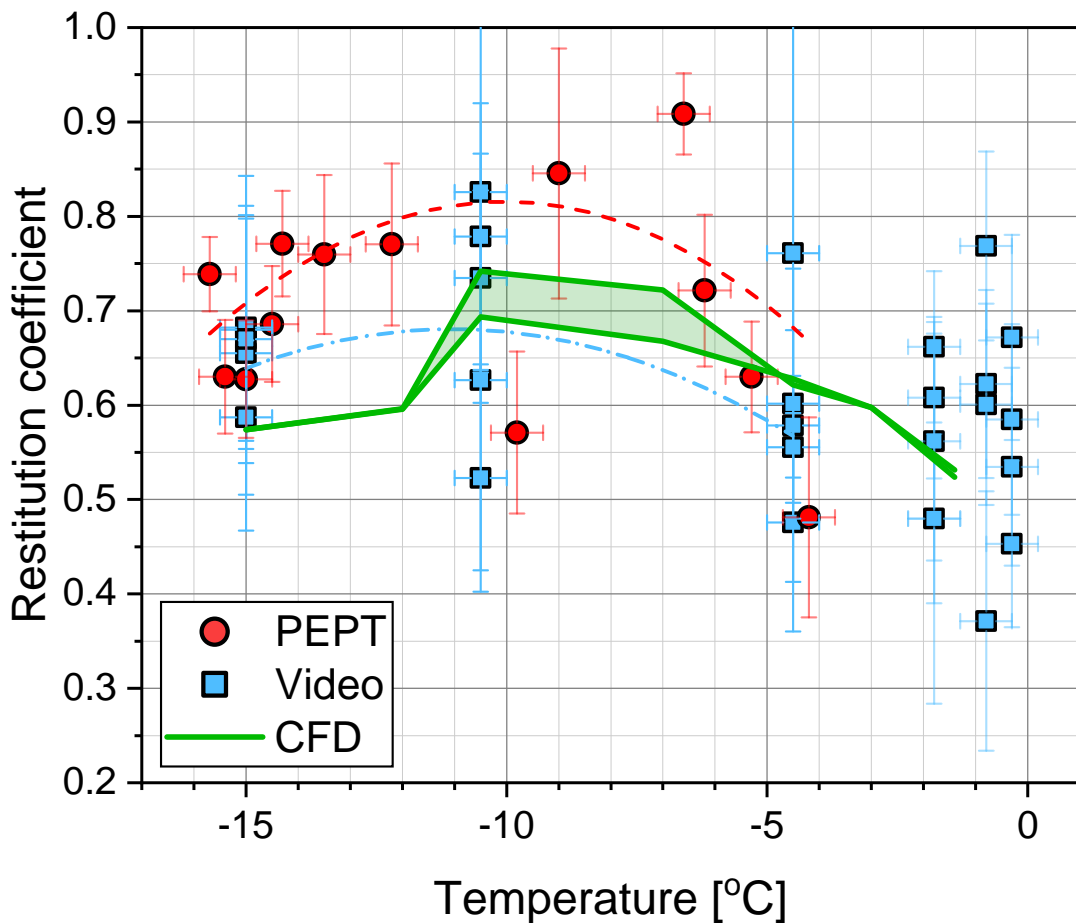


Fig. 4.2: Coefficient of restitution of ice in decane [40]

The combined experimental and CFD-DEM study of the ice particle drop and its interaction with the inclined ice surface was conducted for a temperature range from -15.7°C to -0.3°C to consider the influence of cohesive forces of different magnitude. The coefficient of restitution (COR) value was extracted from the experiments and simulations as the crucial parameter characterizing the collisions.

Figure 4.2 illustrates the main result of the study, which is the coefficient of restitution (COR) of ice for the considered temperature range, derived from three research methods used in this work: CFD-DEM simulations, experimental recordings, and Positron Emission Particle Tracking (PEPT). The CFD-DEM results are presented with two input datasets: median cohesion force values and 95%-based values from Yang et

Summary of the results

al. [50]. COR for ice particles varies between 0.57 and 0.82, and as can be seen from the plot, the optimum temperature at the maximum COR is identified for -11.0°C (video), -10.5°C (CFD), and -10.0°C (PEPT). As the temperature rises, the COR initially increases, peaking at the temperature of maximum COR. Following the peak, the COR declines and stabilizes at around -4.2°C . This pattern is explained by the two factors which balance each other at the maximum point. The increase in the restitution coefficient is due to the decreasing viscosity of the decane, while the decreasing values are attributed to the enhanced cohesion at elevated temperatures. The model agrees well with experimental data, showing the average and maximum discrepancies of 9.4% and 12.1% respectively. However, the deviation of the PEPT experiments is higher, with an average of 19.0% and a maximum of 21.7%. Despite this, the temperature trend of COR is similar across all three methods. The results of this work demonstrate that the CFD-DEM model predicts the behaviour of ice-ice interaction in the oil phase and can be applied to simulate complex multiphase interactions with reasonable accuracy in the same system.

This study improved our understanding of ice in the oil collision process, providing new data on COR for the temperature range considered. Importantly, this work laid the foundation for ice in oil collision dynamics for further simulations of the entire flow, which will be discussed in the summary of the following paper.

4.3 Paper C: CFD-DEM model of plugging in flow with cohesive particles

In the next stage, the CFD-DEM approach was applied to simulate and analyze plug formation in an experimental flow loop's test section, considering plugging dynamics and validating results against experimental benchmarks. It is important to note that the previous work (Paper B) was used to define the mechanical properties of ice.

The third article presents the CFD-DEM model built to investigate the plugging process with cohesive particles, focusing on the impact of variables like particle concentration, Reynolds number, and surface energy on plugging behaviour. It shows a non-linear relationship between these factors.

The CFD-FEM model was validated against the experimental study by Struchalin et al. [20]. The model reproduced an experimental case where a plug formed in the test section at 400 kg/h initial flow rate and a particle concentration of 6.8%. The main result of the work is presented in Figure 4.3 as a graph showing the temporal evolution of the average flow velocity, where the experimental results are compared with the CFD-DEM model results using three different cohesion to adhesion ratios (0.78, 0.8, 0.88). For this system, cohesion was derived from work by Yang et al. [50], while the parameters of adhesion and friction of particles against the walls were fitted.

The study compares simulation results with existing flow maps from previous experiments, proving the model's capability to accurately predict plugging events in multiphase flow despite simplifications and assumptions like 2D geometry, low Young modulus, and no account for the geometry of the entire experimental setup. In terms of experimental verification, this study successfully demonstrates the CFD-DEM model's ability to simulate plugging in multiphase flow with cohesive particles.

4.4 Paper D: Application of machine learning to predict blockage in multiphase flow

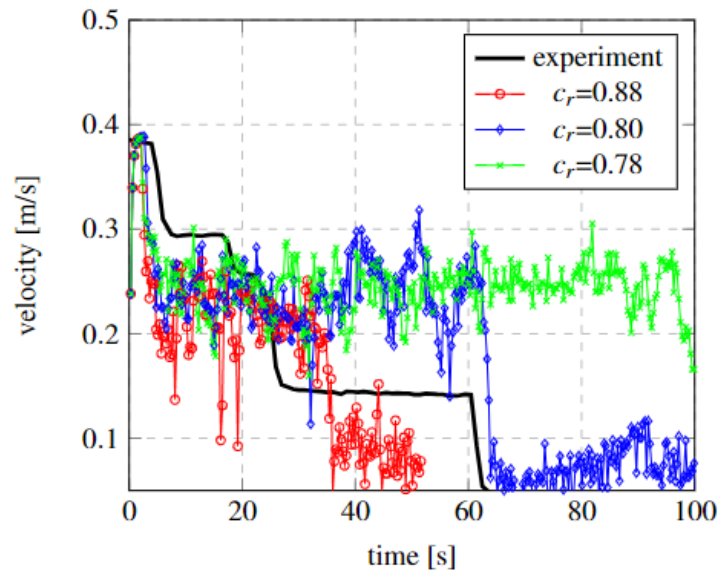


Fig. 4.3: Average flow velocity as a function of time predicted by the CFD-DEM model and compared with the experiment [20]. The simulations are carried out for different ratios of particle-wall adhesion to the particle-particle cohesion c_r . [46]

4.4 Paper D: Application of machine learning to predict blockage in multiphase flow

The fourth paper presents the application of a machine learning classifier for predicting blockage caused by cohesive particles in multiphase flows. The study focuses on applying a random forest classifier to predict blockage. The classifier is trained using the experimental and CFD-DEM data. The experimental setup involved a lab-scale flow loop to study ice slurry in decane [20]. The simulation is based on the coupled CFD-DEM method. The classifier was trained on parameters obtained from these experiments and simulations, including flow rates, Reynolds number, and Capillary number, to identify blockage conditions.

Figure 4.4 shows a flow map displaying the study's main result, the blockage threshold identified for a certain range of particle concentrations. The threshold predicted by the ML model is represented in the figure by three lines, each varying the dimensionless cohesion (granular capillary number). It's important to note that increasing the capillary numbers (and cohesion) by factors of 0.5 and 0.8 leads to a decrease in the threshold predicted by the machine learning model. The CFD-DEM simulations and experimental outcomes are also shown in the figure to validate the results. As can be seen from the plot, the thresholds predicted by the machine learning algorithm almost align with the upper experimental limit and the plugging boundaries indicated with the CFD-DEM.

Summary of the results

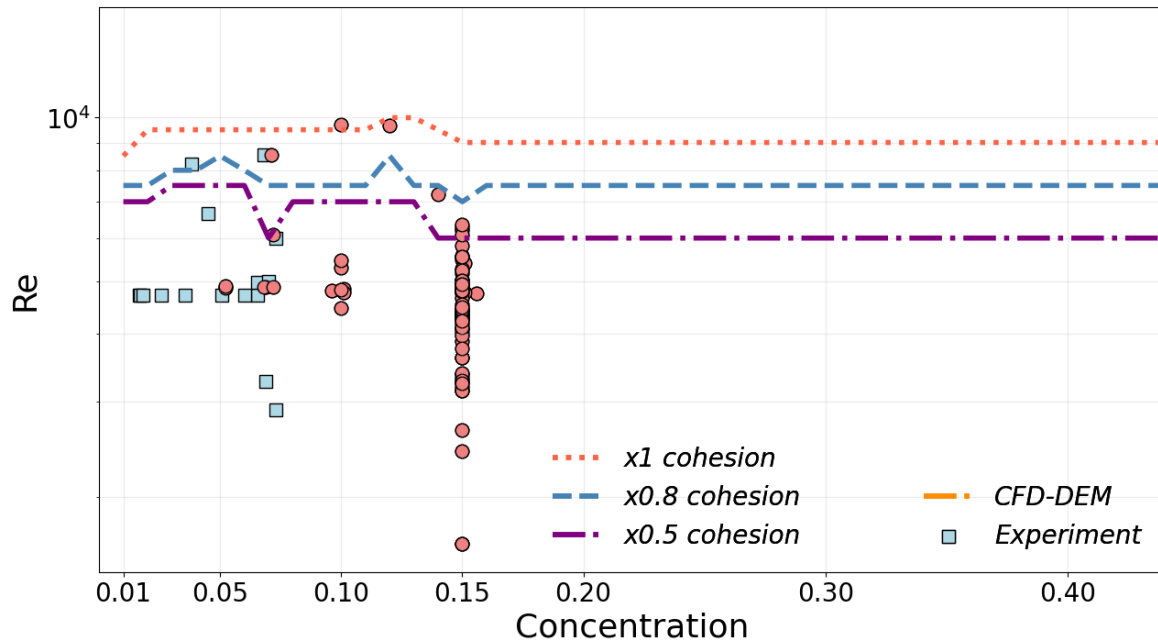


Fig. 4.4: Flow map from the random forest classifier with three different cohesion values. The plot includes the experimental [20] and the CFD training data points with blockage. Experimental points excluded from training are labelled with star-like markers. Reproduced from Paper D.

The model results demonstrated that the classifier predicted blockage occurrences with a precision of 1.00 for no block cases and 0.96 for block cases, while the F1-score is 0.89 for no block cases and 0.98 for block cases, demonstrating the effectiveness of the chosen method. Sensitivity analyses showed the model's adaptability to cohesion variations.

EFFICIENCY AND APPLICABILITY OF THE CFD-DEM MODEL

This chapter discusses aspects of using computational resources effectively to conduct numerical simulations. It begins with a focus on achieving physically realistic and time-efficient simulations and presents analysis results for computational costs. The second part of the chapter provides analysis by comparing the Eulerian-Lagrangian approach to the Eulerian-Eulerian model through a case study of plug formation in a test section of an experimental flow loop. Before discussing comparison results, the chapter briefly outlines the Eulerian-Eulerian method.

5.1 Notes on computational costs

Understanding the computational efficiency of numerical simulations is important for optimizing the use of resources and reducing the time required for analyses. The ultimate goal is to achieve simulations that are both accurate and time-efficient. This is particularly important in simulating physical processes, like plug formation, where the precision of results can impact the interpretation and applicability of research results. Considering how computational time changes with different numbers of processor cores is interesting, as is achieving a balance between computational demand and the realism of physical systems.

In this research, numerical simulations were conducted to reproduce the conditions described in Paper C, particularly the case with the maximum cohesion of 541 J/m^2 . In these simulations, the adhesion of walls was set equal to the cohesion of particles. These simulations aimed to observe the formation of plugs under different conditions, specifically by changing the number of processor cores used. The simulations were conducted on AMD Ryzen Threadripper RO 3975WX (3.8 GHz). The number of physical cores ranged from 1 to 30, and the number of logical cores with hyperthreading from 35 to 60 [64].

Figure 5.1 illustrates how the total computational time, calculated per central processing unit (CPU), changes with the number of processors engaged. As can be seen from the graph, the optimal number of CPUs for efficient simulation is approximately 15. After reaching this point, the simulations do not get much faster because more time is spent communicating between the processors. Moreover, as noted by the documentation of STAR-CCM+ [43], expanding the simulation to logical cores hinders

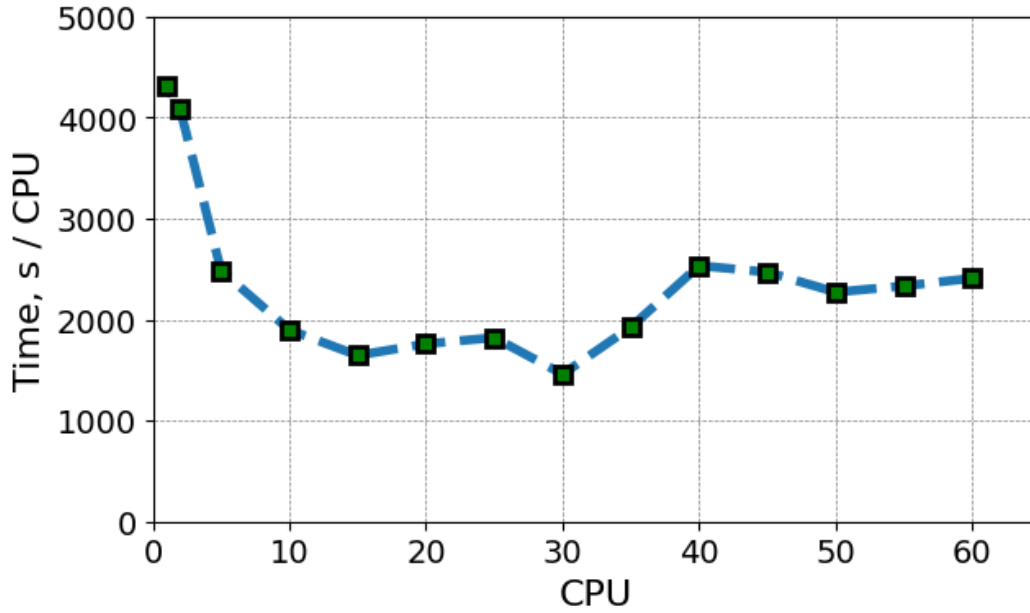


Fig. 5.1: Effect of processor utilization on computational time.

the computation.

5.2 Applicability of different multiphase CFD methods

5.2.1 Eulerian-Eulerian approach

The Eulerian-Eulerian model is a computationally efficient approach to modelling complex multiphase flows, especially useful for high particle concentrations where the direct interaction of individual particles would be challenging to resolve. The Eulerian-Eulerian model describes dispersed and continuous phases as separate but interacting liquids present in the same computational domain [65].

The most common approach, named the two-fluid model, treats the fluid and particles as two continuous phases and solves the Navier-Stokes equations for each phase separately. In this model, the conservation of mass for each phase is represented by the continuity equation:

$$\frac{D(\phi_m \rho_m)}{Dt} = 0, \quad (5.1)$$

where ϕ_m is the volume fraction and ρ_m is the density of phase m .

The sum of volume fractions for all phases equals one, ensuring no overlap:

$$\sum_{m=1}^s \phi_m = 1.0. \quad (5.2)$$

The momentum conservation equation accounts for the forces acting on each phase:

$$\frac{D(\phi_m \rho_m \vec{u}_m)}{Dt} = -\phi_m \nabla p + \phi_m \rho_m \vec{g} + \phi_m \nabla \cdot (\tau_m + \tau_m^t) + \vec{F}_p, \quad (5.3)$$

where \vec{u}_m is the phase velocity vector, p is the pressure, \vec{g} is the gravitational acceleration, τ_m and τ_m^t represent molecular and turbulent stress tensors. \vec{F}_p is the inter-phase coupling term, including the drag force, which is significant as it models the resistance experienced by the particles moving through the fluid. In this model, the deposited particles can hinder the dispersed phase through the momentum coupling terms. In addition, rheological expressions representing the apparent viscosity of suspensions could modify τ_m and thus simulate the inter-particle interactions [65].

One of the significant advantages of the Eulerian-Eulerian approach is lower computational requirements. However, the noted disadvantage is that interactions between particles are not modelled directly but instead are represented through an averaged term of solid stress. This reduces the accuracy and limits the applicability of the model.

5.2.2 Comparative analysis

In the second chapter, the advantages of the Eulerian-Lagrangian approach were previously discussed, especially in comparison to the Eulerian-Eulerian model. To provide a clear analysis, it was decided to compare the simulation results of plug formation in a test section of an experimental flow loop as a case study. The Eulerian-Eulerian model is implemented following the methodology from Balakin et al. [66]. At the same time, the rheological expression for the ice slurry is provided in work by Naukanova et al. [64, 67].

An experimental case of blockage in the test section of the experimental flow loop was reproduced for comparative analyses. The case details are described in Paper C. Both cases share identical boundary conditions for the fluids, including volume fractions and particle dimensions, as well as matching time steps and computational algorithms. The simulations were run on a similar computational setup with 32 CPUs and utilized comparable mesh configurations.

The concentration profiles of particles at the same time interval were considered. In the case of the Eulerian model, it was observed that particles did not block the pipe, while particles did settle and formed a stationary bed.

Figure 5.2 demonstrates how the mean flow velocity changes with time during the pipe plugging for the case where the adhesion of the walls was set to 80% of the inter-particle cohesion. The graph shows that the velocity measured in the experiment and predicted by the Eulerian-Lagrangian model both vary with time, experiencing a drop after 60 seconds. On the other hand, according to the Eulerian-Eulerian model, the mean velocity stays steady throughout the entire period. This demonstrates the superiority of the Lagrangian method in modelling dynamic changes in flow with cohesive particles interacting with the walls and each other.

Figure 5.3 illustrates a scalar scene depicting simulation results using two methods. The scene visualizes the volume fraction of ice particles in an experimental flow loop test section. Figure 5.3 shows that the Eulerian-Lagrangian method can reproduce the plug. This method considers particles' trajectories and interactions with a more detailed and realistic particle dynamics simulation. In contrast, the Eulerian-Eulerian model shows only the accumulation of particles near the constricted section.

Table 5.1 demonstrates the computational time scaled to the number of CPUs

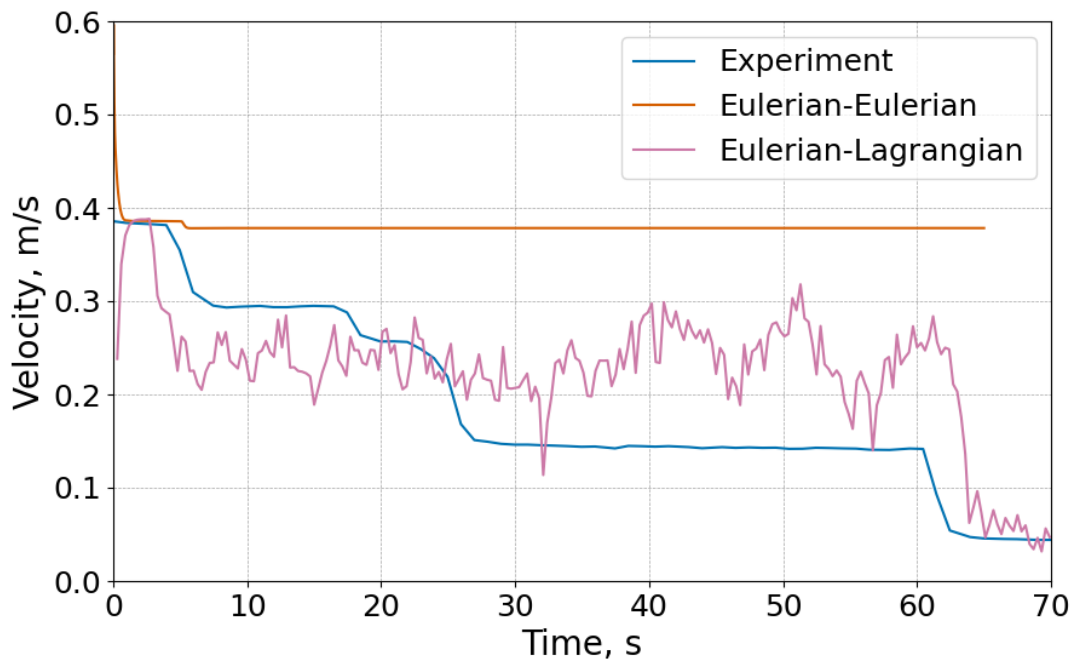


Fig. 5.2: Velocity comparison between experimental data and two computational models.

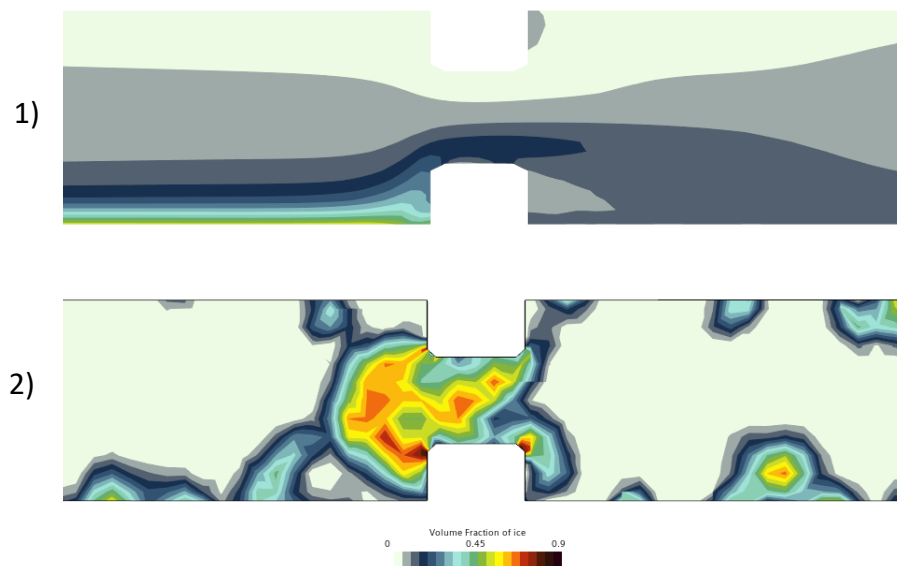


Fig. 5.3: Comparison of two methods: 1) Eulerian-Eulerian and 2) Eulerian-Lagrangian. The flow direction is left to right, and gravity is directed downwards.

5.2 Applicability of different multiphase CFD methods

employed. As the table indicates, a quasi-2D CFD-DEM model (see paper C) does not show a significant speed reduction compared to the Eulerian method. Additionally, for comparative purposes, the computational costs for a fully 3D CFD-DEM model at maximum cohesion, as outlined in the paper, were also presented.

Time/(CPU x 1 sec of process)	Model
46384.203	Eulerian-Lagrangian 3D
221.42041	Eulerian-Lagrangian 2D
127.79211	Eulerian-Eulerian 3D

Table 5.1: Comparison of computational time for different simulation models.

It can be concluded that although the Eulerian-Eulerian model is computationally more efficient, it does not provide the desired level of physical realism.

CONCLUSIONS AND FUTURE WORK

The combined results from the four articles present coupled Computational Fluid Dynamics-Discrete Element Method (CFD-DEM) simulations and machine learning-based methods to address multiphase flow dynamics with cohesive particles.

In the project's first stage, the non-cohesive CFD-DEM model was built to simulate the hydraulic transport of glass beads. The simulation results provided insight into the process of particle dune formation. The simulations aligned well with experimental data, demonstrating the model's predictive power.

A comprehensive theoretical and experimental investigation of cohesive collisions of particles with inclined walls was conducted next. The CFD-DEM models have been validated against experimental benchmarks to simulate particle behaviour with reasonable accuracy. The simulations considered temperature effects on particle-wall adhesion and their restitution coefficient for validation purposes. These parameters were essential for realistically modelling multiphase systems with sticky particles. The model was further updated to represent a multi-particle cohesive turbulent flow in the experimental flow loop, reproducing the plugging of a test section conditioned by a local flow restriction - a centrally open orifice.

As the final stage, a machine learning-based approach, the random forest classifier, effectively predicted blockages in multiphase flows with cohesive particles. The model demonstrated its capability to adapt to cohesion variations and could be extended for real-time applications.

For future research based on the information from the four reported here studies, the following areas of work are recommended to improve the understanding and prediction of particle behaviour in flow systems.

Concentration variability: Future work could benefit from exploring a wider range of particle concentrations. This expansion would provide a more detailed map of plugging in densely packed and dilute systems.

Particle adhesion: It would be interesting to define the adhesion properties of particles to surfaces more accurately. A refined understanding of adhesion could lead to better predictions of plugging and improved design parameters for industrial equipment.

Different particle shapes: Expanding simulations to cover a wider selection of particle shapes with new capabilities of Star-CCM+ could help to understand better how different particles behave and stick. Consequently, this would allow a complete view of how various particle types influence flow patterns.

Conclusions and Future Work

In-situ PEPT validation: Positron Emission Particle Tracking (PEPT) conducted directly in the multi-particle system could offer more precise data and validation of simulation models. Tracking particles interacting with walls and deposits in the turbulent flow is important for validating CFD-DEM models. This in-situ approach would ensure that the behaviour of particles is captured in the exact operating conditions they would encounter in practical applications.

Machine learning approach: Although using a random forest classifier has proven effective, experimenting with other machine learning models, such as deep learning networks, could uncover hidden patterns and relationships in the data. New applications may result in powerful predictive capabilities.

By considering these suggested areas, future research can advance the current work with more detailed and improved methods for predicting and managing the plugging process in multiphase flows.

BIBLIOGRAPHY

- [1] Amadeu K Sum, Carolyn A Koh, and E Dendy Sloan. Clathrate hydrates: from laboratory science to engineering practice. *Industrial & Engineering Chemistry Research*, 48(16):7457–7465, 2009. [1](#)
- [2] Guro Aspenes. The influence of pipeline wettability and crude oil composition on deposition of gas hydrates during petroleum production. 2010. [1](#)
- [3] Esam Jassim, M Abedinzadegan Abdi, and Y Muzychka. A new approach to investigate hydrate deposition in gas-dominated flowlines. *Journal of natural gas science and engineering*, 2(4):163–177, 2010. [1](#)
- [4] Hydrate Agglomeration and Deposition Studies - HYADES. <https://www.sintef.no/en/publications/publication/251566/>. [1](#)
- [5] Kjell H Bendiksen, Dag Malnes, Randl Moe, and Sven Nuland. The dynamic two-fluid model olga: Theory and application. *SPE production engineering*, 6(02):171–180, 1991. [1](#), [1.1](#)
- [6] Ana M Sousa, Tiago P Ribeiro, Maria J Pereira, and Henrique A Matos. On the economic impact of wax deposition on the oil and gas industry. *Energy Conversion and Management: X*, 16:100291, 2022. [1](#)
- [7] Daniyar Kazidenov, Furkhat Khamitov, and Yerlan Amanbek. Coarse-graining of cfd-dem for simulation of sand production in the modified cohesive contact model. *Gas Science and Engineering*, 113:204976, 2023. [1](#)
- [8] Ting Ye, Huixin Shi, Nhan Phan-Thien, and Chwee Teck Lim. The key events of thrombus formation: platelet adhesion and aggregation. *Biomechanics and Modeling in Mechanobiology*, 19:943–955, 2020. [1](#)
- [9] World Health Organization. The top 10 causes of death. <https://www.who.int/news-room/fact-sheets/detail/the-top-10-causes-of-death>, 2020. [1](#)
- [10] Lukas Hohmann, Mira Schmalenberg, Mathusah Prasanna, Martin Matuschek, and Norbert Kockmann. Suspension flow behavior and particle residence time distribution in helical tube devices. *Chemical Engineering Journal*, 360:1371–1389, 2019. [1](#)
- [11] Bhesh Bhandari and Tony Howes. Relating the stickiness property of foods undergoing drying and dried products to their surface energetics. *Drying Technology*, 23(4):781–797, 2005. [1](#)
- [12] Vanessa Neßlinger, Stefan Welzel, Florian Rieker, Dennis Meinderink, Ulrich Nieken, and Guido Grundmeier. Thin organic-inorganic anti-fouling hybrid-films for microreactor components. *Macromolecular Reaction Engineering*, 17(1):2200043, 2023. [1](#)

BIBLIOGRAPHY

- [13] Min-Cheng Tu and Robert Traver. Clogging impacts on distribution pipe delivery of street runoff to an infiltration bed. *Water*, 10(8):1045, 2018. [1](#)
- [14] Xia He, Francis L de los Reyes III, and Joel J Ducoste. A critical review of fat, oil, and grease (fog) in sewer collection systems: Challenges and control. *Critical Reviews in Environmental Science and Technology*, 47(13):1191–1217, 2017. [1](#)
- [15] Prithvi Vijayamohan, A Majid, P Chaudhari, E Dendy Sloan, Amadeu K Sum, Carolyn A Koh, E Dellacase, and Michael Volk. Hydrate modeling & flow loop experiments for water continuous & partially dispersed systems. In *Offshore Technology Conference*, page D021S028R004. OTC, 2014. [1.1](#)
- [16] Ahmad A Majid, Wonhee Lee, Vishal Srivastava, Litao Chen, Pramod Warriier, Giovanni Grasso, Prithvi Vijayamohan, Piyush Chaudhari, E Dendy Sloan, Carolyn A Koh, et al. Experimental investigation of gas-hydrate formation and particle transportability in fully and partially dispersed multiphase-flow systems using a high-pressure flow loop. *SPE Journal*, 23(03):937–951, 2018. [1.1](#)
- [17] Lin Ding, Bohui Shi, Yang Liu, Shangfei Song, Wei Wang, Haihao Wu, and Jing Gong. Rheology of natural gas hydrate slurry: Effect of hydrate agglomeration and deposition. *Fuel*, 239:126–137, 2019. [1.1](#)
- [18] Aurélien Bordet, Sébastien Poncet, Michel Poirier, and Nicolas Galanis. Flow visualizations and pressure drop measurements of isothermal ice slurry pipe flows. *Experimental Thermal and Fluid Science*, 99:595–604, 2018. [1.1](#)
- [19] Takero Hirochi, Shuichi Yamada, Tuyoshi Shintate, and Masataka Shirakashi. Ice/water slurry blocking phenomenon at a tube orifice. *Annals of the New York Academy of Sciences*, 972(1):171–176, 2002. [1.1](#)
- [20] Pavel G Struchalin, Vegar H Øye, Pawel Kosinski, Alex C Hoffmann, and Boris V Balakin. Flow loop study of a cold and cohesive slurry. pressure drop and formation of plugs. *Fuel*, 332:126061, 2023. [1.1](#), [4.3](#), [4.3](#), [4.4](#), [4.4](#)
- [21] Thomas J Danielson, Kris M Bansal, Ronny Hansen, and Emile Leporcher. Leda: the next multiphase flow performance simulator. In *BHR International Conference on Multiphase Production Technology*, pages BHR–2005. BHR, 2005. [1.1](#)
- [22] D Eskin, J Ratulowski, K Akbarzadeh, and S Pan. Modelling asphaltene deposition in turbulent pipeline flows. *The Canadian Journal of Chemical Engineering*, 89(3):421–441, 2011. [1.1](#)
- [23] M Labois, N Pagan, D Lakehal, and C Narayanan. Computational modelling of subsea hydrate formation and associated risks and impact on flow assurance. In *Proceeding of 10th International Conference on CFD in the Minerals and Process Industries (CFD-2014)*, 2014. [1.1](#)
- [24] Oleksii S Rukhlenko, Olga A Dudchenko, Ksenia E Zlobina, and Georgy Th Guria. Mathematical modeling of intravascular blood coagulation under wall shear stress. *PloS one*, 10(7):e0134028, 2015. [1.1](#)

- [25] Xianyu Yang, Shuya Chen, Yanping Shi, Ruimin Feng, Jihua Cai, and Guosheng Jiang. Cfd and dem modelling of particles plugging in shale pores. *Energy*, 174:1026–1038, 2019. [1.1](#)
- [26] Chengyun Ma, Yongcun Feng, Hai Lin, Jingen Deng, Xiaorong Li, and Fangrao Liu. Cfd-dem investigation of blocking mechanism in pre-packed gravel screen. *Engineering Analysis with Boundary Elements*, 132:416–426, 2021. [1.1](#)
- [27] Somnath Mondal, Chu-Hsiang Wu, and Mukul M Sharma. Coupled cfd-dem simulation of hydrodynamic bridging at constrictions. *International Journal of Multiphase Flow*, 84:245–263, 2016. [1.1](#), [4](#), [4.1](#)
- [28] Yachan Shao, Xuan Ruan, and Shuiqing Li. Mechanism for clogging of microchannels by small particles with liquid cohesion. *AIChE Journal*, 67(7):e17288, 2021. [1.1](#)
- [29] Shanlin Xu, Honglei Sun, Yuanqiang Cai, and Xueyu Geng. Studying the orifice jamming of a polydispersed particle system via coupled cfd–dem simulations. *Powder technology*, 368:308–322, 2020. [1.1](#)
- [30] Xu Duan, Bohui Shi, Junao Wang, Shangfei Song, Haotian Liu, Xuetong Li, Yuchuan Chen, Qingyun Liao, Jing Gong, Sihang Chen, et al. Simulation of the hydrate blockage process in a water-dominated system via the cfd-dem method. *Journal of Natural Gas Science and Engineering*, 96:104241, 2021. [1.1](#)
- [31] Zhiyuan Wang, Nan Ma, Jianbo Zhang, Jihao Pei, Shikun Tong, and Baojiang Sun. Numerical modeling of hydrate particle deposition in pipes with diameter reduction. *SPE Journal*, 28(02):522–539, 2023. [1.1](#)
- [32] Kaushik Manikonda, Abu Rashid Hasan, Chinemerem Edmond Obi, Raka Islam, Ahmad Khalaf Sleiti, Motasem Wadi Abdelrazeq, and Mohammad Azizur Rahman. Application of machine learning classification algorithms for two-phase gas-liquid flow regime identification. In *Abu Dhabi International Petroleum Exhibition and Conference*, page D041S121R004. SPE, 2021. [1.1](#)
- [33] Mayadah Alhashem. Machine learning classification model for multiphase flow regimes in horizontal pipes. In *International Petroleum Technology Conference*, page D023S042R001. IPTC, 2020. [1.1](#)
- [34] Majdi Chaari, Abdennour C Seibi, Jalel Ben Hmida, and Afef Fekih. An optimized artificial neural network unifying model for steady-state liquid holdup estimation in two-phase gas–liquid flow. *Journal of Fluids Engineering*, 140(10):101301, 2018. [1.1](#)
- [35] Hao Qin, Vishal Srivastava, Hua Wang, Luis E Zerpa, and Carolyn A Koh. Machine learning models to predict gas hydrate plugging risks using flowloop and field data. In *Offshore technology conference*, page D011S010R003. OTC, 2019. [1.1](#)
- [36] Jiguang Wang, Qi Wang, Yang Meng, Haiyuan Yao, Lunxiang Zhang, Bo Jiang, Zaixing Liu, Jiafei Zhao, and Yongchen Song. Flow characteristic and blockage

BIBLIOGRAPHY

- mechanism with hydrate formation in multiphase transmission pipelines: In-situ observation and machine learning predictions. *Fuel*, 330:125669, 2022. [1.1](#)
- [37] Juhyun Kim, Sunlee Han, Youngjin Seo, Bryan Moon, and Youngsoo Lee. The development of an ai-based model to predict the location and amount of wax in oil pipelines. *Journal of Petroleum Science and Engineering*, 209:109813, 2022. [1.1](#)
- [38] Menad Nait Amar, Ashkan Jahanbani Ghahfarokhi, and Cuthbert Shang Wui Ng. Predicting wax deposition using robust machine learning techniques. *Petroleum*, 8(2):167–173, 2022. [1.1](#)
- [39] Mohammadali Ahmadi. Data-driven approaches for predicting wax deposition. *Energy*, 265:126296, 2023. [1.1](#)
- [40] Nazerke Saparbayeva, Yu-Fen Chang, Pawel Kosinski, Alex C Hoffmann, Boris V Balakin, and Pavel G Struchalin. Cohesive collisions of particles in liquid media studied by cfd-dem, video tracking, and positron emission particle tracking. *Powder Technology*, 426:118660, 2023. [1.2](#), [4.2](#)
- [41] PA Cundall and ODL Strack. Discussion: A discrete numerical model for granular assemblies. *Géotechnique*, 30(3):331–336, 1980. [2.1](#)
- [42] ZY Zhou, SB Kuang, KW Chu, and AB2726154 Yu. Discrete particle simulation of particle–fluid flow: model formulations and their applicability. *Journal of Fluid Mechanics*, 661:482–510, 2010. [2.2.1](#), [2.2.2](#)
- [43] Siemens Digital Industries Software. Simcenter STAR-CCM+ User Guide v. 2020.1, Siemens 2020. [2.2.1](#), [2.2.1](#), [2.2.2](#), [2.2.3](#), [2.2.3](#), [2.2.3](#), [2.2.3](#), [2.2.3](#), [2.2.3](#), [2.2.3](#), [2.6](#), [2.6](#), [4](#), [5.1](#)
- [44] Pawel Kosinski. *Multiphase Flow with Solid Particles*. Cambridge University Press, 2023. [2.2.2](#), [2.2.2](#), [2.2.4](#), [2.4](#)
- [45] C. Crowe, M. Sommerfeld, and Y. Tsuji. *Multiphase Flow with Droplets and Particles*. CRC Press, 1998. [2.2.2](#), [2.2.2](#), [2.2.2](#), [2.2.2](#), [2.2.4](#), [2.3](#)
- [46] Nazerke Saparbayeva and Boris V Balakin. Cfd-dem model of plugging in flow with cohesive particles. *Scientific Reports*, 13(1):17188, 2023. [2.2.2](#), [4.3](#)
- [47] M Sommerfeld et al. Theoretical and experimental modelling of particulate flows. *Lecture series*, 6:3–7, 2000. [2.2.2](#), [2.2.2](#)
- [48] Aslak S Hellestø, Maryam Ghaffari, Boris V Balakin, and Alex C Hoffmann. A parametric study of cohesive particle agglomeration in a shear flow—numerical simulations by the discrete element method. *Journal of Dispersion Science and Technology*, 38(5):611–620, 2017. [2.2.3](#)
- [49] Kenneth Langstreth Johnson and Kenneth Langstreth Johnson. *Contact mechanics*. Cambridge university press, 1987. [2.2.3](#)

- [50] Sung-oh Yang, Derek M Kleehammer, Zhongxin Huo, E.Dendy Sloan, and Kelly T Miller. Temperature dependence of particle–particle adherence forces in ice and clathrate hydrates. *Journal of Colloid and Interface Science*, 277(2):335–341, 2004. [2.2.3](#), [4.2](#), [4.3](#)
- [51] GG Joseph, R Zenit, ML Hunt, and AM Rosenwinkel. Particle–wall collisions in a viscous fluid. *Journal of Fluid Mechanics*, 433:329–346, 2001. [2.2.4](#)
- [52] Boris V Balakin, Kirill V Kutsenko, Alexey A Lavrukhin, and Pawel Kosinski. The collision efficiency of liquid bridge agglomeration. *Chemical Engineering Science*, 137:590–600, 2015. [2.2.4](#)
- [53] Louis M Reitter, Andreas Mayrhofer, Cameron Tropea, and Jeanette Hussong. Experimental investigation of normal and oblique impact of ice particles onto a wetted wall. In *AIAA AVIATION 2022 Forum*, page 3533, 2022. [2.2.4](#)
- [54] Thermophysical properties of decane. NIST chemistry webbook. <https://webbook.nist.gov/cgi/fluid.cgi?ID=C124185Action=Page>. Accessed: 2022-11-24. [2.2.4](#)
- [55] Sergiy Sukhorukov. Ice-ice and ice-steel friction in field and in laboratory. 2013. [2.2.4](#)
- [56] John David Anderson and John Wendt. *Computational fluid dynamics*, volume 206. Springer, 1995. [2.3](#), [2.3](#)
- [57] Pham Chi Vinh and RW Ogden. On formulas for the rayleigh wave speed. *Wave Motion*, 39(3):191–197, 2004. [2.6](#)
- [58] AV Pichugin. Approximation of the rayleigh wave speed. *Unpublished draft*, 2008. [2.6](#)
- [59] S Timoshenko and JN Goodier. *Theory of elasticity*” mcgraw-hill book company. Inc. New York, 1951. [2.6](#)
- [60] Arundhati Navada, Aamir Nizam Ansari, Siddharth Patil, and Balwant A Sonkamble. Overview of use of decision tree algorithms in machine learning. In *2011 IEEE control and system graduate research colloquium*, pages 37–42. IEEE, 2011. [3](#)
- [61] Leo Breiman. Random forests. *Machine learning*, 45:5–32, 2001. [3](#)
- [62] Cross-validation: evaluating estimator performance. https://scikit-learn.org/stable/modules/cross_validation.html#k-fold. [3](#)
- [63] Guillaume Dumazer and Étienne Gagnepain. Hydraulic transport regimes of grains in a millifluidic confinement. In *EPJ Web of Conferences*, volume 249, page 09013. EDP Sciences, 2021. [4.1](#)
- [64] B Balakin. personal communication. [5.1](#), [5.2.2](#)

BIBLIOGRAPHY

- [65] Boris V Balakin, Alex C Hoffmann, Pawel Kosinski, and Lee D Rhyne. Eulerian-eulerian cfd model for the sedimentation of spherical particles in suspension with high particle concentrations. *Engineering Applications of Computational Fluid Mechanics*, 4(1):116–126, 2010. [5.2.1](#), [5.2.1](#)
- [66] BV Balakin, AC Hoffmann, and PJ Kosinski. Experimental study and computational fluid dynamics modeling of deposition of hydrate particles in a pipeline with turbulent water flow. *Chemical Engineering Science*, 66(4):755–765, 2011. [5.2.2](#)
- [67] Madina Naukanova, Gianluca Lavalle, Jean-Michel Herri, Ana Cameirao, Pavel G Struchalin, and Boris V Balakin. Viscosity of ice-in-oil slurries. *International Journal of Refrigeration*, 150:41–46, 2023. [5.2.2](#)

Part II

ARTICLES

SIMULATION OF HORIZONTAL HYDRAULIC CONVEYING AND DUNE FORMATION BASED ON CFD-DEM

Nazerke Saparbayeva, Pawel Kosinski, Guillaume Dumazer, Marc Fischer, and Boris V. Balakin

In AIP Conference Proceedings of ICNAAM 2022 (in press).

Simulation of horizontal hydraulic conveying and dune formation based on CFD-DEM

Nazerke Saparbayeva,^{1, a)} Pawel Kosinski,² Guillaume Dumazer,³ Marc Fischer,³ and Boris V. Balakin¹

¹⁾Department of Mechanical and Marine Engineering, Western Norway University of Applied Sciences, Inndalsveien 28, 5063 Bergen, Norway.

²⁾Department of Physics and Technology, University of Bergen, Norway.

³⁾Mines de Saint-Etienne, CNRS, UMR 5307 LGF, Centre SPIN, F-42023 Saint Etienne, Universite de Lyon, France

^{a)}Corresponding author: Nazerke.Saparbayeva@hvl.no

Abstract.

In this paper, the horizontal hydraulic conveying and dune formation in a millifluidic tube was simulated by the coupled computational fluid dynamics/discrete element method (CFD-DEM) method. The simulations were performed using experimental data sets with the commercial package Star-CCM+. The interaction between the water flow and the particles of glass beads with a diameter of 100 μm was considered using a two-way interaction strategy. Laminar flow with a concentration of particles around 28% was simulated for the 2 ml/min flow rate value at different restitution coefficients. The flow characteristics of the hydraulic conveying in a horizontal pipe, such as dune velocity and length, were considered in detail. The model was validated against an experimental benchmark. Based on the simulation data, the formation of dunes is well predicted by the model. The anticipated results correlate qualitatively with the experimental data with a 10.7% discrepancy for the dune velocity. This work demonstrates that CFD-DEM is a promising approach to studying hydraulic conveying regimes in a horizontal channel.

INTRODUCTION

Hydraulic transport has many industrial applications. Therefore, significant efforts have been made to implement and evaluate the computational fluid dynamics - discrete element method (CFD-DEM) coupling method for describing transport systems. For instance, Zhou et al. [8] used CFD-DEM to study the flow regimes during the hydraulic transport. This combined numerical approach was also used to model pneumatic transport [6]. A CFD-DEM model was also developed by Zhao et al. [7] to investigate the pneumatic conveying in a horizontal pipe with further application of the wall roughness (WR) and discrete random walk (DRW) method. Even though the discrete method offers promising perspectives to model particulate hydraulic transport, the application of this numerical method remains limited. Besides, detailed characteristics of dunes, which are most often called slugs in the context of pneumatic transport, are seldom investigated using discrete numerical methods.

Therefore, in the present paper, we consider the combined CFD-DEM model of horizontal hydraulic conveying to predict dune formation. In the simulations, we applied the Eulerian-Lagrangian method, which tracks each particle and computes related forces. Eventually, experimental measurements of Dumazer and Gagnepain [3] were compared with the model predictions.

MODEL

The numerical model was built in an Eulerian-Lagrangian framework [5], where the flow of the continuous phase is described by solving the Navier-Stokes equations [2]:

$$\nabla \vec{u} = 0, \quad (1)$$

$$\rho_f \left[\frac{\partial \vec{u}}{\partial t} + \vec{u} \nabla \vec{u} \right] = -\nabla p + \mu \nabla^2 \vec{u} - \vec{f}_{p,\Sigma}, \quad (2)$$

where \vec{u} is the fluid velocity, ρ_f , and μ are the continuous phase density and viscosity, respectively, and p is the pressure.

The last term in equation (2) is the drag force acting on an individual particle [2]:

$$\vec{f}_{p,i} = \frac{\pi}{2} R_{0,i}^2 C_{D,i} \rho_c (\vec{u} - \vec{v}_i) |\vec{u} - \vec{v}_i|, \quad (3)$$

where $R_{0,i}$ is the radius and \vec{v}_i is the velocity of the i^{th} particle, and C_D is the drag force coefficient. Thus, the integrated drag force is given by:

$$\vec{f}_{p,\Sigma} = \sum_{i=1,N_1} \vec{f}_{p,i}/V, \quad (4)$$

where N_1 is the total number of particles in a computational cell with volume V . Newton's second law describes the linear motion of the discrete phase:

$$m_i \frac{d\vec{v}_i}{dt} = \vec{f}_{p,i} + \sum_{j=1,N_2} \vec{f}_{i,j}, \quad (5)$$

where m_i is particle mass, and $\vec{f}_{i,j}$ are the forces acting on the i -th particle due to contact with N_2 other particles. The particle rotation is calculated as:

$$\frac{d}{dt} (I_i \vec{\omega}_i) = \sum_{j=1,N_2} \vec{T}_{i,j}, \quad (6)$$

where I_i is the particle moment of inertia, $\vec{\omega}_i$ is the angular velocity and $\vec{T}_{i,j}$ is the torque given by $\vec{r} \times \vec{F}_{i,j}$.

The contact forces are computed via Hertz–Mindlin contact model. This model is available in a variety of CFD codes. The contact model built in STAR-CCM+ was successfully validated for similar systems [4]:

$$F_{i,j}^{(n)} = -K^{(n)} \delta^{(n)} - N^{(n)} \mathbf{v}_{rel;i,j}^{(n)}, \quad (7)$$

where $F^{(n)}$ is the contact force in the normal direction to the plane of collision. $K^{(n)}$ is the stiffness in the normal direction of a “spring” that mimics the deformation process. Also, $\delta^{(n)}$ is the inter-particle overlap distance as it would be if the particles were undeformed. Finally, $N^{(n)}$ is the damping coefficient in the normal direction. The stiffness of the spheres depends on the mechanical properties of the particles. In contrast, the damping coefficient depends on their coefficients of mechanical restitution, which is the ratio of the final to the initial relative velocity between two objects after their collision [2]. The tangential component of the contact force is calculated similarly. In the expression for the tangential component, the static coefficient of friction is used [4].

In this study, we sought to reproduce numerically the experiments by Dumazer and Gagnepain [3] where glass spheres were transported by flow in a cylindrical 2-mm diameter pipe. Following the experiments, a stationary deposit occupies the lower half of the pipe diameter. Therefore, we do not consider the lower half of the pipe in the model to avoid facing enormous computational times. We reduced the geometry to a rectangular conduit with a height equal to 1 mm in order to obtain qualitative results. The pipe length was 20 cm. The width of the channel was set to three-fold the particle size. The spherical particle size was 100 μm as used in the experiments.

The equations were solved numerically via the SIMPLE algorithm. The Euler implicit unsteady technique with $5.0 \cdot 10^{-4}$ s time step was used to progress in time and the computational domain was discretized into 5344 control volumes. The flow was laminar with no-slip wall boundary conditions for horizontal edges, while periodic boundaries were used at the vertical edges (see Figure1). The initial flow rate of the fluid was 2 ml/min, and the restitution coefficient was 0.70, 0.80, and 0.98. The number of injected particles was determined according to the experimentally measured transport rate of 0.19 g/min. The particles were removed straightforwardly from the domain while streaming out of the outlet. The physical properties of glass beads and water in normal conditions were used in the model.

RESULTS AND DISCUSSION

In the numerical model, corresponding to the aforementioned volume flow rate of 2 ml/min, the inlet velocity of the fluid phase was set to $u = 0.021$ m/s. The low speed of transportation leads to the deposition of particles formed at the

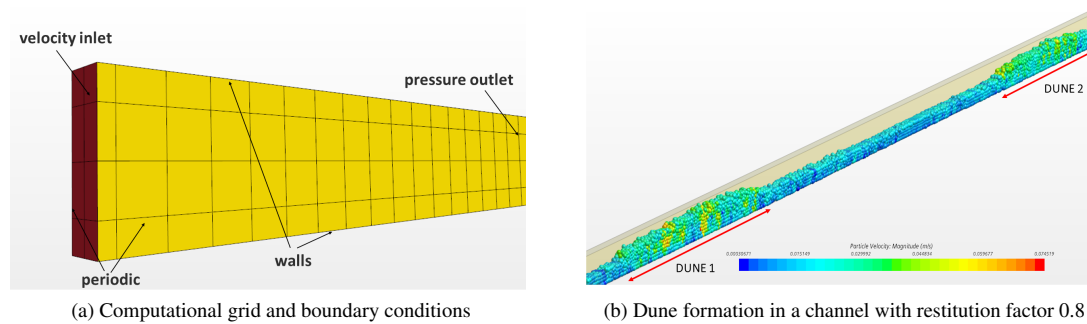


FIGURE 1: Numerical model

bottom of the microchannel. Figure 1 shows the velocity of particles in the channel. The lowest velocities correspond to particles closer to the bottom wall of the pipeline, while the uppermost ones have a high velocity. The model also demonstrated the formation of dunes above the particle layer (see Figure 1). This process reproduces experimental observations. The saltation of the particles is the primary reason for the formation of dunes [1].

Further, we compared the influence of the restitution coefficient. Also, the simulation results for hydraulic conveying in a horizontal pipe were validated against the experimental measurements. In Figures 2 and 3, we present how the length of the dune and the dune velocity depend on the particle restitution coefficient. The dune velocity is found as an average velocity of the particles within a tip of a dune, and further averaged over all the formed dunes. Following the experimental observations, we identify the tip of the dune as a compaction of particles residing in the computational cells that are adjusted to the top wall of the tube. It may be deduced from the plots that fewer particles deposit with an increase in the restitution factor. Therefore, the size of the dunes decreases. The plot was also used to validate the numerical results with the experiments by Dumazer and Gagnepain [3]: for the flow rate of 2 ml/min, the experimental dune's length was 29.5 mm. By implementing this result into Figure 2 (denoted as a dot), we can predict the coefficient of restitution from the experiments to be around 0.74. From the experiments by Dumazer and Gagnepain [3], we also know that the dune's velocity was 25 mm/s. By selecting the same coefficient of restitution and comparing it with the results depicted in Figure 3, we see a discrepancy of 10.7%. Thus, the results from the simulations confirm that the constructed CFD-DEM model can generate a reasonable qualitative agreement with the experimental data.

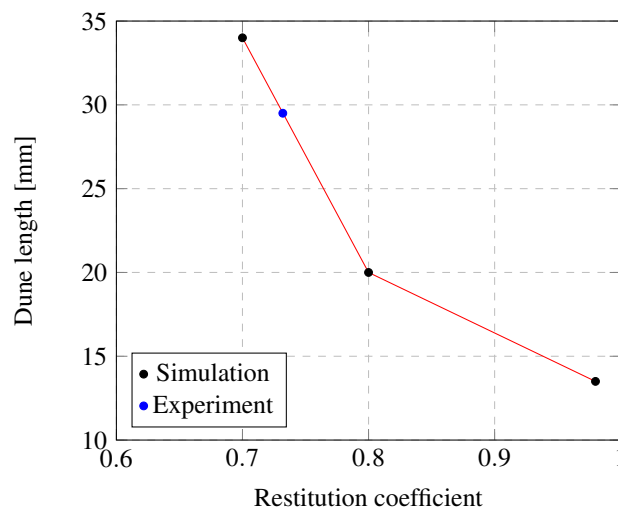


FIGURE 2: Dune length as a function of restitution coefficient. The blue point indicates the mean dune length obtained experimentally for 2 ml/min in Dumazer and Gagnepain [3].

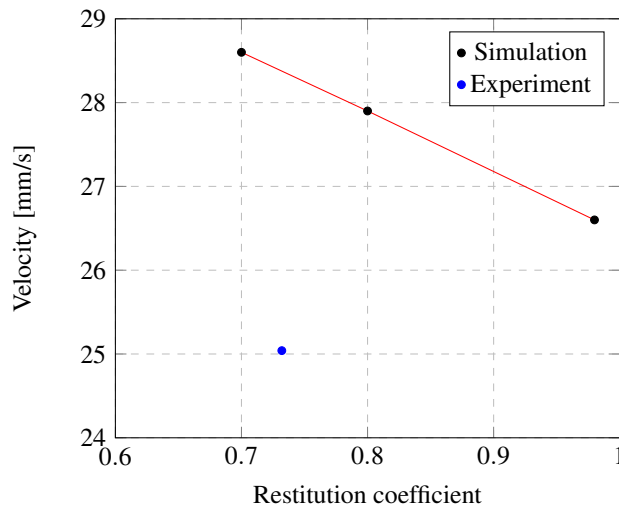


FIGURE 3: Dune velocity as a function of restitution coefficient. The blue point indicates the mean dune speed obtained experimentally for 2 ml/min in Dumazer and Gagnepain [3].

CONCLUSION

CFD-DEM computational model of hydraulic conveying was implemented to predict dune formation in a horizontal pipe. The main objective of the work was to validate the CFD-DEM model against experimental data using the commercial software Star-CCM+. We could qualitatively simulate the formation of dunes which occurs via saltation. The dune's average velocity and length were used as the main parameter for verification. The dune length predicted by the numerical model could be fitted to the experimental one by varying the coefficient of restitution. In contrast, the predicted dune velocity was larger than the measured one. These discrepancies could be because we had to simulate a rectangular conduit half as high as the real cylindrical conduit for the sake of computational time.

In future studies, it would be worthwhile to extend our simulations to investigate the statistics of the length and velocity of dunes. Also, it is necessary to look into other variables, such as the delay time between the appearance of dunes at a given point in space.

ACKNOWLEDGMENTS

This study was supported by the Research Council of Norway (project 300286).

REFERENCES

1. Ralph Alger Bagnold. *The physics of blown sand and desert dunes*. Courier Corporation, 2012.
2. C. Crowe, M. Sommerfeld, and Y. Tsuji. *Multiphase Flow with Droplets and Particles*. CRC Press, 1998.
3. Guillaume Dumazer and Étienne Gagnepain. Hydraulic transport regimes of grains in a millifluidic confinement. In *EPJ Web of Conferences*, volume 249, page 09013. EDP Sciences, 2021.
4. Aslak S Hellestø, Maryam Ghaffari, Boris V Balakin, and Alex C Hoffmann. A parametric study of cohesive particle agglomeration in a shear flow—numerical simulations by the discrete element method. *Journal of Dispersion Science and Technology*, 38(5):611–620, 2017.
5. Catalin G Ilea, Pawel Kosinski, and Alex C Hoffmann. Dust lifting simulations with particles of distributed sizes. In *AIP Conference Proceedings*, volume 936, pages 631–634. American Institute of Physics, 2007. doi:10.1063/1.2790227.
6. J. Li, C. Webb, S.S. Pandiella, G.M. Campbell, T. Dyakowski, A. Cowell, and D. McGlinchey. Solids deposition in low-velocity slug flow pneumatic conveying. *Chemical Engineering and Processing: Process Intensification*, 44(2):167–173, 2005. ISSN 0255-2701. doi: 10.1016/j.cep.2004.02.011. Pneumatic Conveying and Handling of Particulate Solids.
7. Hemin Zhao and Yongzhi Zhao. CFD-DEM simulation of pneumatic conveying in a horizontal pipe. *Powder Technology*, 373:58–72, 2020. ISSN 0032-5910. doi:10.1016/j.powtec.2020.06.054.

8. Mengmeng Zhou, Shibo Kuang, Kun Luo, Ruiping Zou, Shuai Wang, and Aibing Yu. Modeling and analysis of flow regimes in hydraulic conveying of coarse particles. *Powder Technology*, 373:543–554, 2020. ISSN 0032-5910. doi:10.1016/j.powtec.2020.06.085.

COHESIVE COLLISIONS OF PARTICLES IN LIQUID MEDIA STUDIED BY CFD-DEM, VIDEO TRACKING, AND POSITRON EMISSION PARTICLE TRACKING

Nazerke Saparbayeva, Yu-Fen Chang, Pawel Kosinski, Alex C. Hoffmann, Boris V. Balakin, Pavel G. Struchalin

Powder Technology, Elsevier. **426**, 118660 (2023)



Cohesive collisions of particles in liquid media studied by CFD-DEM, video tracking, and Positron Emission Particle Tracking

Nazerke Saparbayeva^{a,*}, Yu-Fen Chang^{a,b}, Pawel Kosinski^c, Alex C. Hoffmann^c, Boris V. Balakin^a, Pavel G. Struchalin^a

^a Western Norway University of Applied Sciences, Department of Mechanical and Marine Engineering, Bergen, Norway

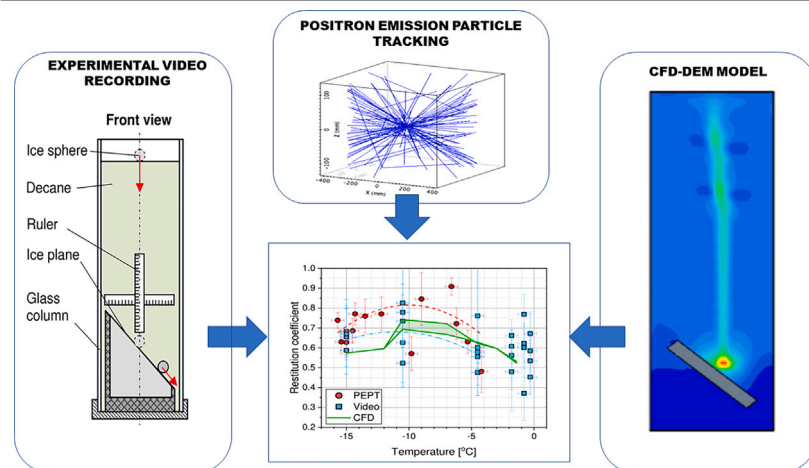
^b UiT The Arctic University of Norway, Department of Clinical Medicine, Tromsø, Norway

^c University of Bergen, Department of Physics and Technology, Bergen, Norway

HIGHLIGHTS

- We consider ice-ice interaction in decane from $-15.7\text{ }^{\circ}\text{C}$ to $-0.3\text{ }^{\circ}\text{C}$.
- 4.7 mm particles collide on the inclined ice surface.
- Video & PEPT reveal particle motion.
- CFD-DEM simulations match experimental data.
- Coefficient of restitution peaks around $-10.0\text{ }^{\circ}\text{C}$ temperature.

GRAPHICAL ABSTRACT



ARTICLE INFO

Keywords:

CFD-DEM

Cohesion

Ice slurry

Coefficient of restitution

STAR-CCM+

ABSTRACT

This paper investigates the cohesive collision of ice in an oil phase at temperatures ranging from $-15.7\text{ }^{\circ}\text{C}$ to $-0.3\text{ }^{\circ}\text{C}$. The new information on the coefficient of restitution (COR) was obtained using three different velocity measurement methods: high-speed experimental video recording, Positron Emission Particle Tracking (PEPT), and numerical simulations. A new type of PEPT tracer was developed for the experiments. The COR values were in the interval 0.57...0.82, with a maximum at around $-10\text{ }^{\circ}\text{C}$. The CFD-DEM coupled approach was applied to reproduce experiments with an ice particle drop and its collision with an inclined ice surface in a decane. The particle-wall interaction is modeled using commercial software, considering particle cohesion, particle size, and shape. CFD-DEM predicted the COR with an average deviation $\sim 10\%$ from the experimental data. The numerical model's results agree with the experiments, demonstrating that the CFD-DEM method is suitable for describing multiphase cohesive interactions.

* Corresponding author.

E-mail address: nazerke.saparbayeva@hvl.no (N. Saparbayeva).

<https://doi.org/10.1016/j.powtec.2023.118660>

Received 17 January 2023; Received in revised form 18 April 2023; Accepted 13 May 2023

Available online 18 May 2023

0032-5910/© 2023 The Author(s). Published by Elsevier B.V. This is an open access article under the CC BY license (<http://creativecommons.org/licenses/by/4.0/>).

1. Introduction

The hydraulic transport of ice particles is essential in energy and powder technology as ice slurries are effective coolants and phase change materials [1]. They are also used in the construction sector [2]. A majority of commercial ice slurries use aqueous media to disperse ice [3], which makes them hardly applicable in systems where repeated cycles of melting and solidification are expected since molten particles dissolve in the carrier liquid. To tackle this issue, Matsumoto et al. [4] proposed an oil-based ice slurry capable of turning to emulsion when melting and restoring the suspension of solid particles at temperatures less than 0 °C. Moreover, oil-based slurries are additionally crucial in petroleum technology as ice particles constitute suitable models of gas hydrates [5]. However, once dispersed in an oil phase, ice particles increase their cohesion due to the formation of liquid films at their surface [6]. Pumping an oily slurry through process equipment could become a challenging problem due to the cohesive interactions of ice particles. Their mutual collisions can lead to agglomeration, formation of deposits, and plugging [7].

Several complex phenomena govern the collisions of ice particles in the oil. Attractive cohesion [6] competes with repulsive lubrication forces [8], which are induced by oil and water squeezed out between the colliding surfaces. Mechanical deformation and surface friction of particles during contact dissipate a significant share of their relative energy before the collision [8]. The viscous phase can also influence the process via, e.g., the formation of wakes [9], turbulence [8], thermal convection, and partial slip [10]. In most cases, the shape [11] and the roughness [12] of particles may become crucial.

A simplified approach to characterize particle collisions is to define a coefficient of restitution (COR) [13], i.e., the square root of the ratio of kinetic energy before the collision (E_{k1}) to the kinetic energy after the collision (E_{k2}) [8]. Numerous works are considering the COR of ice particles in a vacuum/gaseous media [14–17]. Dealing with high-impact velocities, they primarily focus on aerospace applications where a particle may crack during the impact. Higa et al. [15] determined the restitution coefficient of ice particles impacting an ice block in the normal direction. The experiments were carried out in vacuum conditions, temperatures above 120 K, and impact velocities from 1 to 10 m/s. The restitution coefficient was based on the linear velocities of the particles determined with a high-speed camera. They found that the restitution coefficient was about 0.9 for velocities below 1 m/s and temperatures below 245 K. Increasing the temperature, the COR progressively reduced to zero at 237 K due to the formation of liquid films at the surface of the ice.

Reitter et al. [17] used a high-speed camera to identify the influence of liquid films and impact angles on the COR for ice particles in the air. They found that COR for normal collisions reduced with the particle Stokes number and the thickness of the film. At the same time, COR for oblique collisions did not alter significantly and was in the interval of 0.8–0.9. Once the so-far-determined ice CORs provide valuable input for the analysis of cohesive slurries, the experiments did not yet account for the influence of the continuous phase. In addition, the used ice particles were not spherical and, depending on an initial orientation, could rotate after the impact. This was not considered in their studies.

Although a limited number of factors influencing the collision of ice particles have been considered, there is a wider knowledge base describing collisions of metals, oxides, and semiconductors [18]. Collisions of wet particles were studied in Antonyuk et al. [19] and Muller et al. [20]. The experimental results demonstrated that COR was dependent on the thickness of the liquid layer covering the particles [20], the viscosity of the ambient media [21], the impact velocity [19], the viscosity and the surface tension of the liquid film, and the size of the colliding particles [19]. Hastie et al. [22] considered COR for objects of irregular shape. The influence of natural [18] and artificial roughness [23] on the COR was considered for different impact velocities. It was found that an increased roughness reduces the COR in the

air. However, as has been recently reported by Krull et al. [24], COR increases with the height of the roughness when the impact happens in liquid media. This is most possibly connected to an altered slip at the tips of the roughness reducing the viscous lubrication [10].

A majority of the conducted COR tests study collisions using high-speed video tracking. Despite the method's accuracy, there are inherent limitations of the technique. To follow a three-dimensional motion of the colliding particles, which is highly relevant for objects of an irregular shape, at least two cameras are required. Direct optical access to the process demands transparency of the studied system, which is hardly compatible with industrial conditions where pressurized, semi-transparent, and often chemically aggressive media are used. A promising alternative experimental technique was proposed by Oesau et al. [11]. The authors studied CORs of colliding particles using the magnetic particle tracking method based on continuous sensing of a dipole magnet. After comparison with standard high-speed video tracking, the method demonstrated surprisingly high accuracy and repeatability of the results. However, the technique requires magnetic tracer particles, which limit the selection of the tested materials. Another limitation is a restriction for using ferromagnetic materials other than tracers. This again reduces the industrial relevance of the studied phenomena and the process equipment that consists of this kind of material.

In light of the discussed limitations, another method involving radioactivity could be more applicable to studying cohesive collisions of ice. Positron emission particle tracking (PEPT) was pioneered at the University of Birmingham [25–28]. This technique allows tracking a particle moving through a process located in the field of view (FOV) of a 3D detector array. PEPT has been an advantageous experimental method for validating and advancing computational fluid dynamics (CFD). The method uses the radioactive decay of a suitable isotope with which a tracer particle is labeled. In this work, Fluorine-18 (^{18}F) gives rise to the emission of a positron that travels a small distance through the medium until it annihilates with an electron, resulting in a back-to-back emission of two photons of 511 keV each. A straight line between two detectors receiving the photon pair of the same annihilation event (i.e., both within a very narrow time window) defines a “line of response” (LOR). This indicates that the annihilation event must have occurred somewhere along this line. From this, algorithms processing many LORs within a short time interval allow the determination of the centroid of the tracer particle. The accuracy of positioning the particle depends mainly on the algorithm and the activity of the tracer particle. Scatter is inherent in the process, and the reasons for this are discussed in Bailey et al. [29] and Chang et al. [30].

PEPT has been utilized to acquire particle motion, settling, and collision in various processes to overcome the limitations of optical methods, such as particle tracking velocimetry (PTV), which works only with an optically transparent system that is unavailable in many cases. PEPT results can therefore reveal the otherwise undetectable information, which can be further compared with the computational models. For instance, Cole et al. [31] analyzed the PEPT tracer particle velocity to deduce information on local foam structure and events, such as coalescence, to study the structure in flotation froths and to improve the CFD models of flotation. In Cole et al. [31], a 70 μm alumina particle labeled with ^{18}F was tracked with a temporal resolution of approximately 7.5 ms during its ascent and descent in a foam column. PEPT was also applied to study the effect of two and three spouts on the flow dynamics in a pseudo-2D fluidized bed, where the depth of the bed was assumed to be sufficiently small to display pseudo-2D behavior [32]. A 3 mm glass bead labeled with ^{18}F was tracked with a temporal resolution of 3–10 ms. A discrete particle model (DPM) that describes the dynamics of the continuous gas phase and particles was used to simulate 3D fluidized beds. A soft sphere approach was used to describe inter-particle collisions. The results of PEPT agreed very well with the instantaneous 2D velocity data obtained by PTV. However, the DPM simulations overpredicted the particle velocity in the annulus

of the fluidized bed. This deviation was likely due to wall effects that are more pronounced in pseudo-2D beds than in 3D systems, which are not treated with sufficient accuracy in DPM. Although PEPT has never been used before for studying adhesive collisions of ice, our group has recently developed a method to produce radioactive ice tracers for this purpose [33].

Based on the discussed experimental studies, we conclude that the coefficient of restitution is not a universal parameter describing the cohesive collisions of ice in oil. The influence of particle surface properties, together with the behavior of the oil phase, alters the coefficient of restitution significantly. Another difficulty comes from the experimental method itself, as the existing techniques are not entirely applicable to the desired process. Theoretical studies of the problem could shed light on those missing phenomena, but there are not many papers published on the matter. Chen et al. [34] performed a CFD study of the collision of a particle with the wall in a viscous medium. In their work, solid particles were modeled as Lagrangian objects using the discrete element method (DEM) to describe the particle-wall interaction [35]. After experimental validation of the model, we consider how the properties of the liquid phase influenced the contact forces during the collision. However, this model did not account for such important factors as lubrication and cohesion. A series of CFD-DEM models devoted to cohesive gas hydrates was published during the last decade [35–37]. In these works, standard collision models built in commercial CFD codes were used to model multiple interactions among particles and with walls. Although some of the models complied with theoretical correlations for agglomeration in cohesive suspension [35], they were applied without considering how realistically they reproduced individual contacts. The lubrication forces were not taken into account there either.

The primary objective of this paper is to provide a detailed physical description of the process of cohesive collisions of ice in an oily dispersed phase. We start with experimental studies of the process at different temperatures and, therefore, different cohesion, using video tracking and PEPT of radioactive ice particles. The next stage is developing a CFD-DEM model accounting for the majority of factors missing in similar studies and validating the model against our experimental data.

2. Methodology

2.1. Experimental system

Cohesive collisions of ice in oil were studied by letting an ice particle impact onto an inclined ice surface immersed in decane (Sigma Aldrich >95%). For this, the ice surface (inclined at the angle of 45°) was placed in a holder within a vertical cylindrical column filled with decane (Figs. 1, 2A). The column was made of a cylindrical pipe (borosilicate glass 3.3) sandwiched between steel (SS 304) flanges with ports equal to the inner diameter of the pipe (42 mm). A plastic plug holding the ice surface was inserted into the lower flange. The resulting distance along the central vertical axis from the upper edge of the column to the ice surface was 260 mm. The total column height was 360 mm, and the diameter was less than 88 mm.

In the PEPT experiments, the column was covered with 17-mm thick EPE foam thermal insulation. During the experiments, the column was fixed on a tripod, and during the video track, a scale was placed near the column. The column was kept at temperatures below the ice melting point and thermally stabilized. An ice particle held in the upper decane layer was released without initial velocity and fell onto the ice surface. The entire settling process was registered to determine the instantaneous velocities of the particle both before and after the collision with the surface. As a final result, based on the particle velocity history and assuming that the particle was nearly-spherical, the ice-in-oil restitution coefficient was determined as (1):

$$\epsilon = \sqrt{\frac{E_{k2}}{E_{k1}}} \sim \sqrt{\frac{v_2^2 + 0.1\omega^2 d^2}{v_1^2}}, \quad (1)$$

where E_{k1} , E_{k2} are the particle kinetic energies and v_1 , v_2 are particle linear velocity before and after a collision respectively, ω is a particle angular velocity after collision. The particle kinetic energy of rotation before the collision is absent in Eq. (1) since no significant rotation of the particles was detected before the collisions. It is also shown in Section 3.1.

In the laboratory experiments, the particle tracking was done using a high-speed video camera (Sony IMX586 Exmor RS, 48MPx, f/1.79, 240 fps). The focal plane of the lens was aligned with the inclined ice surface. This made it possible to determine the collision moment between the ice particle and the surface.

The ice particles and the inclined ice surface were produced the same way, both for laboratory tests and tests with the PEPT scanner. The ice surface was made by freezing water in a holder at –25 °C. We used tap water for all the experiments, and its chemical composition is presented in the Supplementary materials. After the ice was formed, the surface facing the falling particle was exposed to a warm aluminium plate to form a flat surface at the required angle. The holder edges have the same inclination angle (45°). So, during partial melting, the ice surface is aligned with the edges, achieving the required inclination. After melting, the ice surface was covered with a polished polyethylene plate and placed back in the freezer at the same temperature to freeze the residual water layer between the ice and the plate. This allowed the formation of a flat ice surface. Due to the low adhesion of ice to polyethylene, the plate could be removed without damaging the ice surface.

Ice particles were made of water taken at room temperature. To do this, 80 µl of water were drawn into a standard mechanical pipette (Thermo Scientific Finnpiptette EH81075 4500 mechanical pipette 10–100 µl). The pipette was equipped with a standard plastic tip, which was cut to increase the diameter of the tip's outlet hole and to doze out the required volume of water. The pipette tip was immersed in decane at a temperature between –17 and –19 °C. This was done in a supplementary vertical column, as mentioned above, but without the inclined surface. The column had a bottom ball valve to remove the produced ice particles. Ten seconds after the pipette tip was immersed in the cold decane, the water was slowly injected into the decane and formed a single drop. When the drop fell, an ice shell was formed, retaining the shape of a particle close to spherical and holding the rest of the non-crystallized water inside. The crystallization of the remaining water occurred when the drop was at the bottom of the column. Then a new portion of water was taken, and the production process was repeated. Three to five particles were produced at a time. After that, the ball valve at the bottom of the column was opened, and the particles, together with some amount of decane, were extracted into a 400 ml beaker. The beaker was tilted so that the decane with particles fell down along the wall without a substantial impact on the beaker's bottom. At least 60% of the particles from one production procedure remained intact and undamaged. The rest of the particles were destroyed in the process due to high internal mechanical stresses caused by the expansion of water during crystallization inside the pre-formed ice shell. The resulting particles had a shape very close to spherical, with a diameter $d_i = 2r_i = 4.7 \pm 0.3$ mm. Their typical appearance is shown in Fig. 2B.

The produced particles were stored in a decane and were retrieved from it only for use in the main experiment. Prior to this, the temperatures of the decane in the main column and in the beaker were equalized. The temperatures of decane at all the stages of ice particle production and the experiments were controlled by immersed K-type thermocouples ($\pm 0.1^\circ\text{C}$) connected to the RS-42 RS PRO thermometer.

The settling of the particle in a column was analyzed from the recorded video. The linear velocity of a particle was determined from the difference in the coordinates of its geometric center. The coordinates were determined relative to the chosen zero mark on the ruler placed near the ice surface inside the column. For that, the X-Y coordinate system defined in Fig. 2 was used. The processing of the two

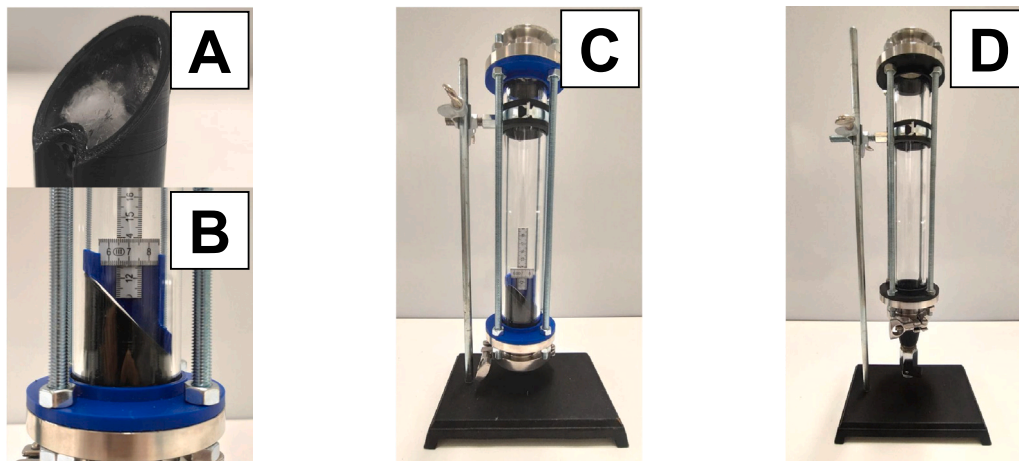


Fig. 1. Photos of the glass columns. The ice surface in a plastic holder (A), its position within a glass column (B), the main column for the drop (C), and the supplementary column for the ice sphere production (D).

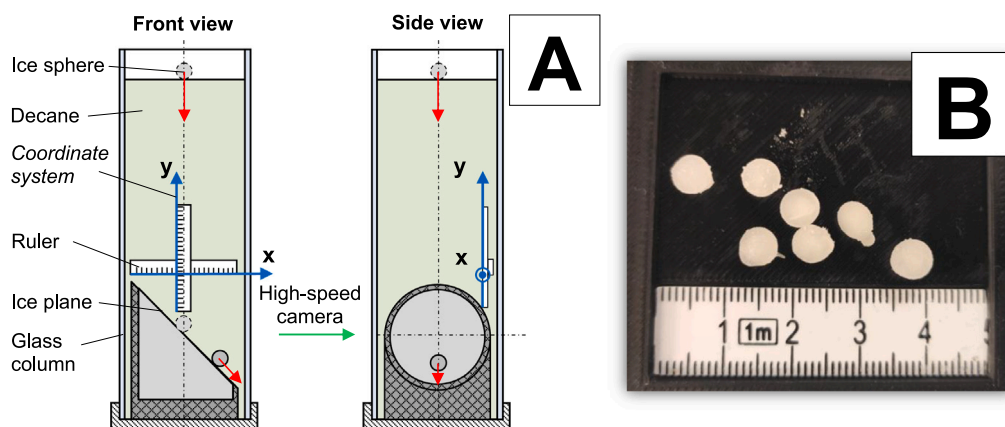


Fig. 2. Experimental set-up (A) and appearance of the ice particles (B).

frames taken at a known time interval τ made it possible to determine the displacement of the particle by a set of initial and final coordinates $(x_1, y_1), (x_2, y_2)$ and calculate its velocity as $v = [(x_2 - x_1)^2 + (y_2 - y_1)^2]^{0.5} / \tau$. The rotational velocity, ω , was determined using the rotational angle α of a line passing through the center of an ice sphere as $\omega = \alpha / \tau$. The time interval was limited to $\tau = 150$ ms, corresponding with the particle's momentum response time [8]. To process the frames and determine the particle coordinates, we used the Grafula 3 software.

We note that our method of velocity determination contains a methodological uncertainty, leading to an underestimation of the instantaneous linear velocity due to its unknown component in the third direction perpendicular to the focal plane of the camera. However, this error did not make a significant contribution. Considering the system to be axisymmetric and assuming the probability of particle motion in all horizontal directions to be the same, the unknown horizontal velocity component could be estimated. The unaccounted particle velocity component underestimated its average absolute value at 0.43% and a maximum value of 2.13%.

The uncertainties of linear velocities in the laboratory tests were determined as $\Delta v = [(\Delta x \cdot \partial v / \partial x)^2 + (\Delta y \cdot \partial v / \partial y)^2 + (\Delta \tau \cdot \partial v / \partial \tau)^2]^{0.5}$ where the uncertainties of the particle coordinates and the time step are $\Delta x, \Delta y = \pm 0.5$ mm and $(\Delta \tau = \pm 4.2$ ms, correspondingly. The uncertainty of the ratio of the linear velocities $V R = v_2 / v_1$ is taken as $\Delta V R = [(\Delta v_2 \cdot \partial \Delta V R / \partial v_2)^2 + (\Delta v_1 \cdot \partial \Delta V R / \partial v_1)^2]^{0.5}$.

The COR's measurement uncertainty was defined in the same way from $\Delta \epsilon = [(\Delta v_2 \cdot \partial \epsilon / \partial v_2)^2 + (\Delta v_1 \cdot \partial \epsilon / \partial v_1)^2 + (\Delta d \cdot \partial \epsilon / \partial d)^2 + (\Delta \omega \cdot \partial \epsilon / \partial \omega)^2]^{0.5}$.

2.2. Positron emission particle tracking

Positron emission particle tracking (PEPT) was used to track the 3D movement and velocity of the ice particles. For this purpose, ice particles made of water solution of ^{18}F were located in the ice decane column with a millisecond temporal resolution. The $[^{18}\text{F}]$ fluoride was produced from $[^{18}\text{O}]$ water targets by the $^{18}\text{O}(p,n)^{18}\text{F}$ nuclear reaction, where a neutron (n) and fluorine-18 were produced by the reaction of an accelerated proton (p) with oxygen-18. Each ice particle was made of 80 μl of the ^{18}F aqueous solution by the method described in Section 2.1. The radioactivity per ice particle was around 20–40 MBq.

A detector array surrounding the decaying nuclei is needed to detect the back-to-back photon pairs. In this study, the “Siemens Biograph Vision 600” PET (positron emission tomography) scanner was utilized as the detector array. The cylindrical scanner consists of 80 rings, and each ring consists of 760 LSO (lutetium oxyorthosilicate) crystals in the tangential direction and one crystal in the axial direction. Each crystal is of the dimension 3.2 mm \times 3.2 mm \times 20 mm. A silicon photomultiplier (SiPM) array couples with a mini block of a 5 \times 5 crystal array. For more details on the scanner, refer to [38]. The crystal arrangement creates an axial field of view (FOV) of 263 mm and a radius of 410 mm. 64-bit list-mode data consisting of information on the detector pairs and 1-ms timestamps were acquired. The lines of response (LORs) identified by the detector pairs were then processed to locate the ice particle.

The distance between the positron emission and the annihilation events gives rise to uncertainty in locating the decaying nucleus. This

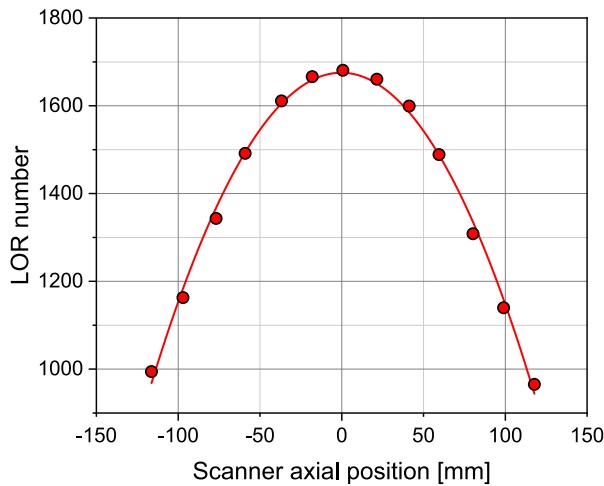


Fig. 3. The number of lines of response (LORs) produced by the ²²Na point source placed at different locations along the scanner axial direction as the x-y coordinate is around (1, -176). Each point represents an average of 60 data.

distance is related to the initial energy of the positron. For ¹⁸F and ²²Na, the mean ranges of positrons in water are around 0.6 mm and 0.53 mm, respectively [29,39]. Also, the non-zero momenta of the positron and electron as they annihilate cause deviation from collinearity, which contributes to further uncertainty in the localization of the decaying nucleus. In addition to the above-mentioned sources of uncertainty, other factors, including finite crystal size, depth of interaction in the crystal, electronics properties, and photon deflection due to interaction with other materials, also create false and deviated signals.

To eliminate the influence of erroneous signals and to accurately identify the centroid of the particle, several data processing algorithms have been developed [30,40,41] and refined for the specific detector system and experimental setup. Unlike the projection-based algorithms that are used in general PET reconstruction, in-house developed PEPT algorithms compare the LORs with each other to identify the most probable location of the centroid of the radioactive ice particle. The iterative operation was applied to eliminate false LORs (of which examples are shown in Fig. 5) and increase the position accuracy.

To verify the positioning algorithm used to process the ice particle data and also to check the variations of LOR amount affected by the relative locations in the FOV, a ²²Na point source (Eckert & Ziegler) of diameter 250 μm was placed at various axial locations. Since in the actual experiments, the ice particle generates 3000–15000 LORs per positioning interval (4 ms in this study), a period was chosen to obtain around 1700 LORs from the ²²Na point source when it was at the FOV center. Then the same data acquisition setting was used as the point source moved to the FOV edge to check how the relative location affects the LOR amount and the positioning accuracy.

As shown in Fig. 3, as the ²²Na point source moved away from the FOV center along the scanner axial direction by around 115 mm, the number of LORs was reduced to 60% of the peak number. The resulting positioning accuracy as a function of axial location is plotted in Fig. 4. 3D standard deviations of 60 positions (Fig. 4) were obtained at different locations corresponding to those shown in Fig. 3. Note that in this verification test, ²²Na point source was off the center in the plane perpendicular to the scanner axial direction for around 176 mm. More minor standard deviations can be expected if the positron emitter is on the axial axis of the cylindrical scanner. Under this condition, the positioning uncertainties, as indicated by the standard deviations, are below 0.2 mm within around half of the axial FOV range.

Verified with the ²²Na point source, the same algorithm was applied to locate the ice particles. Fig. 5(a) shows the LORs of 0.1 ms acquired

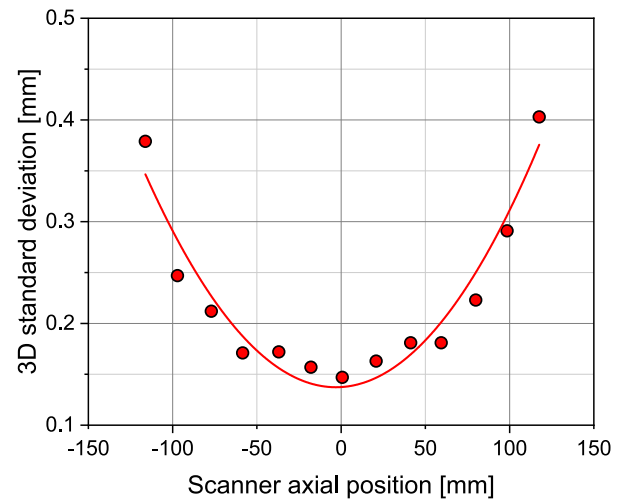


Fig. 4. The 3D standard deviation of 60 positions, as an indication of the positioning accuracy, obtained by processing the LORs of the ²²Na point source using the in-house developed algorithm. The point source was placed at different locations along the scanner axial direction as the x-y coordinate is around (1, -176).

with a stationary ice particle made of 80-μl ¹⁸F aqueous solution and the particle was kept still in decane. Fig. 5(b) shows the LORs used for localization after being processed by the iterative algorithm. The 3D standard deviation of 60 positions, each obtained every 4 ms, is 177 μm under the condition of 3015 LORs per 4 ms and the particle at the z-axis center and off x-y center for around 90 mm. Since the LOR amounts in ice collision experiments are usually between 3000 and 15000, and the standard deviation scales with 1/√n, where n is the number of LORs [40,42], the accuracy in the actual experiments are expected to be better than 177 μm.

The uncertainties of the linear velocities, their ratio, and COR for the PEPT experiments were determined in the same way as for the laboratory tests, using the corresponding uncertainties of the coordinates (Δx = 0.081 mm, Δy = 0.062 mm, Δz = 0.145 mm), and time (Δτ = 2 · 10⁻¹² s).

2.3. Model description

CFD-DEM model of a multiphase system was built using the commercial software STAR-CCM+ 2210 17.06.007 [43]. This model was recently validated for settling of Lagrangian particles in viscous fluids [44]. The fluid and solid phases were solved separately in the coupled CFD-DEM method based on the Eulerian-Lagrangian approach. The liquid phase is described by the system of volume-averaged Navier-Stokes equations formulated for a laminar, incompressible, and isothermal fluid [8]:

$$\frac{D\phi}{Dt} = 0, \tag{2}$$

where φ is the volume fraction of the liquid, and D.../Dt is the substantial derivative. For the computational cells where Lagrangian particles reside, this parameter is calculated as 1 - V_p/V_c, where V_p is the total volume of particles and V_c is the volume of the computational cell.

The momentum equation:

$$\rho \frac{D\phi \vec{u}}{Dt} = -\nabla p + \mu \nabla^2 \vec{u} - \vec{f}_{p,\Sigma}, \tag{3}$$

where \vec{u} is the fluid velocity, ρ, and μ are the density and viscosity, respectively, and p is the pressure. The last term of Eq. (3) describes the superposition of inter-phase forces (per unit volume) acting from Lagrangian particles residing in a computational cell. This term is computed scaling the inter-phase forces applied to an individual particle with the number density of particles in the computational cell n =

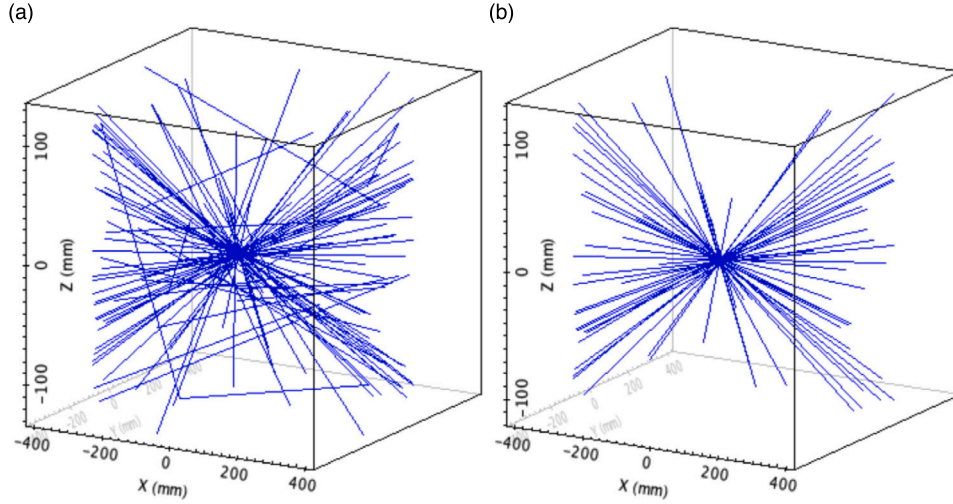


Fig. 5. Lines of response (LORs) of 0.1 ms acquired with a stationary ice particle in decane. The particle was made of 80- μl ^{18}F aqueous solution. The z-axis is the scanner axial axis. (a) Unprocessed LORs. (b) The LORs is used for localization after being processed by the iterative algorithm.

$3\phi/4r_i^3$, where r_i is the radius of the i th particle. We note that Eq. (3) is presented in a general form applicable to a system with multiple particles. However, our system consisted of a single particle.

Newton's second law describes the linear motion of the discrete phase:

$$m_i \frac{d\vec{v}_i}{dt} = \vec{f}_{p,i} + \vec{f}_{ls,i} + \vec{f}_{lr,i} + \vec{f}_{b,i} + \vec{f}_{vm,i} + m_i \vec{g} + \sum_{j=1, N_2} \vec{f}_{i,j}, \quad (4)$$

where m_i is particle mass, \vec{v}_i is the particle's velocity, and indices ls , lr , and vm denote the shear, rotational lift forces, and the virtual mass force, respectively, $\vec{f}_{b,i} = \rho/\rho_p m_i \vec{g}$ is the buoyancy force, and ρ_p is the density of the particle. Also, $\vec{f}_{i,j}$ are the forces acting on the i th particle due to contact with N_2 particles and solid boundaries, and \vec{g} is the acceleration due to gravity. The particle rotation is calculated from:

$$\frac{d}{dt}(I_i \vec{\omega}_{p,i}) = \sum_{j=1, N_2} \vec{T}_{i,j}, \quad (5)$$

where I_i is the particle moment of inertia, $\vec{\omega}_{p,i}$ is the angular velocity of the particle, and $\vec{T}_{i,j}$ is the total torque of the forces acting on the i th particle due to its contacts.

The drag force acting on the particle is calculated as [8]:

$$\vec{f}_{p,i} = \frac{\pi}{2} r_i^2 c_{D,i} \rho_f (\vec{u} - \vec{v}_i) |\vec{u} - \vec{v}_i|, \quad (6)$$

where $c_{D,i}$ is the drag force coefficient. The drag coefficient is calculated according to the Schiller–Naumann drag coefficient method [8]:

$$c_{D,i} = \begin{cases} (24/\text{Re}_{p,i}) \cdot (1 + 0.15 \text{Re}_{p,i}^{0.687}) & \text{Re}_{p,i} \leq 10^3 \\ 0.44 & \text{Re}_{p,i} > 10^3, \end{cases} \quad (7)$$

where $\text{Re}_{p,i} = 2\rho|\vec{u} - \vec{v}_i|r_i/\mu$ is the particle Reynolds number.

The shear lift force (Saffman force) applies to a particle moving relative to a fluid with a velocity gradient in the fluid orthogonal to the relative motion. The force is given as:

$$\vec{f}_{ls,i} = c_{ls} \rho \pi r_i^3 (\vec{u} - \vec{v}_i) \times \vec{\omega}, \quad (8)$$

where $\vec{\omega} = \nabla \times \vec{u}$ is the curl of the fluid velocity and c_{ls} is the lift coefficient. Sommerfeld's definition of the lift coefficient is used in the model [45]:

$$c_{ls,i} = \frac{4.1126}{\text{Re}_{s,i}^{0.5}} f_i(\text{Re}_{p,i}, \text{Re}_{s,i}), \quad (9)$$

where $\text{Re}_{s,i} = 4\rho r_i^2 |\vec{\omega}|/\mu$ is the Reynolds number for shear flow, and function f is given as:

$$f_i = \begin{cases} (1 - 0.3314\beta^{0.5}) e^{-0.1\text{Re}_{p,i}} + 0.3314\beta^{0.5} & \text{Re}_{p,i} \leq 40 \\ 0.0524 (\beta \text{Re}_{p,i})^{0.5} & \text{Re}_{p,i} > 40, \end{cases} \quad (10)$$

$\beta = 0.5 \text{Re}_{s,i}/\text{Re}_{p,i}$. The spin lift force (Magnus force) model is applied to calculate the force acting on a spinning particle moving in a fluid [8]:

$$\vec{f}_{lr,i} = \rho \pi r_i^2 c_{lr} |\vec{u} - \vec{v}_i| \frac{\vec{\Omega}_i \times (\vec{u} - \vec{v}_i)}{|\vec{\Omega}_i|}. \quad (11)$$

In the above, $\vec{\Omega}_i$ is the relative angular velocity of the particle to the fluid:

$$\vec{\Omega}_i = 0.5 \nabla \times \vec{u} - \vec{\omega}_{p,i}, \quad (12)$$

where \vec{u} is the fluid velocity and $\omega_{p,i}$ is the angular velocity of the particle. The coefficient of rotational lift $c_{lr,i}$ is according to Sommerfeld given as [45]:

$$c_{lr,i} = 0.45 + \left(\frac{\text{Re}_{R,i}}{\text{Re}_{p,i}} - 0.45 \right) \exp(-0.5684 \text{Re}_{R,i}^{0.4} \text{Re}_{p,i}^{0.3}), \quad (13)$$

where $\text{Re}_{R,i} = 4\rho r_i^2 |\vec{\Omega}_i|/\mu$.

The virtual mass force affects the material particle as it accelerates the surrounding continuous phase:

$$\vec{f}_{vm,i} = c_{vm} \rho V_{p,i} \left(\frac{D\vec{u}}{Dt} - \frac{d\vec{v}_i}{dt} \right), \quad (14)$$

where $c_{vm} = 0.5$ is the virtual mass coefficient.

When the particle comes into contact with its nearest neighbors at the next DEM-time step, the contact forces and torque are activated in Eq. (4),(5). The Hertz–Mindlin contact model with linear cohesion calculates the contact forces in normal, n , and tangential, t , directions relative to the plane of contact between the objects [35]:

$$\vec{f}_{i,j} = F_{i,j}^{(n)} \vec{n} + F_{i,j}^{(t)} \vec{t}. \quad (15)$$

The unit vector normal to the contact plane \vec{n} points from the center of colliding i th particle towards the center of the j th particle or the contact zone at the wall.

The normal component of the force then becomes:

$$F_{i,j}^{(n)} = -K^{(n)} \delta^{(n)} - N^{(n)} v_i^{(n)} + F_C, \quad (16)$$

where $\delta^{(n)}$ is the particle-to-wall overlap distance. According to Hertz's theory, $K^{(n)}$ is the "spring's" stiffness in the normal direction employed

in the soft-sphere approach, and it is dependent on $\delta^{(n)}$:

$$K^{(n)} = \frac{4}{3} E_e \sqrt{r_i \delta^{(n)}}, \quad (17)$$

where $E_e = E_i / (1 - \nu_i^2)$ is the equivalent of Young's modulus, E_i is Young's modulus, and ν_i is the Poisson ratio. $N^{(n)}$ is the damping coefficient in the normal direction:

$$N^{(n)} = \sqrt{5K^{(n)} m_i} \frac{-\ln(\epsilon_{(n)})}{\sqrt{\pi^2 + (\ln \epsilon_{(n)})^2}}, \quad (18)$$

where $\epsilon_{(n)}$ is the coefficient of the particle material restitution in the normal direction. The cohesive force is expressed using Johnson-Kendall-Roberts (JKR) model [46]:

$$F_C = 1.5r_i W \pi, \quad (19)$$

where W is the work of cohesion. The values for the cohesion work at different experimental temperatures were taken from the work of Yang et al. [6].

The tangential component of the contact force [35]:

$$F_{i,j}^{(t)} = -K^{(t)} \delta^{(t)} - N^{(t)} v_i^{(t)} \quad (20)$$

where

$$\delta^{(t)} = \int_0^{t_c} v_i^{(t)} dt, \quad (21)$$

where t_c is the contact duration [47]:

$$t_c = 2.94 \left(\frac{5\sqrt{2}\pi\rho_p}{4E_e} \right)^{0.4} r_i v_i^{-1/5}. \quad (22)$$

The stiffness coefficient in the tangential direction:

$$K^{(t)} = 8G_e \sqrt{r_i \delta^{(t)}}, \quad (23)$$

where $G_e = 0.5 \frac{E_i}{(1+\nu_i)}$ is the equivalent shear modulus.

$N^{(t)}$ is the damping coefficient in the tangential direction:

$$N^{(t)} = \sqrt{5K^{(t)} m_i} \frac{-\ln(\epsilon_{(t)})}{\sqrt{\pi^2 + (\ln \epsilon_{(t)})^2}}, \quad (24)$$

where $\epsilon_{(t)}$ is the particle restitution coefficient in the tangential direction.

In case $|K^{(t)} \delta^{(t)}| > f_s |K^{(n)} \delta^{(n)}|$ the tangential component comes above the sliding limit, a constant $F^{(t)}$ applies as follows [35]:

$$F^{(t)} = f_s |K^{(n)} \delta^{(n)}| \text{sign}(\delta^{(t)}), \quad (25)$$

where f_s is the Coulomb friction coefficient.

The last aspect of the model is the rolling resistance that gives a resisting torque in Eq. (5):

$$\vec{M}_{i,j} = r_i \mu_r F_{i,j}^{(n)} \frac{-\vec{\omega}_i}{|\vec{\omega}_i|}, \quad (26)$$

where $\mu_r = 2.5 \cdot 10^{-2}$ is the coefficient of rolling resistance.

To account for the lubrication forces in the continuous phase, we used the approach developed by Joseph et al. [48], extrapolating the COR for wet particles from the COR in "dry" conditions:

$$\epsilon_{(n)} = \epsilon_{dry} + \frac{1 + \epsilon_{dry}}{St_0} \ln \frac{x_c}{x_0}, \quad (27)$$

where $\epsilon_{dry} = 0.8$ is the dry restitution coefficient, $St_0 = m_i v_i / 6\pi\mu r_i^2$ is the particle Stokes number before the contact takes place, and $x_c/x_0 \sim 10^{-3}$ is the typical ratio between the inter-particle distance at the point of contact x_c and the terminal position outside the range of the lubrication force x_0 [48]. As in Reitter et al. [17], we set $\epsilon_{dry} = 0.8$, and also assume the coefficient of restitution in the tangential direction was not significantly altered by lubrication, i.e., $\epsilon_{(t)} = \epsilon_{dry}$. The values of the static friction coefficient for ice were taken from recent experiments by

Sukhorukov [49]. They were also linearly interpolated for the temperature interval from our experiments — the obtained values of the static friction coefficient range from 0.57 to 0.71. The physical properties of the ice and the decane were set dependent on the temperature following NIST database [50].

The numerical model was built in the commercial CFD-package STAR-CCM+. The geometry of the computational domain is the same as experimental geometry. The boundary conditions include the pressure boundary at the decane-air interface, and the rest of the surfaces are no-slip walls. As presented in Fig. 6, the computational domain was discretized using 143656 27-mm³ cubical control volumes to simulate the process of the ice drop falling and the collision with the inclined ice surface. The mesh around the inclined surface is refined to 20% of the mesh base size. A mesh-independence study was performed using mesh sizes twice smaller and 1.5 times larger than the used mesh size. The chosen mesh size resulted in the lowest computational costs, yet the best quantitative agreement with values of particle terminal velocity computed using analytical expressions [8]. A two-grid procedure is used to couple the phases in the vicinity of the boundaries, where the computational cells are smaller than the particle. In this case, the fluid phase was resolved on a larger grid, and then the velocity and the pressure fields were linearly interpolated to the original mesh [51]. In the experiments, the shape of the particles was not ideally spherical. Therefore, composite particles were generated as an assembly of two spheres with the sizes and the offset determined experimentally. They are presented in Fig. 6.

The continuous-phase equations were spatially discretized using central differences. The Euler implicit method was used to advance time with a time step of 10 ms. The governing equations were solved numerically using SIMPLE(Semi Implicit Pressure Linked Equation) with relaxation coefficients: 0.8 velocity, 0.2 pressure, 0.9 volume fraction. A study compared different collision models, including the Hertz-Mindlin and Walton-Brown models [52]. The results showed that both models produced similar outcomes. The minimum time step for the DEM solver was set at 20% of the duration of the Rayleigh wave propagation through the particle [53].

3. Results and discussion

3.1. Experimental trajectories

An example of the particle fall process is shown in Fig. 7 and in the Supplementary video. From the experiments, we conclude that the particle moved vertically enough for most of the drops. Deviations from the vertical trajectory are insignificant, and the moment of collision is well detected. The reason for the horizontal shifts during the falling process is that the particle does not have an ideal spherical shape. Due to the small magnitude, this was challenging to quantify the rotational motion during the particle fall.

A clear rebound does not characterize the collision itself. The particle continues to move along the inclined ice surface without a detachment but starts rolling after the impact. A similar movement of the particle was detected in the PEPT experiments. Fig. 8 shows a typical PEPT-track of the ice particle with a 4 ms time resolution.

The trajectory shows that the particle descended, collided with the inclined ice surface, continued moving along the ice surface, and eventually proceeded further down through a vertical column (Fig. 1A). The particle speed, as shown in Fig. 8(b), downward velocity, and acceleration can be further calculated. As it can be seen in Fig. 8(b), the particle speed decreased abruptly once colliding with the ice surface.

As discussed before, if the particle is not perfectly round, it can be subject to unbalanced lateral forces while settling in decane. This results in lateral movements as can be seen in the figures. It is observed that the particle experienced a speed drop and a speed recovery around the collision event, which is likely an indication of a rebound. In the PEPT experiments, the rebound velocity was identified at the time when the descending speed reached a local minimum (minimal downward motion). Also, the velocity before the collision was identified just before this local minimum descending.

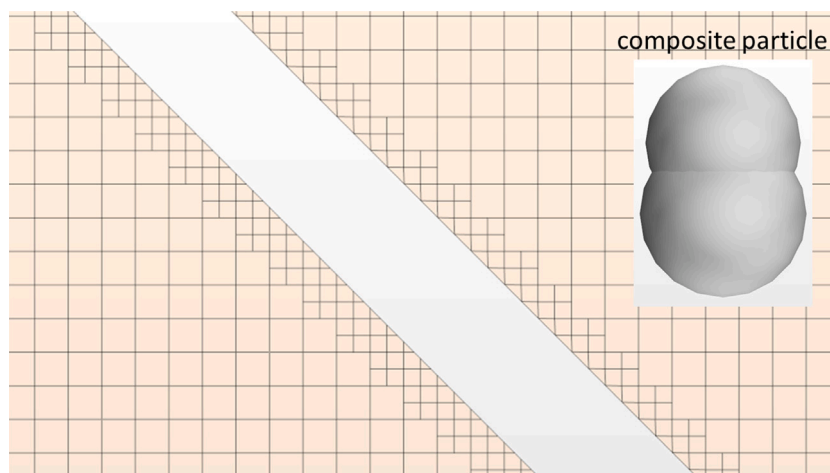


Fig. 6. Computational grid at the inclined surface and particle geometry.

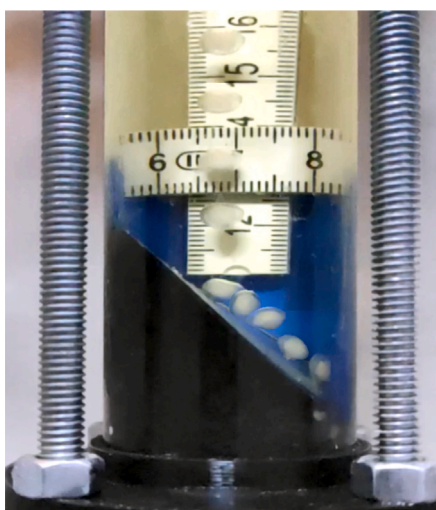


Fig. 7. Particle trajectory during experiments obtained combining video snapshots.

3.2. CFD-DEM

The numerical analysis was carried out for a temperature interval from $-15\text{ }^{\circ}\text{C}$ to $-1.4\text{ }^{\circ}\text{C}$. For illustration, Fig. 9 shows the particle velocity as a function of time at $-4.5\text{ }^{\circ}\text{C}$. As can be seen from the figure, the first time interval (1) corresponds to the initial particle's downward motion when the velocity of the particle accelerates with a simultaneous increase in the drag force. After the interval (1), the terminal velocity was reached. According to the simulation, the average value of this velocity was 12 cm/s . The time interval when the particle moves with this constant speed is denoted as (2) in the figure. At the next stage (3), when the ice particle collides with the inclined ice surface, the velocity drops to about 7 cm/s due to mechanical deformation (including lubrication) and cohesion. After collision (4), the particle accelerates again due to gravity up to a value close to the terminal velocity. At the last stage (5), the velocity drops sharply as the particle reaches the bottom of the column and rebounds slightly, changing the velocity magnitude. Fig. 9 also illustrates how the temporal change of the total contact forces during motion along the ice surface. As follows from the figure, the contact forces are negative at the first collision of the particle with the wall due to the deformation of the materials. The overlap reduces from an initial value of $16\text{ }\mu\text{m}$ to $\sim 7\text{ }\mu\text{m}$ during the next rounds of particle deformation. The magnitude of the forces is about 3 times higher than the cohesive force, which is $\sim 1\text{ mN}$ in this

case. The positive peaks appear at the moments of system reloading after the first repulsion when the particle is directed back towards the surface under the simultaneous action of gravity and cohesion. Fig. 10 demonstrates an imprint of the particle's trajectory onto the velocity field in the liquid. According to the figure, the particle's trajectory is not strictly vertical, which was also observed in the experiments. Due to the non-spherical shape, the particle scours, and then lift forces come into action. As expected, the velocity of the liquid phase reaches a maximum around the moving particle. The average velocity values are observed along the trajectory of the particle, and the lowest values correspond to the remaining regions. The velocity in the area below an inclined plane is almost zero before an ice particle collides with it, but it increases slightly after the particle-wall collision.

3.3. COR and model validation

The video experiments were carried out in the temperature range from $-15\text{ }^{\circ}\text{C}$ to $-0.3\text{ }^{\circ}\text{C}$, while the temperature for the PEPT experiments varied in the range from $-15.7\text{ }^{\circ}\text{C}$ to $-4.2\text{ }^{\circ}\text{C}$. The summary of these studies and their comparison with CFD simulation are discussed below. We note that the repeatability of experimental results for temperatures above $-2\text{ }^{\circ}\text{C}$ was complex due to difficulties in thermal stabilization. This was the primary source of scattering of the experimental data. However, as it will be shown below, the reliability of the obtained data is confirmed by their agreement in the measurements done by different methods.

Fig. 11 presents the linear velocities of the particles before and after the collision with the ice surface. We conclude that the velocities obtained by the different methods are in good agreement with each other. Taking the results from the video experiments as a reference, the average/maximum deviations of the PEPT experiments and the simulation results are $6.6/28.8\%$ and $8.8/12.9\%$ for the velocities before the collision. They are $23.8/46.4\%$ and $12.8/16.7\%$ for the velocities after the collision, respectively.

The effect of the temperature on the particle velocities before and after the collision is different. Considering the results of simulation and laboratory tests first, we observe the particle velocity *before* the collision slightly increases with the temperature. In contrast, the particle velocity *after* the collision tends to have a maximum value at a temperature of $-9.9\text{ }^{\circ}\text{C}$ (video) and $-12\text{ }^{\circ}\text{C}$ (CFD).

The velocity *before* the collision increases with the temperature as the viscosity of decane reduces [50]. At the same time, the particle velocity *after* impact increases too, but only up to a specific temperature. This is probably due to the reduction of the ice friction coefficient with temperature followed by an increased cohesion of ice [6,7] coming

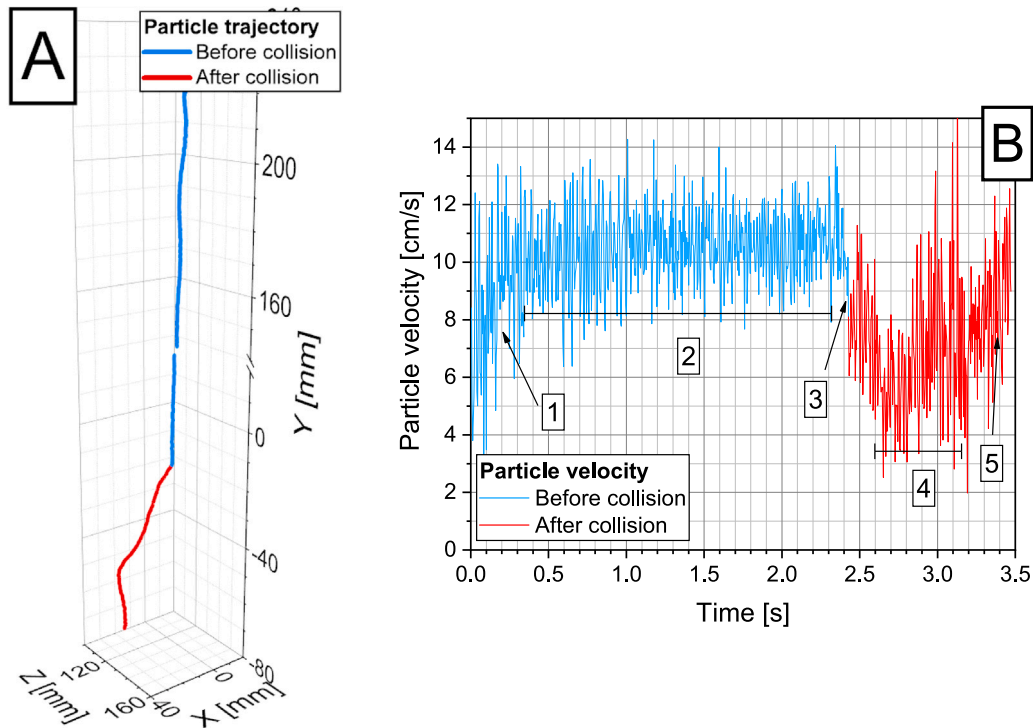


Fig. 8. Particle track in decane obtained by PEPT with a temporal resolution of 4 ms (A), and particle velocity history (B). The particle is released (1) and sedimented in decane (2), collided with the inclined ice surface (3), continued moving along the ice surface (4), and eventually fell further down through a vertical tunnel (5).

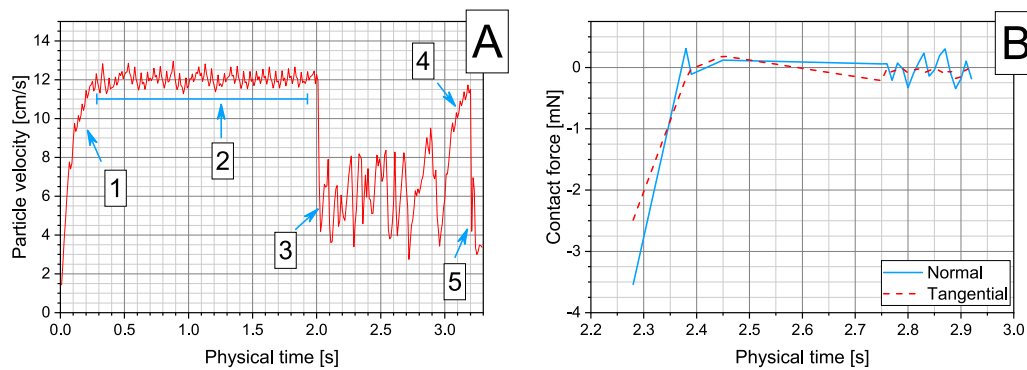


Fig. 9. Temporal changes in particle velocity (A) and contact forces (B) at $-4.5\text{ }^{\circ}\text{C}$ obtained using a CFD-DEM model, depicting the particle's movement as it was released (1), settled in decane (2), collided with the inclined ice surface (3), slid along the ice surface (4), and ultimately dropped down a vertical tunnel (5).

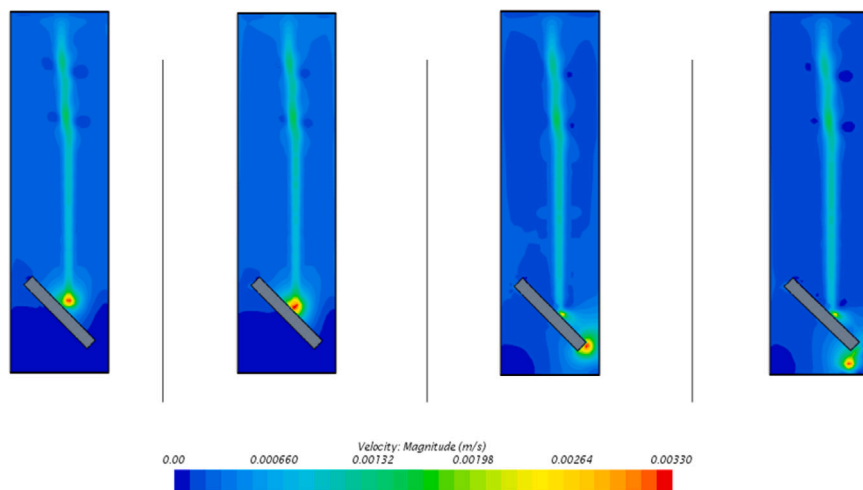


Fig. 10. Velocity distribution of the fluid phase at four different moments of the time at $-4.5\text{ }^{\circ}\text{C}$.

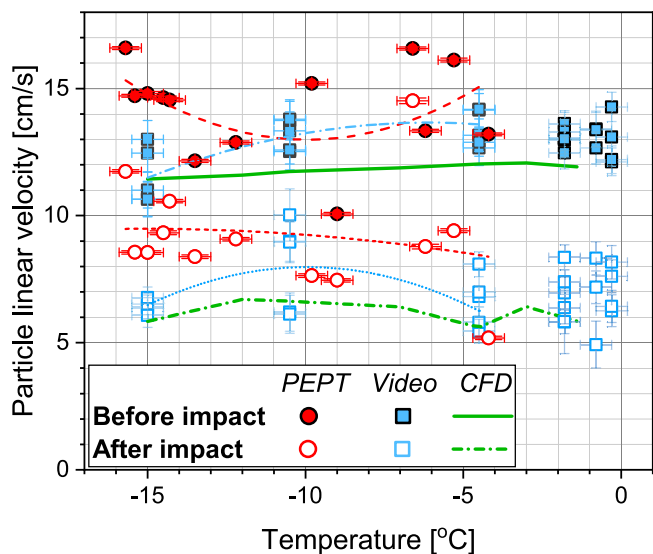


Fig. 11. Particle linear velocities as a function of temperature. Polynomial approximations of experimental results are given for reference.

into action and dominating all other effects, continuously reducing the velocity when increasing the temperature.

A slightly different behavior of particle velocities was found in PEPT experiments. Here the velocity *before* the collision has a *minimum* value at around $-9.9\text{ }^{\circ}\text{C}$, while the velocity *after* the collision constantly decreases within the entire studied temperature range. We attribute these results to a broader spread of particle velocity caused by the lower accuracy of the PEPT experiments because of the more complicated experimental procedure. We also note that the thermal stabilization was imperfect in the PEPT experiments as the portal of the scanner is subjected to automatic ventilation. Therefore, thermal convection of the decane was possible there.

Despite that, the linear velocity ratio ($VR = v_2/v_1$) for all of the methods is similar (Fig. 12). Taking the fitted values of VR from the video experiments as a reference, the average deviation of the CFD and PEPT is 4.2%, and 16.9%, respectively, and the maximum deviations are 8.1% and 18.1%, respectively. All the methods show the VR has a local maximum which is 0.711 at $-10.8\text{ }^{\circ}\text{C}$ (PEPT), 0.605 at $-11.1\text{ }^{\circ}\text{C}$ (video), and 0.578 at $-12\text{ }^{\circ}\text{C}$ (CFD). The appearance of the VR maximum is a consequence of linear velocity behavior. Ice cohesion, friction, and viscosity are the primary factors affecting the maximum linear velocity ratio. These factors affect particle motion differently and contribute to the overall system behavior. Due to increasing ice cohesion in decane when the temperature increases [6,7], the particle impact becomes less elastic. In contrast, decreasing ice friction and viscosity of decane with increasing temperature causes the drag and shear forces acting on the particle to decrease, leading to a permanent increase in particle velocity before impact. The observed maximum VR results from a balance between the increased ice cohesion and decreased friction, which simultaneously progress with the increased temperature. Below the extremum, the friction is reduced with temperature while the cohesion is still low. Therefore, VR increases. Increasing the temperature above the extremum makes the cohesion effect more dominant, decreasing the linear velocity ratio.

The influence of ice cohesion forces is also seen from the angular velocities of the particle after the impact (Fig. 13). Here, the laboratory experiments showed the angular velocity has a maximum at the temperature of $-9.6\text{ }^{\circ}\text{C}$. Then, the angular velocity reduces with the increase in temperature. The simulation showed a slightly higher temperature for the maximum angular velocity point, around $-4.5\text{ }^{\circ}\text{C}$. Nevertheless, in general, the data are in good agreement with each other.

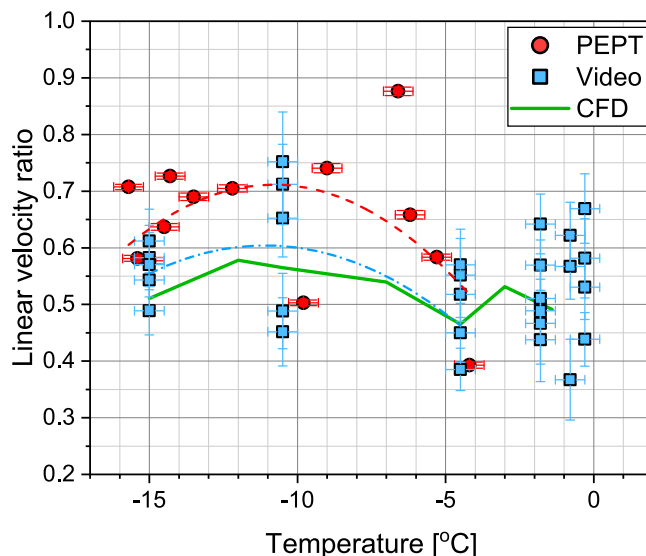


Fig. 12. Velocity ratio as a function of temperature. Polynomial approximations of experimental results are given for reference.

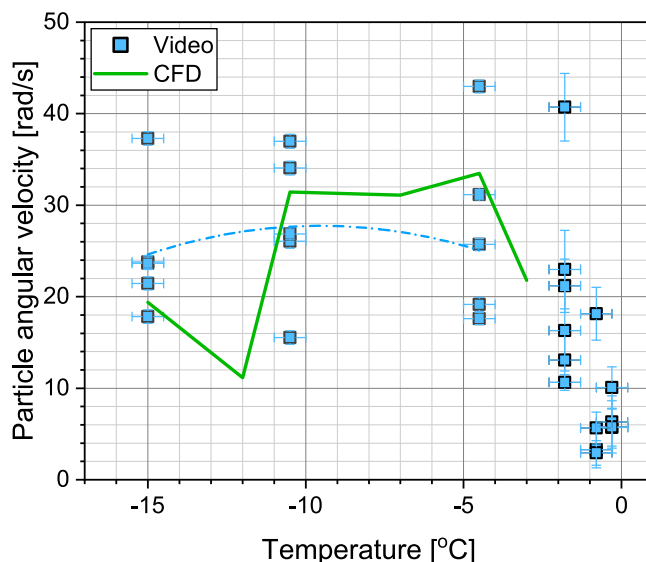


Fig. 13. Angular particle velocity as a function of temperature. Polynomial approximations of experimental results are given for reference.

The average and maximum deviation of simulation from the video experiments are 28.5% and 58.8%. This significant spread is, however, expected since the shape of the particles is a non-ideal sphere. Due to that, the variations of angular velocities appear if a particle touches the ice plane with a more or less flat section of its surface. We note that no information on the particle's angular velocity is available from our PEPT method.

The coefficient of restitution of ice in decane was determined using linear and angular velocities as a square root of the ratio of particle kinetic energies before and after an impact, according to Eq. (1). Fig. 14 presents these calculations. It should be noted that since the particle rotation could not be quantified in the PEPT experiments, we took the fitted values of particle angular velocity from the video experiments. To illustrate how cohesion influences the COR, in this figure, we show the CFD results from two different simulation series: one produced using the median cohesive force from Yang et al. [6] and those with 95%-based values. From Fig. 14, we conclude that there is a good agreement

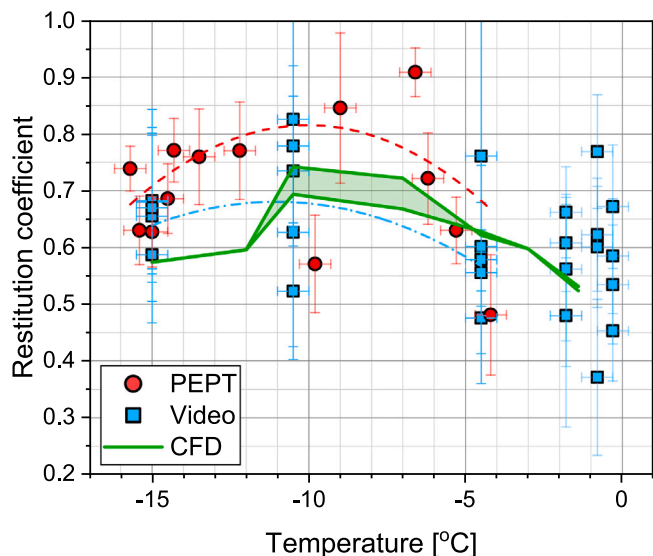


Fig. 14. Coefficient of restitution of ice in decane. Polynomial approximations of experimental results are given for reference.

between the video experiments and CFD simulation. The average and maximum deviation of simulation from lab tests are 9.4% and 12.1%. Deviation of the PEPT experiments is higher and equals to an average of 19.0% and a maximum of 21.7%. For all three methods, a temperature of maximum COR can be found at -11.0 °C (video), -10.5 °C (CFD), and -10.0 °C (PEPT). These temperatures agree with each other, corresponding to the maximal values of COR 0.680 (video), 0.742/0.693 (CFD, median cohesive force/95%-based values), and 0.816 (PEPT). The temperature trend of COR is similar for all three methods. With increasing temperature, the COR first increases until the temperature of maximum COR. Then, the COR decreases, reaching a similar or slightly lower value at -4.2 °C than at the lowest considered temperatures. The minimum obtained values of the COR are 0.567 (video), 0.574 (CFD), and 0.682 (PEPT).

4. Conclusions

This paper provides new data on the restitution coefficient of ice in decane in the temperature range from -15.7 °C to -0.3 °C. The restitution coefficient was proportional to the ratio of kinetic energies of a falling particle in decane before and after its collision with an inclined ice surface. Particle velocity measurements were carried out using the Positron-Emission Particle Tracking technique (PEPT) and high-speed video recording. Both methods provided similar data on the linear velocities, their ratios, and the restitution coefficient (COR). However, the COR has average and maximum deviations between PEPT experiments and the camera-recorded experiments of 19.0% and 21.7%. The reasons for that are thought to be the more complicated procedure of the PEPT experiments compared to the laboratory tests and the impossibility of determining the angular velocity of a particle after its collision with the ice surface.

The coefficient of restitution has a maximum value at -10.0 / -11.0 °C (PEPT/video). This value is 0.816/0.680, while the minimum values within the temperature range of -15.7 ... -4.2 °C are 0.682/0.567 (PEPT/video). The increasing restitution coefficient is due to the decreasing viscosity of the decane, and the decreasing values are due to cohesion.

The experiments were reproduced using CFD-DEM, considering the cohesion, temperature-dependent properties of the materials, and shape of the particles. The restitution coefficient obtained in the simulations deviates from the video-recorded experiments with an average discrepancy of 9.4%. The simulation reproduced the actual particle tracks well,

giving particle velocities very close to the actual ones. The average deviations of the simulated particle linear and angular velocities from the experimental values were about 10.8%. Based on the successful validation of the model with experimental results, we conclude that the cohesive CFD-DEM model implemented in Star-CCM+ is sufficiently accurate.

CRedit authorship contribution statement

Nazerke Saparbayeva: Investigation, Writing – review & editing. **Yu-Fen Chang:** Investigation, Writing – review & editing. **Pawel Kosinski:** Supervision. **Alex C. Hoffmann:** Supervision. **Boris V. Balakin:** Supervision, Investigation, Writing – review & editing. **Pavel G. Struchalin:** Investigation, Writing – review & editing.

Declaration of competing interest

The authors declare the following financial interests/personal relationships which may be considered as potential competing interests: Boris Balakin reports financial support was provided by Research Council of Norway.

Data availability

Data will be made available on request.

Acknowledgments

This project was supported by the Research Council of Norway (project 300286). We thank Dr Tom Christian Holm Adamsen and radiographer Bodil Naess from Haukeland University Hospital for their help in the production of radioactive solution and running the PET scanner.

Appendix A. Supplementary data

Supplementary material related to this article can be found online at <https://doi.org/10.1016/j.powtec.2023.118660>.

References

- [1] M. Kauffeld, S. Gund, Ice slurry–History, current technologies and future developments, *Int. J. Refrig.* 99 (2019) 264–271.
- [2] L. Liu, Z. Fang, M. Wang, C. Qi, Y. Zhao, C. Huan, Experimental and numerical study on rheological properties of ice-containing cement paste backfill slurry, *Powder Technol.* 370 (2020) 206–214.
- [3] M. Kauffeld, M. Kawaji, P.W. Egolf, Handbook on Ice Slurries, Vol. 359, International Institute of Refrigeration, Paris, 2005.
- [4] K. Matsumoto, M. Okada, T. Kawagoe, C. Kang, Ice storage system with water–oil mixture: formation of suspension with high IPF, *Int. J. Refrig.* 23 (5) (2000) 336–344.
- [5] P.J. Rensing, M.W. Liberatore, A.K. Sum, C.A. Koh, E.D. Sloan, Viscosity and yield stresses of ice slurries formed in water-in-oil emulsions, *J. Non-Newton. Fluid Mech.* 166 (14–15) (2011) 859–866.
- [6] S.-o. Yang, D.M. Kleehammer, Z. Huo, E. Sloan, K.T. Miller, Temperature dependence of particle–particle adherence forces in ice and clathrate hydrates, *J. Colloid Interface Sci.* 277 (2) (2004) 335–341, <http://dx.doi.org/10.1016/j.jcis.2004.04.049>.
- [7] P.G. Struchalin, V.H. Øye, P. Kosinski, A.C. Hoffmann, B.V. Balakin, Flow loop study of a cold and cohesive slurry, pressure drop and formation of plugs, *Fuel* 332 (2023) 126061.
- [8] C. Crowe, M. Sommerfeld, Y. Tsuji, *Multiphase Flow with Droplets and Particles*, CRC Press, 1998.
- [9] A. Hooshanginejad, A. Baskota, S. Jung, Backflipping motion of air bubbles colliding with a tilted wall, 2022, arXiv preprint [arXiv:2208.14486](https://arxiv.org/abs/2208.14486).
- [10] O.I. Vinogradova, G.E. Yakubov, Surface roughness and hydrodynamic boundary conditions, *Phys. Rev. E* 73 (4) (2006) 045302.
- [11] T. Oesau, P. Grohn, S. Pietsch-Braune, S. Antonyuk, S. Heinrich, Novel approach for measurement of restitution coefficient by magnetic particle tracking, *Adv. Powder Technol.* 33 (1) (2022) 103362.

- [12] B.V. Balakin, S. Alyaev, A.C. Hoffmann, P. Kosinski, Micromechanics of agglomeration forced by the capillary bridge: The restitution of momentum, *AIChE J.* 59 (11) (2013) 4045–4057.
- [13] T. Eidevåg, E.S. Thomson, S. Sollén, J. Casselgren, A. Rasmuson, Collisional damping of spherical ice particles, *Powder Technol.* 383 (2021) 318–327.
- [14] F.G. Bridges, A. Hatzes, D. Lin, Structure, stability and evolution of Saturn's rings, *Nature* 309 (5966) (1984) 333–335.
- [15] M. Higa, M. Arakawa, N. Maeno, Measurements of restitution coefficients of ice at low temperatures, *Planet. Space Sci.* 44 (9) (1996) 917–925.
- [16] T. Hauk, E. Bonaccorso, I. Roisman, C. Tropea, Ice crystal impact onto a dry solid wall. Particle fragmentation, *Proc. R. Soc. A* 471 (2181) (2015) 20150399.
- [17] L.M. Reitter, A. Mayrhofer, C. Tropea, J. Hussong, Experimental investigation of normal and oblique impact of ice particles onto a wetted wall, in: *AIAA AVIATION 2022 Forum*, 2022, p. 3533.
- [18] S. Antonyuk, S. Heinrich, J. Tomas, N.G. Deen, M.S. Van Buijtenen, J. Kuipers, Energy absorption during compression and impact of dry elastic-plastic spherical granules, *Granul. Matter* 12 (1) (2010) 15–47.
- [19] S. Antonyuk, S. Heinrich, N. Deen, H. Kuipers, Influence of liquid layers on energy absorption during particle impact, *Particuology* 7 (4) (2009) 245–259.
- [20] T. Müller, K. Huang, Influence of the liquid film thickness on the coefficient of restitution for wet particles, *Phys. Rev. E* 93 (4) (2016) 042904.
- [21] P. Gondret, M. Lance, L. Petit, Bouncing motion of spherical particles in fluids, *Phys. Fluids* 14 (2) (2002) 643–652.
- [22] D. Hastie, Experimental measurement of the coefficient of restitution of irregular shaped particles impacting on horizontal surfaces, *Chem. Eng. Sci.* 101 (2013) 828–836.
- [23] F. Krull, R. Hesse, P. Breuninger, S. Antonyuk, Impact behaviour of microparticles with microstructured surfaces: Experimental study and DEM simulation, *Chem. Eng. Res. Des.* 135 (2018) 175–184.
- [24] F. Krull, J. Mathy, P. Breuninger, S. Antonyuk, Influence of the surface roughness on the collision behavior of fine particles in ambient fluids, *Powder Technol.* 392 (2021) 58–68.
- [25] Y. Fangary, M. Barigou, J. Seville, D. Parker, Fluid trajectories in a stirred vessel of non-newtonian liquid using positron emission particle tracking, *Chem. Eng. Sci.* 55 (24) (2000) 5969–5979.
- [26] F. Snieders, A. Hoffmann, D. Cheesman, J. Yates, M. Stein, J. Seville, The dynamics of large particles in a four-compartment interconnected fluidized bed, *Powder Technol.* 101 (3) (1999) 229–239.
- [27] B. Hoomans, J. Kuipers, M.M. Salleh, M. Stein, J. Seville, Experimental validation of granular dynamics simulations of gas-fluidised beds with homogenous in-flow conditions using positron emission particle tracking, *Powder Technol.* 116 (2–3) (2001) 166–177.
- [28] D. Parker, A. Dijkstra, T. Martin, J. Seville, Positron emission particle tracking studies of spherical particle motion in rotating drums, *Chem. Eng. Sci.* 52 (13) (1997) 2011–2022.
- [29] D.L. Bailey, D.W. Townsend, P.E. Valk, M.N. Maisey, *Positron Emission Tomography: Basic Sciences*, Springer London, 2006.
- [30] Y.F. Chang, T.C.H. Adamsen, A.C. Hoffmann, Using a PET camera to track individual phases in process equipment with high temporal and spatial resolutions: Algorithm development, in: *2012 IEEE International Instrumentation and Measurement Technology Conference Proceedings*, 2012, pp. 2326–2330, <http://dx.doi.org/10.1109/I2MTC.2012.6229306>.
- [31] K. Cole, K. Waters, X. Fan, S. Neethling, J. Gilliers, Combining Positron Emission Particle Tracking and image analysis to interpret particle motion in froths, *Miner. Eng.* 23 (11–13) (2010) 1036–1044.
- [32] M.S. Van Buijtenen, W.-J. Van Dijk, N.G. Deen, J. Kuipers, T. Leadbeater, D. Parker, Numerical and experimental study on multiple-spout fluidized beds, *Chem. Eng. Sci.* 66 (11) (2011) 2368–2376.
- [33] Y.-F. Chang, B.V. Balakin, Novel bio-compatible tracers for positron emission particle tracking, in: *J. Phys.: Conf. Ser.*, 1689, (1) IOP Publishing, 2020, 012019.
- [34] L. Chen, Y. Wang, J.J. Klemeš, J. Wang, W. Tao, Study on collision between single coarse particle and wall in viscous media using CFD–DEM, *Eur. J. Mech. B Fluids* (2022).
- [35] A.S. Hellestø, M. Ghaffari, B.V. Balakin, A.C. Hoffmann, A parametric study of cohesive particle agglomeration in a shear flow—Numerical simulations by the discrete element method, *J. Dispers. Sci. Technol.* 38 (5) (2017) 611–620.
- [36] X. Duan, B. Shi, J. Wang, S. Song, H. Liu, X. Li, Y. Chen, Q. Liao, J. Gong, S. Chen, et al., Simulation of the hydrate blockage process in a water-dominated system via the CFD-dem method, *J. Nat. Gas Sci. Eng.* 96 (2021) 104241.
- [37] Y. Li, J. Zhao, B. Shi, J. Gong, Q. Li, et al., Simulation of the effect of hydrate adhesion properties on flow safety in solid fluidization exploitation, *Petroleum* (2022).
- [38] J. Van Sluis, J. De Jong, J. Schaar, W. Noordzij, P. Van Snick, R. Dierckx, R. Borra, A. Willemsen, R. Boellaard, Performance characteristics of the digital biograph vision PET/CT system, *J. Nucl. Med.* 60 (7) (2019) 1031–1036.
- [39] L. Jødal, C. Le Loirec, C. Champion, Positron range in PET imaging: non-conventional isotopes, *Phys. Med. Biol.* 59 (23) (2014) 7419–7434.
- [40] Y.-F. Chang, C. Ilea, Ø. Aasen, A. Hoffmann, Particle flow in a hydrocyclone investigated by positron emission particle tracking, *Chem. Eng. Sci.* 66 (18) (2011) 4203–4211.
- [41] Y.-F. Chang, A.C. Hoffmann, A Lagrangian study of liquid flow in a reverse-flow hydrocyclone using positron emission particle tracking, *Exp. Fluids* 56 (1) (2015) 4, <http://dx.doi.org/10.1007/s00348-014-1875-5>.
- [42] C. Wiggins, R. Santos, A. Ruggles, A feature point identification method for positron emission particle tracking with multiple tracers, *Nucl. Instrum. Methods Phys. Res. A* 843 (2017) 22–28.
- [43] P. Siemens, *STAR-CCM+ User Guide Version 2210*, Siemens PLM Software Inc., Munich, Germany, 2022.
- [44] J.J. Casarin, A.T. Franco, E.M. Germer, R.G. Pivovarski, Numerical simulation of the particle settling in a Bingham fluid using the two-way coupling CFD-DEM scheme, *J. Theoret. Appl. Mech.* 60 (2022).
- [45] M. Sommerfeld, et al., Theoretical and Experimental Modelling of Particulate Flows, in: *Lecture Series*, vol. 6 (2000) 3–7.
- [46] K.L. Johnson, K.L. Johnson, *Contact Mechanics*, Cambridge University Press, 1987.
- [47] S. Timoshenko, J.N. Goodier, *Theory of Elasticity: By S. Timoshenko and JN Goodier*, McGraw-Hill, 1951.
- [48] G. Joseph, R. Zenit, M. Hunt, A. Rosenwinkel, Particle–wall collisions in a viscous fluid, *J. Fluid Mech.* 433 (2001) 329–346.
- [49] S. Sukhorukov, *Ice-Ice and Ice-Steel Friction in Field and in Laboratory*, Norges teknisk-naturvitenskapelige universitet, Fakultet for . . . , 2013.
- [50] Thermophysical properties of decane. NIST chemistry webbook, 2022, <https://webbook.nist.gov/cgi/fluid.cgi?ID=C124185&Action=Page>. (Accessed 24 November 2022).
- [51] Siemens Digital Industries Software, *Simcenter STAR-CCM+ user guide v. 2020.1*, 2020, Siemens.
- [52] O.R. Walton, Numerical simulation of inclined chute flows of monodisperse, inelastic, frictional spheres, *Mech. Mater.* 16 (1–2) (1993) 239–247.
- [53] P.C. Vinh, R. Ogden, On formulas for the Rayleigh wave speed, *Wave Motion* 39 (3) (2004) 191–197.

CFD-DEM MODEL OF PLUGGING IN FLOW WITH COHESIVE PARTICLES

Nazerke Saparbayeva and Boris V. Balakin

Scientific Reports, Nature. **13**, 17188 (2023)



OPEN

CFD-DEM model of plugging in flow with cohesive particles


Nazerke Saparbayeva  & Boris V. Balakin

Plugging in flows with cohesive particles is crucial in many industrial and real-life applications such as hemodynamics, water distribution, and petroleum flow assurance. Although probabilistic models for plugging risk estimation are presented in the literature, multiple details of the process remain unclear. In this paper, we present a CFD-DEM model of plugging validated against several experimental benchmarks. Using the simulations, we consider the process of plugging in a slurry of ice in decane, focusing on inter-particle collisions and plugging dynamics. We conduct a parametric study altering the Reynolds number (3000...9000), particle concentration (1.6...7.3%), and surface energy (21...541 mJ/m²). We note the process possesses complex non-linear behaviour for the cases where particle-wall adhesion reduces by more than 20% relative to inter-particle cohesion. Finally, we demonstrate how the simulation results match the flow maps based on the third-party experiments.

Cohesive particles can significantly impact the morphology of multiphase flows. Sticking to each other and walls, the particles build an obstruction or plug in closed channels. The plugging is crucial in many applied fluid mechanics problems: flows in porous media, hemodynamics, and suspension rheology¹. The industrial relevance of the problems concerns petroleum, pharmaceutical, chemical, and food industries. More globally, the process of plugging is relevant for behaviour models of animals¹. The plugging is dependent on the flow field, the number of particles, their cohesivity, and contact behaviour. However, due to the complexity of inter-particle and particle-fluid interactions, no reliable methodology is used to predict the plug formation process. Experimental flow maps enable evaluation of plugging risks for a limited interval of flow conditions². Therefore, a better theoretical understanding of the fluid mechanics of plugging is required to extend and update the existing empirical correlations.

For this reason, numerical models of plugging based on the principles of computational fluid dynamics (CFD) are developed. About a decade ago, simplified models of plugging were developed for petroleum^{3,4} and medical applications⁵. Eskin et al.³ considered the process of asphaltene deposition in petroleum pipes using the advection-diffusion method coupled with the population balance approach, which simulated the agglomeration of asphaltene particles. Cohesive interactions of particles were modelled using empirical correlations where coefficients were fitted to a smaller-scale experiment. The model could simulate a uniform, continuous deposit blocking ~ 30% of the pipe-cross section with no overall flow reduction. A similar approach was used by Rukhlenko et al.⁵ to simulate thrombosis in a blood vessel. This work used a single-phase CFD model coupled with a population balance approach to define a porous zone where the blood coagulation happened and resulting fibrin structures were deposited. The simulations resulted in flow maps highlighting intervals of vessel sizes and Reynolds numbers where the thrombus formation was most probable. Labois et al.⁴ presented a more complex three-phase Eulerian-Eulerian model of gas hydrate deposition in the subsea conditions of gas leakage. An innovative aspect of the proposed simulation approach was defining the second, stationary hydrate phase generated from the moving hydrate phase when it adhered to a structure. However, this transition's details were unclear as the authors did not present sufficient details of the simulation approach. The considered models^{3,4} were based on empirical closure relations and required input of several fitting parameters determined experimentally. Moreover, none of the models was verified against a relevant experimental benchmark.

A more accurate simulation approach would consider interactions of individual particles during the plugging. In this case, an Eulerian CFD model is combined with a Lagrangian Discrete Element Method (DEM) capable of reproducing inter-particle collisions. Several works used this method to study the clogging of relatively large particles at local flow restrictions. They considered how various parameters affect plugging, such as particle size, concentration, velocity, and shape. The study by Hilton et al.⁶ focused on the effect of particle shape on the volumetric dynamics of pneumatic transport systems. This model treated collisions of ~ 400- μ m particles using a standard soft-sphere model with the so-termed *spring*, *dash-pot*, and *slider*. The model, validated against experiments, was capable of depicting particle slugs blocking the entire cross-section of the pipe. Interestingly,

Department of Mechanical and Marine Engineering, Western Norway University of Applied Sciences, 5063 Bergen, Norway. email: Nazerke.Saparbayeva@hvl.no

the simulations demonstrated that spherical particles or those close to spherical shape led to stable flow at volume fractions around 60%, while ellipsoidal particles led to slug formation when the ellipticity was under 0.7 or above 1.3. Yang et al. used the CFD-DEM method to examine the plugging of particles in the shale pores⁷. Their findings showed that particle size and concentration are crucial in plugging efficiency. Additionally, the authors noted that the particle velocity, roughness, and tortuosity significantly affect the blockage of the pores. Ma et al.⁸ utilized the CFD-DEM approach to investigate the blocking mechanism in pre-packed gravel screens commonly used in oil and gas wells. The study found that the size and concentration of large particles affected blockage, and increasing the screen's porosity could reduce particle accumulation. Mondal et al.⁹ studied the behaviour of particulate suspensions at a constriction for concentrations < 50% using the CFD-DEM method. Their research revealed that the resolved approach is suitable for systems where the particle size is comparable to the flow geometry. They also investigated the phenomenon of multi-particle hydrodynamic bridging. They found that the probability of clogging increases with particle volume concentration, suggesting a critical particle volume concentration for the spontaneous formation of bridges. The critical concentration was in the interval of 7–32% and dependent on the ratio between the particle size and the diameter of the flow restriction. A similar system was considered by Xu et al.¹⁰, who modelled the clogging of a constriction by polydisperse sand particles. They examined how particle size and shape affect clogging probability and found that the largest particles from the size distribution formed a particle jamming arch. The probability of clogging approached unity when $d_{84}/d_{16} > 1.8$. None of the abovementioned CFD-DEM studies considered plugging by cohesive particles.

Several studies investigated the process of plugging with cohesive particles. Shao et al.¹¹ analysed the mechanism of clogging in microchannels by the gas-solid flow where the particles were sticky due to liquid bridges and van-der-Waals interactions. The size of the channel was comparable with the size of the particle ($\sim d_p$), and the particles' Young modulus was lower than the respective parameter of most solid materials. The plugging event was defined as the channel blockage by a particle with no simultaneous stagnation in the gas phase. The simulation resulted in flow maps illustrating how the plugging depends on the particle Stokes number (St) and the Weber (We) number of the bridge. As follows from the maps, plugging took place for $St < 3.5$ and $We < 10$. Duan et al.¹² simulated an industry-relevant problem of methane hydrate blockage at two different flow restrictions in a water-dominant system. The CFD-DEM model treated cohesive collisions between particles, combining the Hertz-Mindlin approach with Johnson-Kendall-Roberts (JKR) cohesion model. A simplified validation of the model was performed comparing with the experimental pressure gradients for cases with no plugs in a homogeneous flow regime. The model reproduced the formation of a sand watch-like deposit at the restriction with no total flow stop by this deposition. The deposit size was proportional to the flow velocity and the size of solid particles. Wang et al.¹³ used a CFD-DEM approach to model gas-solid flow with hydrate particles through a pipe with varying diameters. The model simulated cohesive interactions using the JKR approach. Although the Young modulus of the particles was significantly below referent values for gas hydrates, and the surface energy of the particle is not provided in the paper, the simulation results were compared surprisingly well with the experiments. Further, the authors considered how the particles' deposition efficiency depends on mean flow velocity and the particle-to-diameter size ratio. The deposition efficiency appeared in the interval 2% to 34%, meaning that the model did not reproduce the process of plugging.

Concluding the introductory part, we note very few models are tailored to accurately predict mechanisms that govern the plug formation process. The models strongly rely on empiricism or fail to reproduce the process as it happens for most real-life situations: a full flow stop caused by a sticky deposit of particles. The models are not validated against a plugging experiment. This study addresses the challenges by introducing a CFD-DEM model validated against a well-defined experimental benchmark by Struchalin et al.² for plugging in an ice-decane slurry. Previously, in our study, Saparbayeva et al.¹⁴, we utilized the CFD-DEM model to investigate the ice-ice cohesive collision and obtained insights helpful to develop the CFD-DEM model for the entire flow. For the first time, the model reproduces the plug formation process in sufficient detail and demonstrates how the plugging depends on the critical parameters of the process.

Methods

Model description

The CFD-DEM approach employed an Eulerian-Lagrangian framework to solve the fluid and solid phases independently. The fluid phase was described by a system of turbulent, incompressible Navier-Stokes equations^{15,16}:

$$D\phi/Dt = 0; \quad D(\rho\phi\vec{u})/Dt = -\phi\nabla p + \phi(\mu + \mu^t)\nabla^2\vec{u} + \phi\rho\vec{g} - \vec{F}_p, \quad (1)$$

where ϕ is the volume fraction of the continuous phase, \vec{u} is the velocity of the continuous phase, ρ is the density of the continuous phase, p is the pressure, μ and μ^t are molecular and turbulent viscosity, \vec{g} is the acceleration due to gravity. The standard k-epsilon turbulence model computes the turbulent viscosity¹⁶. We further assumed that the heat transfer with the ambient environment did not sufficiently influence the properties of the continuous phase and then excluded the energy equation from the analysis. The combined effect of the drag and lift forces exerted by DEM particles in the continuous phase is presented by \vec{F}_p ¹⁴ for a computational cell.

Newton's second law governs the motion of the i th DEM particle¹⁵:

$$m_i \frac{d\vec{v}_i}{dt} = \vec{f}_{p,i} + \vec{f}_{l,i} + m_i\vec{g} - (m_i/\rho_p)\nabla p + \sum_{j=1,N} \vec{f}_{i,j}, \quad (2)$$

where m_i is the mass of the particle, \vec{v}_i is the particle's velocity, ρ_p is the density of the particle. The drag force is determined as $\vec{f}_{p,i} = \frac{\pi}{2} r_i^2 c_{D,i} \rho (\vec{u} - \vec{v}_i) |\vec{u} - \vec{v}_i|$, where $r_i = 200 \mu\text{m}$ is the radius of the particle, $c_{D,i}$ is Schiller-Naumann's drag coefficient^{14,17}. The lift force is calculated as $\vec{f}_{l,i} = c_l \rho \pi r_i^3 (\vec{u} - \vec{v}_i) \times \vec{\omega}$ with lift coefficient c_l

calculated according to Sommerfeld's expression¹⁸ and curl of the fluid velocity $\vec{\omega} = \nabla \times \vec{u}$. The contact forces induced due to the collision with the N of j th neighbour particles (or the walls) are given by f_{ij} . The DEM solver activates this term when the particles are expected to contact their collision pairs at the next temporal substep of the DEM model. The particle rotation is calculated by accounting for the described forces. This is in detail described in Saparbayeva et al.¹⁴

The Hertz-Mindlin contact model accounting for cohesion determines the contact forces acting between particles and walls during the collision. They are given in normal (n) and tangential (t) directions relative to the plane of collision whose normal points from the i th particle^{14,19}:

$$\vec{f}_{ij} = F_{ij}^{(n)} \vec{n} + F_{ij}^{(t)} \vec{t} \quad (3)$$

The contact force in the normal direction can be expressed as¹⁴:

$$F_{ij}^{(n)} = -K^{(n)} \delta^{(n)} - N^{(n)} v_{r,i}^{(n)} + F_C \quad (4)$$

where $\delta^{(n)}$ is the particle-to-wall overlap distance, $v_{r,i}$ is the inter-particle relative velocity, K and N represent the stiffness and the damping coefficients. These parameters depend on the particles' mechanical properties: the Young modulus, Poisson's ratio, and the coefficient of restitution (COR). The cohesive force is computed using the JKR approach²⁰ $F_C = 1.5\pi r_i \gamma_i$, where γ is the work of cohesion (γ_{ice}) or the work of the adhesion to walls (γ_{wall}). The tangential component of the contact force is determined in a similar to Eq. (4) fashion yet excluding the cohesive interaction $F_{ij}^{(t)} = -K^{(t)} \delta^{(t)} - N^{(t)} v_{r,i}^{(t)}$. A detailed description of the contact treatment is presented in Saparbayeva et al.¹⁴

Boundaries and mesh

The numerical model was developed in the commercial CFD-package STAR-CCM+ 2210 (specifically version 17.06.007). To tailor the simulation to the specific needs of our research, we extended its capabilities by incorporating user-written codes, known as 'field functions'. These field functions played a crucial role in our work by allowing us to modify the default settings and configurations of the standard model. The geometry of the computational domain resembles the test section of the experimental flow loop described in Struchalin et al.²: 20 cm long pipe with an internal diameter of 22 mm contains a 1 cm long orifice blocking 80% of the pipe cross-section. In the experiments, the orifice was used to induce plugging in the test section. To conserve computational costs, we produced two geometries: a full-scale 3D test section, which was further sliced to a quasi-2D element bounded by periodic boundaries in a horizontal direction orthogonal to the main flow. The thickness of the slice was equal to 3 diameters of the particle. The periodic boundaries recycled the secondary flow and particles in this direction. As presented in Fig. 1, other boundaries include the pressure at the inlet and outlet of the pipe, and the rest of the surfaces are no-slip walls. The computational mesh was made of 8 mm³ rectangular volumes. A rather coarse mesh resulted in elevated $Y^+ < 6$. This meshing was chosen to ensure the Lagrangian particles were subgrid¹⁷, which also complies with the software developers' guidelines¹⁶. For the current flow geometry, we did a mesh independence study. The analysis was conducted for mesh sizes ranging from 1 to 3 mm with a step size of 0.5 mm. When changing the mesh size, we noted a low statistical spread of plugging dynamics at $\sim 15\%$. Finally, we tested how a fully 3D case differs from a quasi-2D simplified model. To speed up the formation of the plug, we set the cohesion to the maximum 95% experimental value²¹ and used $\gamma_{ice} = \gamma_{wall} = 541 \text{ mJ/m}^2$. The difference was evaluated in terms of the rate of plug formation. The simulations revealed that the 2D results compared well to the 3D simulation with an average discrepancy of about 8%. However, we note the formation of more massive particle slugs in the 3D model. The 2D model used 142 times less computational time.

Model settings

Multiple parameters of the model were set according to experimental conditions to reproduce plugging experiments. The process of plugging took place for ~ 100 s, and the temperature in the cross-section linearly increased from -1.1 to -0.6°C during the process. The heating of the flow was due to the particle-wall friction. The

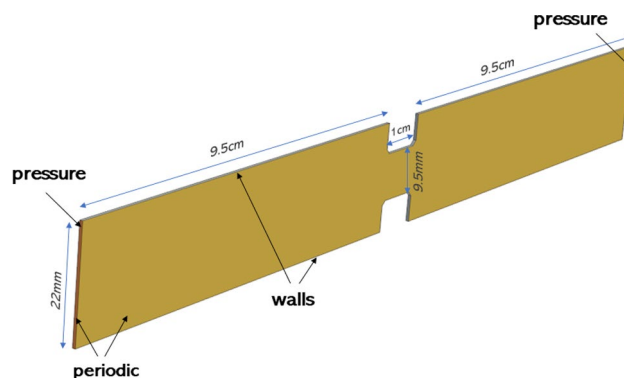


Figure 1. Geometry and boundaries.

molecular properties of the phases were set for the time-average temperature according to the NIST database²². Since plugging resulted in a continuous reduction of flow rate, a flow regime transition was expected at the end of the process. The model simulated this effect by scaling the turbulent viscosity to zero when the flow Reynolds number fell below 2300. Table 1 presents the parameters of the model.

For the mechanical properties of ice, we used the approach described in detail by Saporbayeva et al.¹⁴. We computed the normal coefficient of restitution ε_n accounting for lubrication force from decane using the method proposed by Joseph et al.²³ for particle Stokes numbers beyond 17. For the lower Stokes numbers, ε_n was set at 0.05. The tangential coefficient of restitution was assumed to be unaffected by lubrication and then equal to the so-called “dry” value $\varepsilon_t = 0.8$ ²⁴. Poisson’s ratio for ice was set as 0.36²⁵. To limit the computational costs by increasing the DEM temporal sub-stepping^{14,16}, the Young modulus of the particle was artificially reduced below the real values²⁶ to 0.1 MPa. We carried out simulations to test the influence of this parameter on the dynamics of the process. The model was weakly sensitive to the increase of the Young modulus by 3 orders as the average change pipe blockage dynamics was $\sim 30\%$ while resulting in a 15-fold increase of the computational time. Although the rolling resistance may be significant in contact interactions²⁷, the rolling friction coefficient was set at a low value of 0.001. Additional experiments are required to determine this parameter accurately for interactions of ice in decane. The default mechanical properties of glass¹⁶ were set for the walls of the computational domain.

We extended the model to more effectively account for temperature-dependent variables, including friction and cohesion, which previous studies have identified as significant factors influencing ice collisions¹⁴. The experimental temperature log was imported into the model. The cohesive surface energy was set linearly increasing with the temperature. For this, we interpolated experimental measurements for ice in decane presented by Yang et al.²¹. In the interpolation, we used data points obtained in the interval $-4.0 \dots -1.5^\circ\text{C}$ where $\gamma_{ice} \sim 21 \dots 172 \text{ mJ/m}^2$. The cohesive energy is calculated in the JKR limit from the micromechanical force measurements reported by Yang et al.²¹. We note that these values of cohesion energy are about 3-orders greater than the cohesion of clotted blood particles²⁸.

A similar interpolation was conducted for the coefficient of friction fr based on the data from Sukhorukov²⁵. For the interpolation, we used measurements taken in the interval $-8.0 \dots 1.8^\circ\text{C}$ for the shortest contact time between ice surfaces. The friction coefficient was in the interval $\sim 0.60 \dots 0.69$. The friction coefficient reduced with the temperature.

The adhesive energy of ice to the walls of the test section filled with decane and the coefficient of friction with the walls are not explicitly available in the literature. According to Aspenes et al.²⁹, the adhesion is proportional to the free energy of the solid surface. The free energy of the walls²⁹ is lower than the cohesive energy of ice²¹. The friction coefficient of ice at the pipe material is also lower than the ice-to-ice friction²⁵. Therefore, we explored how the ratio of the ice-wall adhesion to the ice-ice cohesion $c_r = \gamma_{ice}/\gamma_{wall} < 1$ influences the simulation results. We also noted that ice adhesion to different materials reduces with temperature^{30,31}. Therefore, as a conservative estimate, the adhesion was set as a constant proportional to the initial value of cohesion. We also assumed that the friction coefficients between the particles and the walls were scaled proportionally to c_r .

The pressure at the inlet was specified to reproduce the experimental mass flow with neutrally buoyant and non-cohesive particles, which was determined in separate calibration simulations. Zero velocity and pressure fields were used as initial conditions for simulations. Initially, the flow field in the test section was established for about 2 s to the experimental value without DEM particles. In this way, we prevented the formation of particulate deposits during the start-up phase of the process. Then, the particles were injected at the inlet at 13 000 1/s, corresponding to the experimental volume fraction. To avoid phase slip at the inlet, mean flow velocity was continuously monitored and over-prescribed as the inlet velocity of DEM particles. In this model, we assumed that the significant deposition of the particles took place in the test section and neglected possible deposition in the rest of the experimental system. Moreover, due to the large volume of the system compared with the volume of the test section, we assumed that the deposition of the particles in the test section did not significantly influence the volume fraction of the particle at the inlet.

We used the SIMPLE in STAR-CCM+^{14,32} to solve governing equations for the continuous phase. The following relaxation coefficients were set for the solver: 0.8 velocity, 0.2 pressure, 0.9 volume fraction, and 0.9

Diameter of particles d_i	400 μm
Density of fluid ρ	747 kg/m^3
Density of particles ρ_p	916 kg/m^3
Fluid viscosity μ	1.25 mPa s
Normal COR ε_n ²³	$0.8 + 1.8 \ln x_c/x_0/St_0$, 0.63 ^a , 0.8 ^b
Tangential COR ε_t	0.8
Sliding friction coefficient f	$-0.015T + 0.574$, 0.1–0.6 ^b
Rolling friction coefficient μ_r	0.001
Surface energy γ	$0.280 + 0.061T$, 0.541 ^b J/m^2
Young’s modulus E_p	0.1 MPa
Poisson’s ratio ν_p	0.36

Table 1. Model parameters. Relative Stokes number $St_0 = m_i v_{r,i}/6\pi\mu r_i^{2/3}$, $x/x_0=10^{-3}$, T is the experimental temperature in $^\circ\text{C}$. ^aAsymptotic value, ^bSimplified simulations.

turbulence model. The equations were spatially discretized using upwind discretization in space and the implicit Euler method (2nd order) in time. The time step was 0.5 ms. The time step of the DEM model parameter was set at 20% of the duration of the Rayleigh wave propagation through the particle^{16,33}. The absolute values of the DEM time step were $\sim 20\mu\text{s}$.

Results and discussion

Model validation

It is noteworthy to highlight the significance of previous studies as they have contributed to our understanding of particle deposition and cohesive interactions in a pipe flow. We validated the applied CFD-DEM model with no account for cohesion in Eq. (4). First, we reproduced the blockage for the process described in Mondal et al.⁹. The obtained results reproduced clogging of the flow channel at a particle volume concentration of 13% close to the value of 10% reported in the original work. In addition, by applying the non-cohesive CFD-DEM approach to experimental data sets, we successfully simulated dune formation in a microchannel during horizontal hydraulic transport³⁴. The predicted velocity of the dunes exhibited a 10.7% deviation from the corresponding experimental values. Cohesive particles significantly contribute to block formation in this study. It is worth noting a related study using our CFD-DEM model with included cohesion accurately predicted restitution coefficients, with a 10% average deviation from experimental data¹⁴.

The CFD-DEM model was then validated against the experiment by Struchalin et al.². The model reproduced experimental case 2 from Struchalin et al.², where a plug was formed in the test section at an initial flow rate of 400 kg/h and a particle concentration of 6.8%. For this system, cohesion was known from the experiments by Yang et al.²¹ while the adhesion and the friction of the particles at the walls were fitted parameters. They were tuned proportionally to the cohesion to match the experiment. The left plot in Fig. 2 demonstrates how the mean flow velocity changed with time during the plugging of the pipe. We note a slug-like behaviour of the flow in the CFD-DEM model for low adhesion cases. This is connected to more sticky particles re-dispersed deposits formed at less sticky walls. This phenomenon is illustrated in Fig. 3A. As presented in Fig. 3B, in these simulations, the maximum coefficients of restitution for the particle-particle and particle-wall conditions reduced from 0.8 to 0.55 and 0.35 due to the lubrication effects (see Methods). The reduced restitution coefficients contribute to the faster plugging of the test section.

The best correspondence to the experiments was obtained when adhesion and friction were $\sim 88\%$ of the cohesion; the average discrepancy of the model was 25%. For lower adhesion, the simulated velocity sharply reduced to $\sim 50\%$ of the initial values; the flow rate remained at this value for 60–100 s without a significant reduction due to the re-dispersion of the deposited particles. However, as the model incorporated the experimental temperature log and the cohesion was set dependent on the temperature, this parameter increased with time. Large particle slugs formed when the cohesion significantly increased. At the end of the process, the slugs blocked the orifice. For the high adhesion values, the step-wise shape of the experimental curve corresponded to the experimental. The differences are addressed in the secondary deposition and jamming in other parts of the experimental system that are not modelled in CFD-DEM (e.g. pump, mixing tank, flow meter). The respective growth of the secondary flow resistance in non-modelled locations contributes to the rate of flow velocity reduction.

It is interesting to consider how the CFD-DEM model reproduced the third-party flow maps. We present this information in Fig. 2 (right). Here, we collect data for flow regimes in horizontal flows of slurries and suspensions of particles. To exclude the influence of pipe material, we set $c_r = 1$. Next, speeding up the simulations, $fr = 0.6$, which is the maximum for the considered system, and $\varepsilon_n = 0.63$ corresponding to the maximum relative velocity.

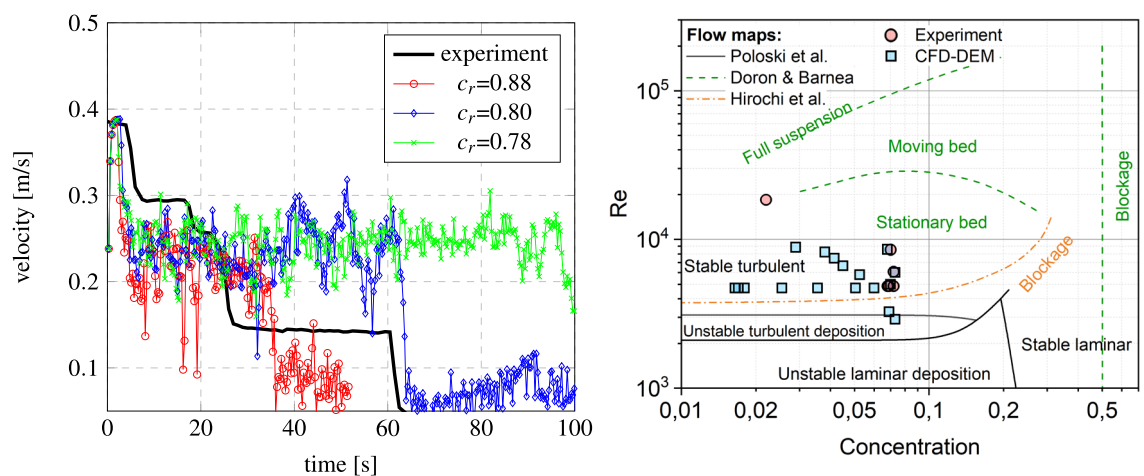


Figure 2. CFD-DEM model compared with experimental results: (left) average flow velocity as a function of time for difference cohesion to adhesion ratios $c_r = \gamma_{wall}/\gamma_{ice}$ compared to Struchalin et al.² at $Re = 4996$, $\phi_p = 6.8\%$; (right) flow maps by Poloski et al.³⁵, Doron and Barnea³⁶, Hirochi et al.³⁷, Struchalin et al.² (Experiment) compared with the CFD-DEM predictions at $c_r = 1$, $\varepsilon_n = 0.63$, $fr = 0.6$.

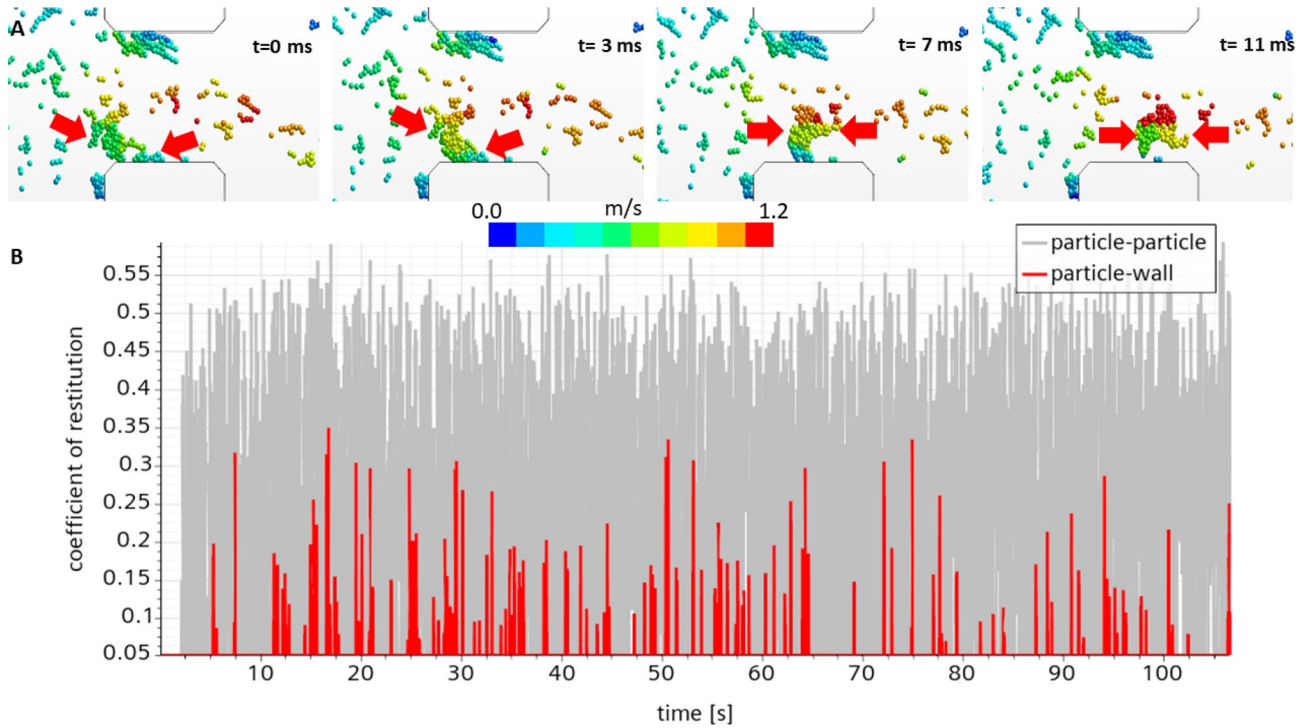


Figure 3. (A) Scrubbing of deposited particles from the walls. Color scale denotes the magnitude of the continuous phase velocity. (B) Coefficient of restitution for particle-particle and particle-wall collisions.

The experiments are compared with cases where simulations resulted in plugging of the test section. As in the experiments by Strcuhalin et al.², the model reveals plugging in flow regimes where stationary deposits with no plugging are supposed to be formed. This is an expected trend since the maps are developed for particles with significantly lower cohesion and adhesion. However, the model corresponds to the referent experiment demonstrating plugs and the flow rates below the experimental and comparable concentrations.

Plugging dynamics

Figure 4 considers the dynamics of blockage in more detail. Here, to shorten the simulation and limit the re-dispersion of the particles, we set the cohesion to the maximum experimental value 541 J/m² according to Yang et al.²¹, neglect lubrication, and minimize the friction. The simulation results reveal a continuous reduction of mean flow velocity after the particles were injected at t = 2 s. Shortly after the injection, the particles were driven

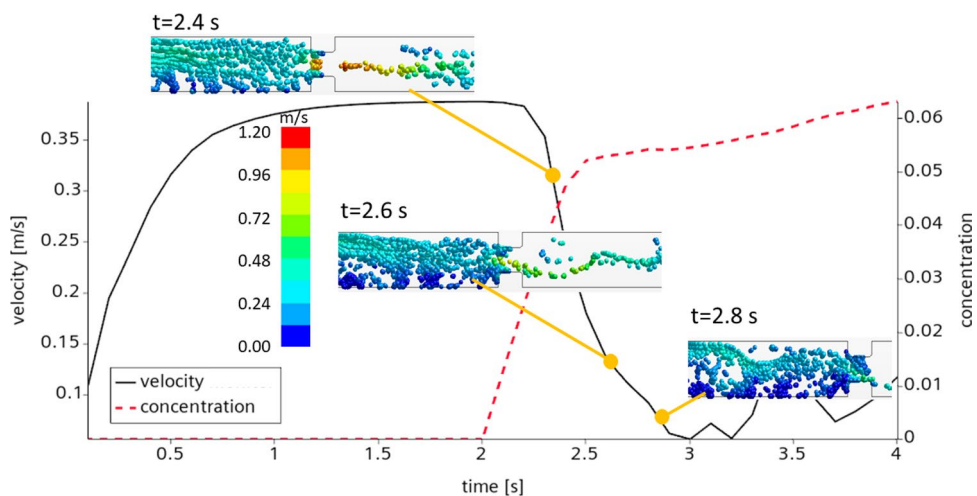


Figure 4. Dynamics of plug formation. Surface energy $\gamma_{ice} = \gamma_{wall} = 541 \text{ J/m}^2$, mean flow velocity $\bar{u} = 0.39 \text{ m/s}$, particle concentration $\phi_p = 5.9\%$, coefficient of restitution $\varepsilon_n = 0.8$, $fr = 0.1$. Flow direction from left to right, color scale denotes the magnitude of the continuous phase velocity.

to the bottom of the pipe, where they adhered to the walls and formed stationary deposits. The volume fraction of the particles in the deposits was about 50%, close to the packing limit reported in the benchmark study². Once the deposition progressed, the particles experienced inertial deposition at the surface of the orifice for $t = 2.6$ s. Smaller deposits were built both at the frontal part of the orifice and directly in its throttle. The deposition resulted in an elevated flow resistance, which led to a dramatic flow reduction for a fixed pumping pressure drop. As in the experiments², the plug was formed at the very end of the process due to trapping the bottom deposits with those formed at the orifice. After the stationary plug was formed, the flow experienced low-magnitude oscillations. This choking happens due to the inertial motion of particles in the upflow part of the test section.

Sensitivity analysis

In addition to blockage dynamics, we evaluated the validity of the model's response to variation in flow rate (Reynolds number), the concentration of particles, and the granular capillary number² $Ca = \bar{u}\mu/\gamma_{ice}$ with \bar{u} which is an average flow velocity. These parameters were defined at the inlet of the model. As in the flow map study, to speed up this parametric analysis, we used constant cohesion and restitution coefficients without accounting for lubrication. We aimed to highlight how the blockage time depended on these parameters. The simulation results are presented in Fig. 5. The left plot in this figure illustrates a correlation between the temporal duration of blockage, the Reynolds number, and the concentration of particles. The considered interval of Reynolds numbers is relevant in the food industry (e.g. ice slurries³⁸) and represents transient cases in petroleum and mining industries³⁹. The findings clearly indicate that when the volume fraction of particles exceeds 4%, the blockage time is consistently below 10 s. As the particle concentration rises, it increases the probability of particle interaction and agglomeration. Consequently, this contributes to the rapid formation of blockages within the pipe. The relationship between blockage time and Reynolds number shows the transition point. Prior to reaching a Reynolds number of approximately 6000, a consistent uprising trend is observed. However, beyond this threshold, a reduction in blockage time becomes apparent. Then, at $Re \approx 8000$, the blockage time dramatically increases, so the blockage takes several hundreds of seconds. The observed trend is rather straightforward as by increasing the Re we increased the relative velocity between the particles and then reduced the efficiency of clogging due to cohesion. However, the number of collisions also increases with Re , which is the reason for the existence of the local minimum blockage time. The right plot in Fig. 5 highlights the significance of the capillary number, which is inversely proportional to adhesion. Reading the plot, it becomes apparent that the blocking time remains mostly within the range of 0–10 s for different capillary number values. The blockage time is inversely proportional to the capillary number. In these simulations we highlighted the influence of cohesion reducing the mechanical deformations ($\varepsilon_n = 0.8$) and the friction ($fr = 0.1$). We again note a non-linear trend when increasing the cohesion. Namely, at $Ca \approx 2 \cdot 10^{-3}$, the blockage speeds us by a factor of two. This happens due to the enhanced scrubbing of deposited particles from the walls by the clusters of those remaining in the bulk of the flow, promoting partial re-suspension of particles, slugging, and thus bringing more particles to the orifice. When the cohesion increased from this point, the effect is compensated by even more intense deposition.

Concluding remarks

This study demonstrates that the CFD-DEM approach is capable to reproduce the process of plugging in turbulent multiphase flows with cohesive/adhesive particles with minimal modifications to the standard model. Our model was simplified and based on several assumptions: 2D geometry, low Young modulus, and no influence of the entire experimental system considered. The simulations do however return reasonable results when experimental measurements well support the cohesive properties and the concentration of particles. From the simulations, we found that the inertial collisions and the gravity-driven deposition are the dominant mechanisms leading to plugging the pipe. Although many flow maps are developed to account for these phenomena, the stickiness of the particles, in our case, dislocates plugging towards lower concentrations and higher flow rates on the map.

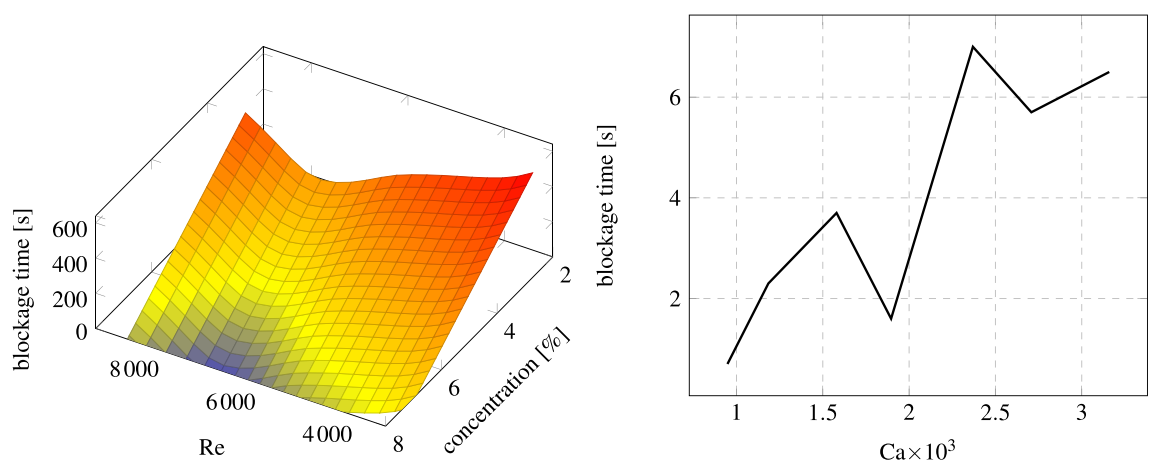


Figure 5. Blockage time as a function of flow Reynolds number, particle concentration ϕ_p , and Ca when the following parameters are fixed: (left) $c_r = 1.00$, $Ca = 1.18 \cdot 10^{-3}$, $\varepsilon_n = 0.63$, $fr = 0.60$; (right) $c_r = 1.00$, $Re = 4714$, $\phi_p = 6.90\%$, $\varepsilon_n = 0.8$, $fr = 0.1$.

The CFD-DEM method provides excellent insight into the physics of the process. However, due to the high computational costs, which can extend up to 12 h on a system utilizing 30 CPUs of AMD Ryzen Threadripper PRO 3975WX at 3.8 GHz, this approach is hardly applicable for simulating the entire flow system or providing decision support. A more pragmatic yet accurate simulation approach still needs to be developed.

Data availability

The datasets used and/or analysed during the current study are available from the corresponding author on reasonable request.

Received: 20 July 2023; Accepted: 4 October 2023

Published online: 11 October 2023

References

- Zuriguuel, I. *et al.* Clogging transition of many-particle systems flowing through bottlenecks. *Sci. Rep.* **4**, 7324 (2014).
- Struchalin, P. G., Øye, V. H., Kosinski, P., Hoffmann, A. C. & Balakin, B. V. Flow loop study of a cold and cohesive slurry. Pressure drop and formation of plugs. *Fuel* **332**, 126061 (2023).
- Eskin, D., Ratulowski, J., Akbarzadeh, K. & Pan, S. Modelling asphaltene deposition in turbulent pipeline flows. *Can. J. Chem. Eng.* **89**, 421–441 (2011).
- Labois, M., Pagan, N., Lakehal, D. & Narayanan, C. Computational modelling of subsea hydrate formation and associated risks and impact on flow assurance. In *Proceeding of 10th International Conference on CFD in the Minerals and Process Industries (CFD-2014)* (2014).
- Rukhlenko, O. S., Dudchenko, O. A., Zlobina, K. E. & Guria, G. T. Mathematical modeling of intravascular blood coagulation under wall shear stress. *PLoS ONE* **10**, e0134028 (2015).
- Hilton, J. & Cleary, P. The influence of particle shape on flow modes in pneumatic conveying. *Chem. Eng. Sci.* **66**, 231–240 (2011).
- Yang, X. *et al.* CFD and DEM modelling of particles plugging in shale pores. *Energy* **174**, 1026–1038 (2019).
- Ma, C. *et al.* CFD-DEM investigation of blocking mechanism in pre-packed gravel screen. *Eng. Anal. Bound. Elem.* **132**, 416–426 (2021).
- Mondal, S., Wu, C.-H. & Sharma, M. M. Coupled CFD-DEM simulation of hydrodynamic bridging at constrictions. *Int. J. Multiph. Flow* **84**, 245–263 (2016).
- Xu, S., Sun, H., Cai, Y. & Geng, X. Studying the orifice jamming of a polydispersed particle system via coupled CFD-DEM simulations. *Powder Technol.* **368**, 308–322 (2020).
- Shao, Y., Ruan, X. & Li, S. Mechanism for clogging of microchannels by small particles with liquid cohesion. *AIChE J.* **67**, e17288 (2021).
- Duan, X. *et al.* Simulation of the hydrate blockage process in a water-dominated system via the CFD-DEM method. *J. Nat. Gas Sci. Eng.* **96**, 104241 (2021).
- Wang, Z. *et al.* Numerical modeling of hydrate particle deposition in pipes with diameter reduction. *SPE J.* **28**, 522–539 (2023).
- Saparbayeva, N. *et al.* Cohesive collisions of particles in liquid media studied by CFD-DEM, video tracking, and Positron Emission Particle Tracking. *Powder Technol.* **426**, 118660 (2023).
- Zhou, Z., Kuang, S., Chu, K. & Yu, A. Discrete particle simulation of particle–fluid flow: model formulations and their applicability. *J. Fluid Mech.* **661**, 482–510 (2010).
- Siemens Digital Industries Software. Simcenter STAR-CCM+ User Guide v. 2020.1 (Siemens 2020).
- Crowe, C., Sommerfeld, M. & Tsuji, Y. *Multiphase Flow with Droplets and Particles* (CRC Press, 1998).
- Sommerfeld, M. *et al.* Theoretical and experimental modelling of particulate flows. *Lect. Ser.* **6**, 3–7 (2000).
- Hellestø, A. S., Ghaffari, M., Balakin, B. V. & Hoffmann, A. C. A parametric study of cohesive particle agglomeration in a shear flow-numerical simulations by the discrete element method. *J. Dispers. Sci. Technol.* **38**, 611–620 (2017).
- Johnson, K. L. & Johnson, K. L. *Contact Mechanics* (Cambridge University Press, 1987).
- Yang, S.-O., Kleehammer, D. M., Huo, Z., Sloan, E. & Miller, K. T. Temperature dependence of particle-particle adherence forces in ice and clathrate hydrates. *J. Colloid Interface Sci.* **277**, 335–341. <https://doi.org/10.1016/j.jcis.2004.04.049> (2004).
- Thermophysical properties of Decane. NIST chemistry webbook. <https://webbook.nist.gov>. Accessed 24 Nov 2022.
- Joseph, G., Zenit, R., Hunt, M. & Rosenwinkel, A. Particle-wall collisions in a viscous fluid. *J. Fluid Mech.* **433**, 329–346 (2001).
- Reitter, L. M., Mayrhofer, A., Tropea, C. & Hussong, J. Experimental investigation of normal and oblique impact of ice particles onto a wetted wall. In *AIAA AVIATION 2022 Forum*, 3533 (2022).
- Sukhorukov, S. *Ice-Ice and Ice-steel friction in field and in laboratory*. Ph.D. thesis, Norwegian University of Science and Technology (2013).
- Traetteberg, A., Gold, L. W. & Frederking, R. M. W. *The Strain Rate and Temperature Dependence of Young's Modulus of Ice* (Division of Building Research, National Research Council, 1975).
- Kronlachner, T., Pirker, S. & Lichtenegger, T. Block-movement-based calibration of a discrete element model for fine, cohesive powders. *Powder Technol.* **421**, 118411 (2023).
- McKenzie, A. J., Doyle, B. J. & Aman, Z. M. Micromechanical force measurement of clotted blood particle cohesion: Understanding thromboembolic aggregation mechanisms. *Cardiovasc. Eng. Technol.* **13**, 816–828 (2022).
- Aspenes, G. *et al.* Adhesion force between cyclopentane hydrates and solid surface materials. *J. Colloid Interface Sci.* **343**, 529–536 (2010).
- Baker, H., Bascom, W. D. & Singleterry, C. The adhesion of ice to lubricated surfaces. *J. Colloid Sci.* **17**, 477–491 (1962).
- Landy, M. & Freiburger, A. Studies of ice adhesion: I. Adhesion of ice to plastics. *J. Colloid Interface Sci.* **25**, 231–244 (1967).
- Akhshik, S., Behzad, M. & Rajabi, M. Cfd-dem simulation of the hole cleaning process in a deviated well drilling: The effects of particle shape. *Particuology* **25**, 72–82 (2016).
- Vinh, P. C. & Ogden, R. On formulas for the Rayleigh wave speed. *Wave Motion* **39**, 191–197 (2004).
- Saparbayeva, N., Kosinski, P., Dumazer, G., Fischer, M. & Balakin, B. Simulation of horizontal hydraulic conveying and dune formation based on CFD-DEM. In *AIP Conference Proceedings of ICNAAM 2022* (in press).
- Poloski, A. *et al.* *Deposition Velocities of Non-Newtonian Slurries in Pipelines: Complex Simulant Testing*, vol. PNNL-18316 WTP-RPT-189 Rev. 0 (2009).
- Doron, P. & Barnea, D. Flow pattern maps for solid-liquid flow in pipes. *Int. J. Multiph. Flow* **22**, 273–283. [https://doi.org/10.1016/0301-9322\(95\)00071-2](https://doi.org/10.1016/0301-9322(95)00071-2) (1996).
- Hirochi, T., Yamada, S., Shintate, T. & Shirakashi, M. Ice/water slurry blocking phenomenon at a tube orifice. *Ann. N. Y. Acad. Sci.* **972**, 171–176. <https://doi.org/10.1111/j.1749-6632.2002.tb04569.x> (2002).
- Kauffeld, M., Kawaji, M. & Eglolf, P. W. *Handbook on Ice Slurries* 359 (International Institute of Refrigeration, 2005).
- Ding, L. *et al.* Rheology of natural gas hydrate slurry: Effect of hydrate agglomeration and deposition. *Fuel* **239**, 126–137 (2019).

Acknowledgements

We acknowledge the Research Council of Norway for supporting this work. The authors thank dr. Pavel G. Struchalin from Western Norway University of Applied Sciences for his help with the construction of the flow map.

Author contributions

The authors contributed equally to this study. Both authors contributed equally to this work, collaborating on writing all manuscript sections.

Funding

Funding was provided by Norges Forskningsråd (Grant No. 300286).

Competing interests

The authors declare no competing interests.

Additional information

Correspondence and requests for materials should be addressed to N.S.

Reprints and permissions information is available at www.nature.com/reprints.

Publisher's note Springer Nature remains neutral with regard to jurisdictional claims in published maps and institutional affiliations.



Open Access This article is licensed under a Creative Commons Attribution 4.0 International License, which permits use, sharing, adaptation, distribution and reproduction in any medium or format, as long as you give appropriate credit to the original author(s) and the source, provide a link to the Creative Commons licence, and indicate if changes were made. The images or other third party material in this article are included in the article's Creative Commons licence, unless indicated otherwise in a credit line to the material. If material is not included in the article's Creative Commons licence and your intended use is not permitted by statutory regulation or exceeds the permitted use, you will need to obtain permission directly from the copyright holder. To view a copy of this licence, visit <http://creativecommons.org/licenses/by/4.0/>.

© The Author(s) 2023

APPLICATION OF MACHINE LEARNING TO PREDICT BLOCKAGE IN MULTIPHASE FLOW

Nazerke Saparbayeva, Boris V. Balakin, Pavel G. Struchalin, Talal Rahman and Sergey Alyaev

Submitted to Computation, MDPI

Article

Application of machine learning to predict blockage in multiphase flow

Nazerke Saparbayeva ¹ , Boris V. Balakin ¹, Pavel G. Struchalin¹, Talal Rahman ² and Sergey Alyaev ³

¹ Department of Mechanical and Marine Engineering, Western Norway University of Applied Sciences, 5063 Bergen, Norway

² Department of Computer Science, Electrical Engineering and Mathematical Sciences, Western Norway University of Applied Sciences, 5063 Bergen, Norway

³ NORCE Norwegian Research Centre, 5008 Bergen, Norway

* Correspondence: Nazerke.Saparbayeva@hvl.no

Abstract: This study presents a machine learning-based approach to predict blockage in multiphase flow with cohesive particles. The aim is to predict blockage based on parameters like Reynolds and capillary numbers using a random forest classifier trained on experimental and simulation data. Experimental observations come from a lab-scale flow loop with ice slurry in the decane. The plugging simulation is based on coupled Computational Fluid Dynamics with Discrete Element Method (CFD-DEM). The resulting classifier demonstrated high accuracy, validated by precision, recall, and F1-score metrics, providing precise blockage prediction under specific flow conditions. Additionally, sensitivity analyses highlighted the model's adaptability to cohesion variations. Equipped with the trained classifier, we generated a detailed machine-learning-based flow map and compared it with earlier literature, simulations, and experimental data results. This graphical representation clarifies the blockage boundaries under given conditions. The methodology's success demonstrates the potential for advanced predictive modelling in diverse flow systems, contributing to improved blockage prediction and prevention.

Keywords: multiphase flow; blockage prediction; machine learning classifier; CFD-DEM simulations; flow loop experiments.

0. Introduction

The issue of pipeline blockage is relevant in multiple industries, resulting in environmental concerns and financial losses. Applying machine learning methods is becoming a promising solution in flow assurance [1]. This methodology is a potentially powerful tool for analyzing, classifying, and predicting flow regimes, including critical aspects such as pipeline blockage. Numerous studies exist where machine learning methods consider challenges associated with multiphase flows and pipeline blockages.

Manikonda et al. [2] applied machine learning methods to identify vertical gas-liquid two-phase flow regimes. The study aimed to determine the current flow regime using data collected from over thirty articles and two experimental flow loops. They utilized supervised and unsupervised ML classification models, including a Multi-class Support Vector Machine, K-nearest neighbour Classifier, K-means clustering, and hierarchical clustering to separate different flow regions. The study found that the K-Nearest Neighbor Classifier achieved a 98 % classification accuracy and matched the flow regime maps from Hasan et al. [3].

Similarly, Alhashem [4] employed a machine learning model using a Stanford Multiphase Flow Data dataset to classify multiphase flow regimes in a horizontal pipe. Fluid flow and pipe configuration descriptions were used as input variables, while the output corresponded to the flow regime type. The authors used the F-1 accuracy score as the performance metric to compare five machine learning methods. After evaluating five methods,

Citation: Lastname, F.; Lastname, F.; Lastname, F. Title. *Journal Not Specified* 2023, 1, 0. <https://doi.org/>

Received:

Revised:

Accepted:

Published:

Copyright: © 2024 by the authors. Submitted to *Journal Not Specified* for possible open access publication under the terms and conditions of the Creative Commons Attribution (CC BY) license (<https://creativecommons.org/licenses/by/4.0/>).

including decision tree, random forest, logistic regression, support vector machine, and neural network (multi-layer perceptron), the authors observed that the Decision Tree and Random Forest achieved the highest accuracy rates with 86% and 89%, respectively, with minimal training times less than 0.005 seconds.

While these studies have primarily focused on horizontal flows, Chaari et al. [5] introduces an Artificial Neural Network (ANN) model for steady-state liquid holdup estimation in two-phase gas-liquid flow, designed to be unifying and applicable across all pipe inclinations and flow patterns. Utilizing the ANN model, this study incorporates 16 dimensionless groups to effectively account for the inertial, viscous, and gravitational effects experienced by both the liquid and gas phases, based on a Stanford Multiphase Flow Database dataset. The proposed model outperformed two established models, showing improved coefficients of determination and significantly lower average absolute relative errors, with improvements of up to 57% in inclination ranges and 66% in various flow patterns.

In addition to the aforementioned non-particle-based studies, certain works show that machine learning methods have great potential for the future of hydrate management and studies of plugging in multiphase flows. It is relevant to evaluate these ML-models using three main criteria defining their industrial applicability: accuracy, size of the datasets, and scalability of the model parameters. Qin et al. [6] considered two machine learning methods: the support vector classifier (SVC) and the regression neural network (NN). The models were trained using 4500 experimental cases, which was the largest dataset of those used in plugging studies. The authors applied the ML-methods to analyze hydrate risks and construct field risk maps using an experimental flow loop and field databases. The accuracy of the SVC was about 0.99 while the NN method was $\sim 96\%$. Their study demonstrates that a coupled regression and classification learning model can simultaneously predict hydrate volume fraction and plugging risk using process variables. These variables include water cut, gas-oil ratio, liquid velocity, operating time within the hydrate domain, oil properties, and the inter-particle cohesive force of hydrates. However, these variables were not made dimensionless using the standard π -theorem analysis [7] so that the ML-models could be hardly scaled for applications other than hydrates.

Furthermore, Wang et al. [8] applied ML to assess the risk of hydrate formation and blockage in a pure water system. The multi-layer perceptron (MLP) model and the logistic regression (LR) model were used in this work. Although the models achieved 99% accuracy, the training dataset's size was dramatically limited as six cases were fed into the model. The researchers used data from experiments conducted in a high-pressure, entirely visual flow loop for the training. The input variables for these models included time, temperature, pressure drop, gas consumption, remaining water, and the water-cut ratio at each data point. The output of the models aimed to determine the risk of blockage and was based on defining three regions and two critical transition points in the hydrate formation process, namely the "action point" and the "blockage point." The input data was non-dimensionalized using the statistical parameters with StandardScaler [9]. However, the nondimensionalization did not follow the principles of π -theorem [7].

In recent years, scientists have started using machine learning techniques to predict and reduce wax deposits in petroleum pipelines, offering fresh approaches to address this common issue in the oil sector.

For instance, Kim et al. [10] integrated Artificial Intelligence (AI) through the Stacked Auto-Encoder (SAE) model, using an OLGA simulator to generate learning data and employing the RRR (Ryg, Rydahl, and Ronningen) model to describe the molecular diffusion and shear dispersion aspects of wax deposition. It demonstrates impressive accuracy in predicting the location and maximum volume of wax accumulation with over 90% accuracy. However, there may be discrepancies between the predicted wax thickness and actual data, possibly due to the limited initial dataset. Despite this, the model performs effectively at the early detection of wax deposition and accurately predicts the location and amount of wax buildup, showing potential in maintaining a continuous flow of petroleum pipelines.

Additionally, Amar et al. [11] proposed a multilayer perceptron model (MLP) for predicting the weight percent of deposited wax under different production conditions using experimental measurements. After utilizing the Levenberg-Marquardt algorithm (MLP-LMA) and Bayesian Regularization algorithm (MLP-BR) during the MLP's learning phase, it became evident that MLP-LMA outperformed MLP-BR with an overall root mean square error of 0.2198. Furthermore, its potential for digital implementation makes it more useful in controlling wax deposition in oil and gas pipelines.

Ahmadi [12] proposed a novel approach: combining fuzzy logic and genetic algorithm (GA) to create an efficient method for predicting wax deposition. The model considers important input variables such as oil composition, temperature, pressure, and oil-specific gravity. Parameters like mean square error and relative deviation are quantitative benchmarks, highlighting the model's accuracy and reliability. The developed model demonstrates high performance and reliability compared to other methods in determining wax deposition values, with the key advantage of rapid calculations and cost-effectiveness. However, like other modelling methods, the proposed machine learning models have limitations related to the range of input and output values. They can only be applied to oil samples and conditions similar to the available data.

After reviewing the aforementioned research, it becomes evident that the application of machine learning methods represents a potent tool for flow assurance issues, particularly for predicting multiphase flow regimes. Collectively, these studies contribute to the ongoing efforts to improve predictive methods for flow patterns, providing valuable insights into potential challenges such as pipeline blockages.

In previous studies, our group focused on understanding how particles can clog up flowing systems. In the work by Struchalin et al. [13], we expanded upon the experimental approach of Hirochi et al. [14] by conducting flow loop experiments employing a decane-oil slurry. These experiments involved controlling particle concentration and size and carefully regulating temperature to affect particle cohesion. Our work led to an improved understanding of the plugging process with the given experimental conditions. These findings act as a reference point for validating numerical models of plugging. In the second study by Saparbayeva and Balakin [15], we applied a CFD-DEM to better understand plug formation in a multiphase system with a cohesive dispersed phase. The process parameters were dimensionless according to the π -theorem principles [13]. Many models from the literature lacked validation against actual plugging experiments. To address these limitations, we introduced a CFD-DEM model validated against the well-defined experimental benchmark for plugging. Notably, our prior work by Saparbayeva et al. [16] laid the foundation for this model by investigating ice-ice cohesive collisions, offering valuable insights into successful application in understanding the entire flow process.

The novelty of this paper is highlighted by its ability to predict blockage without the need for model execution or experimental trials. This is achieved by integrating a machine learning model that utilizes experimental and CFD-DEM model datasets as inputs. In contrast to the previously discussed studies in machine learning application, our research introduces the application of a machine learning classification model to predict blockages in multiphase systems with unique characteristics, specifically the presence of ice particles in a decane-oil slurry. The presence of ice particles introduces an extra layer of complexity. In our case, this involves utilizing a more precise CFD-DEM model.

1. Methodology

The dataset used for the classifier's training consists of two parts: the plugging data collected in the flow loop experiments and the database of CFD-DEM simulations expanding the experimental dataset.

1.1. Experiments

The flow experiments were carried out using a lab-scale multiphase flow loop. A cohesive slurry of ice in decane circulated in the loop. These materials were chosen due

to the known cohesive surface energy for different temperatures below the ice formation point [17]. The ice particles were produced outside the flow loop by crushing ice blocks. The size of the particles was in the interval 200-400 μm . The particle size distribution was log-normal. The maximum volume fraction of particles used in experiments was 15%. The maximum Reynolds number $Re = \rho v d / \mu \sim 25000$, where ρ , μ are the density and the viscosity of decane, v is the mean flow velocity, and d is the diameter of the pipe. The flow loop consisted of a centrifugal pump, a temperature-controlled stirred tank, and a steel test section (ID=22 mm). Negative temperatures of -3...-1⁰ C were set in the loop by connecting tank coils to a chiller and thermally insulating the flow loop. Plugging occurred in the test section, where a 9.5-mm orifice was installed. The local resistance of the orifice and secondary wake flow in the corners of the orifice promoted the deposition and sticking of cohesive particles.

The flow loop and its hydraulic scheme are presented in Figure 1. The experiments were carried out by loading a controlled amount of ice in a highly agitated and pre-cooled flow, reducing the flow rate to a set point, increasing the temperature to a given value, and monitoring the flow using the mass flow meter. In addition, the measurement system of the loop included a differential manometer controlling the test section and thermocouples for temperature control. A successful plugging event was defined as a sensor-confirmed zero flow condition following the set point without further action from the loop operator. More details about the experiments are found in [13].

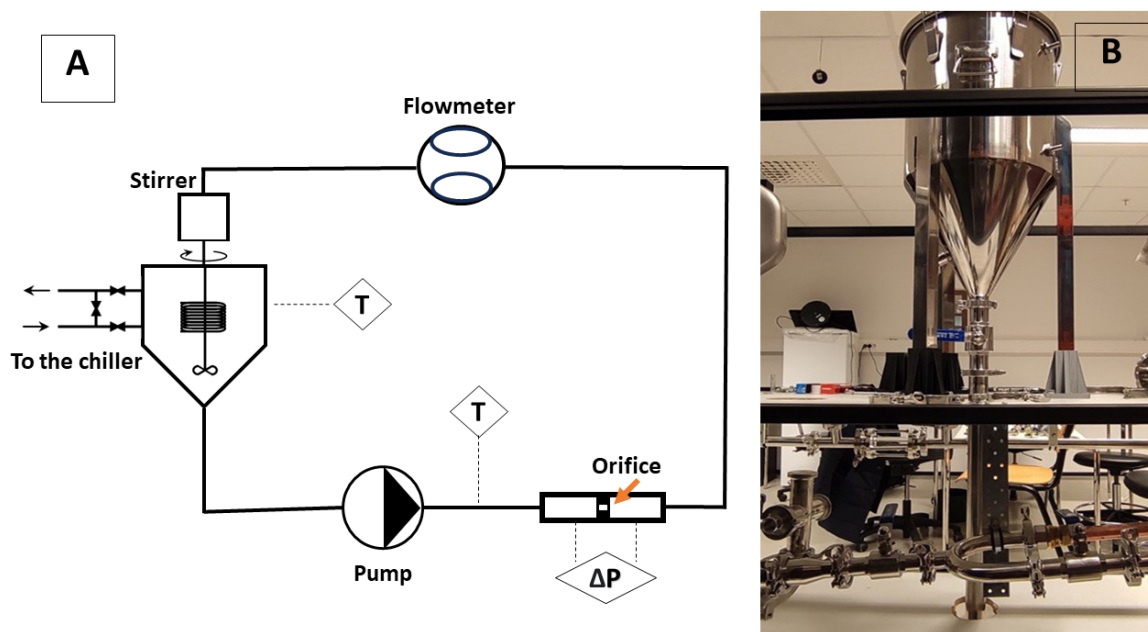


Figure 1. Hydraulic diagram of the experimental flow loop [A] and photo of the central part of the flow loop [B].

1.2. CFD-DEM model

To complement relatively few flow loop experiments, we generated additional data points from CFD-DEM model developed for this study. In particular, the CFD model allowed us to study cohesion parameters more closely. In the experiments, the cohesion was altered by changing the temperature of the coils in the tank. However, due to the large thermal inertia of the flow loop, the cohesion was defined with significant uncertainties. Therefore, a multiphase CFD-DEM model of the test section was built to highlight the influence of cohesive forces and to consider the physics of the plugging process in greater detail. The model was based on the Eulerian-Lagrangian approach, where Navier-Stokes equations described the flow of decane, while the particles were treated as Lagrangian

objects following Newtonian mechanics. The phases were coupled via drag, lift, and pressure gradient forces calculated in each computational cell of the model. The contact interactions between the particles were resolved using the so-termed "soft-sphere" technique, accounting for their deformations upon collisions. The Hertz-Mindlin approach was used for this purpose, considering cohesive forces acting during the collision. While the inter-particle cohesive energy γ was known from the third-party experiments, the particle-wall cohesion was not known in the experiments. Therefore, a ratio of the cohesive energy of the walls to the cohesive energy of the ice $c_r = \gamma_{wall} / \gamma_{ice}$ was used as a fitting parameter to validate the model. As the model treated every particle separately, and many particles were present in the experiments, this was required to limit the computational costs. Therefore, as shown in Figure 2(left), the geometry of the experiment was simplified to a thin slice of the test section bounded by periodic boundaries. A constant pressure drop resulting in the experimental flow rate was set at the ends of the model. The model is described in greater detail in Saparbayeva and Balakin [15].

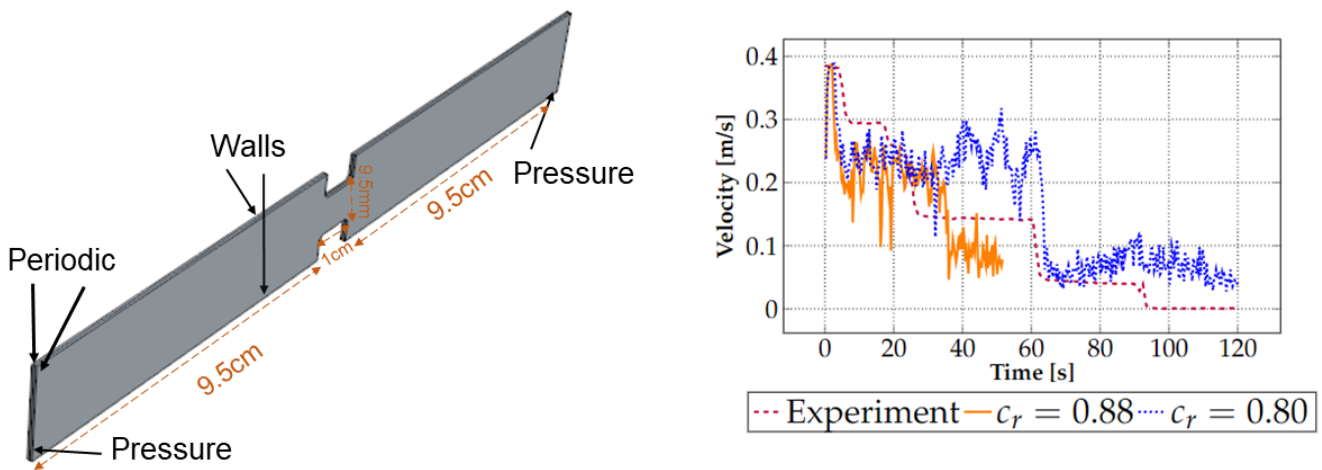


Figure 2. Geometry and boundary conditions of the model (left) and comparison between experimental data and CFD-DEM model: average flow velocity over time with different cohesion-to-adhesion ratios $c_r = \gamma_{wall} / \gamma_{ice}$ in comparison to the findings of Struchalin et al. [13] at Reynolds number $Re=4996$ and particle volume fraction $\phi_p=6.8\%$ (right).

1.3. Machine learning

We employ the random forest classifier as our machine-learning tool to analyze blockage in the considered multiphase flow. This choice is driven by the classifier's adaptability and robustness when dealing with multidimensional datasets, making the classifier a well-suited approach for our case with multiple parameters and features [18], [19]. The random forest classifier offers the advantage of feature importance analysis, enabling the identification of the critical factors of the process [20]. Additionally, this classifier type can handle non-linear data and overfits at a lower rate than similar ML techniques.

We implemented this method using the scikit-learn library, a standard Python tool for machine learning tasks [21]. Scikit-learn offers a user-friendly interface for methods like the random forest and supports various models and data processing techniques. Adjusting model parameters and evaluating performance allows for a comprehensive analysis of the classifier's usage.

The flowchart of the constructed ML technique is presented in Figure 3. We used input data from two primary sources to train our model: experimental flow loop data and CFD-DEM simulations. Each entry in the input file contains four key parameters: Reynolds number, concentration, capillary number, and the fourth parameter, a binary classifier

indicating whether blockages are present or absent in the system. The Reynolds number is a dimensionless parameter used to evaluate the significance of inertial forces compared to viscous forces in a fluid motion, while the capillary number indicates the balance between viscous forces and surface tension forces in a system. To evaluate the model's performance and ensure its stability, we employed a cross-validation method with a parameter $k=5$. This means the treated multidimensional datasets were divided into five folds (subsets) for training and testing. Each model was trained on four folds. 80% of data and tested on the remaining 20% of the data. The cross-validation procedure was repeated five times with different fold combinations. The outcome is the model performance verification. In total, 150 cases were used for the training.

In the machine learning model, we adjusted several key parameters to optimize the model's performance. We selected a fixed random seed value of 42 and set the random forest classifier with 100 estimators while limiting the maximum depth of each decision tree to 10. These parameters were selected to establish a well-balanced model combining accuracy and adaptability across various parameter conditions. Other parameters are configured with their default values. After selecting the best hyperparameters, we train a final Random Forest classifier on 100% of data to produce the most accurate flow map.

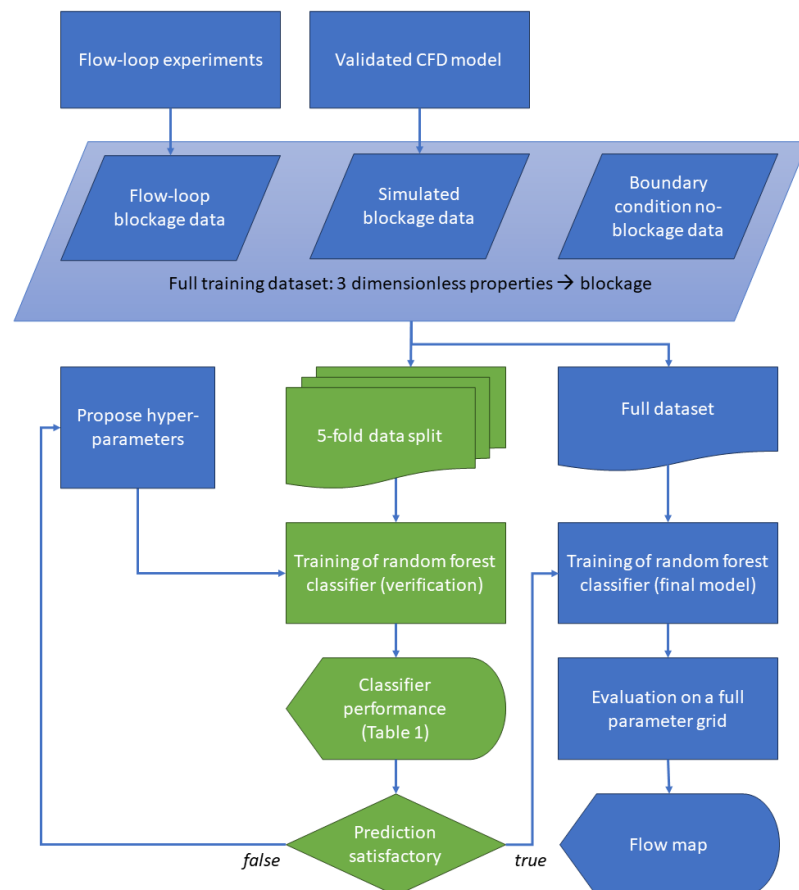


Figure 3. Schematic description of the developed ML model.

2. Results

2.1. Experiments and CFD-DEM model

An example of the experimental log is presented in Figure 2(right) in terms of the history of flow velocity. The plot shows that the velocity gradually reduced until the plugging condition. There were several significant steps of the velocity reduction. This is related to the propagation of particulate slugs, which were formed due to the accumulation

of particles in quiescent zones of the flow loop. Depending on the set point, the duration of the plugging process in different experiments was in the interval 50...1000 s. The experimental results for various flow conditions are summarized in Figure 5, where the flow map of plugging is presented in terms of flow Reynolds number and the concentration of particles. A referent flow map from similar experiments of Hirochi et al.[14] is shown in the figure. As follows from the map, plugging happened when the concentration of particles was above 14%, and the Reynolds number below 10000. These values differ from Hirochi et al.[14] as ice particles in decane are more cohesive than ice particles in an aqueous media, as considered in the referent study. There were also untypical cases where the plugging was registered at low concentrations and high Re. These plugging events, labelled separately in the figure, are attributed to the blockage of clearances in the pump.

The CFD-DEM model was validated against the experimental logs; an example of the validation plot is shown in Figure 2(right) for different values of c_r . As shown by Saparbayeva and Balakin, [15] and presented in the figure, the best match of the experiment is found for $c_r=0.88$. The model does not entirely reproduce the stepwise drops of the flow velocity as it does not replicate the entire flow loop with places where the particle slugs are formed. After the validation, the CFD-DEM model produced new points for the flow map (Figure 5). The model data correspond to the experimental dataset. Additional simulations were carried out to test how the process is sensitive to variation of γ_{ice} . This was done by altering the dimensionless granular capillary number $Ca = v\mu/\gamma_{ice}$, where v is the mean flow velocity, μ is the viscosity of the continuous phase, and γ_{ice} is the cohesive surface energy of the ice particles. In the simulations, the capillary number was in the range from 0.001 to 0.003.

2.2. Machine learning

2.2.1. Dataset

Using the classifier, we predicted the presence of blockages across a range of parameter conditions. In this figure, we present an array of process conditions at which the classifier forecasts plugging events. The contrast between the plugging and non-plugging conditions defines boundaries where blockages occur, as depicted in Figure 4. At lower concentrations, up to about 15%, the boundary appears around a Reynolds number of 10,000. Later, as concentrations increase, this boundary reduces. Figure 4 shows that the model predicted blockades at high Re and low particle concentrations. This happens because the imported dataset contains several specific experimental data points with high Reynolds numbers that indicate the cases when the pump of the flow loop experienced blockage.

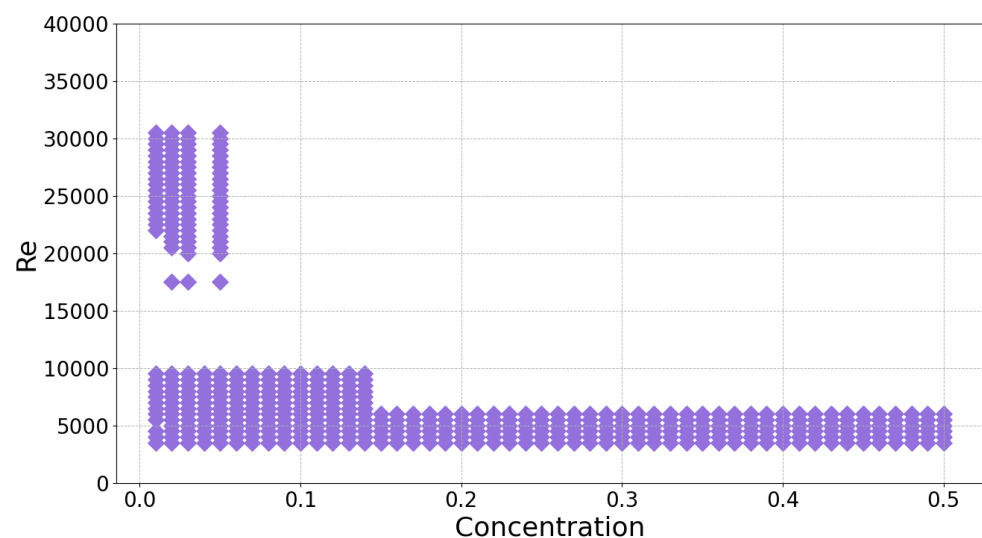


Figure 4. ML-predicted process conditions resulted with plugging. Intermediate result produced from the original dataset.

2.2.2. Validation

Our accuracy evaluation analyzed key performance measures, including precision, recall, and F1-score. The results are presented in table 1, with accuracy scores ranging from 0, indicating the worst, to 1, indicating the best accuracy. Precision represents the proportion of true positive predictions among all positive predictions made by the classifier. Recall measures the proportion of true positive predictions among all actual positive cases. The F1-score is the harmonic mean of precision and recall, providing a balanced assessment of the classifier's performance. As demonstrated in Table 1, all of these measures show notably high values for both cases, whether with or without blockage. The case without blockage exhibited a minimum recall value of 0.80 and a maximum precision value of 1, while the blockage case achieved a maximum recall value of 1. The F1-score for both cases is high, indicating that the classification model performs well. These metrics collectively demonstrate the effectiveness of the chosen method.

Table 1. Summary of random forest classifier performance.

Case	Precision	Recall	F1-score
No Block	1.00	0.80	0.89
Block	0.96	1.00	0.98

2.2.3. Results

Figure 5 represents a flow map by Hirochi et al. [14] in comparison with a representation of the three blockage boundaries predicted by the classifier, as well as experimental [13] and simulation data points. The boundaries of the ML-predicted plugging regimes are presented as in Figure 4. We have excluded an unphysical boundary showing blockage at high Reynolds numbers for the flow map construction. Four data points from the imported dataset discussed earlier in Figure 4 were excluded for the training of the final version of the ML model. Furthermore, we presented three different results for machine learning lines corresponding to changes in cohesion. As depicted in the figure, the scaling of the cohesive surface energy by factors 0.5 and 0.8, and the respective increase of the granular capillary number, lower the boundary predicted by the machine learning model. An interesting observation is that the upper limit set by the machine learning classifier closely aligns with the line when the Reynolds number is around 10^4 . This alignment is particularly in line with the upper boundaries observed in CFD-DEM simulations and experimental results. We also point out that the isolines of cohesion set horizontal at the concentrations above 15% which might not be entirely realistic as more particles might enhance plugging and thus lift the boundary as in Hirochi et al. [14]. This artifact is related to the fact that the training dataset was limited by 15% due to the experimental limitations and enhanced computational costs in the CFD-DEM model.

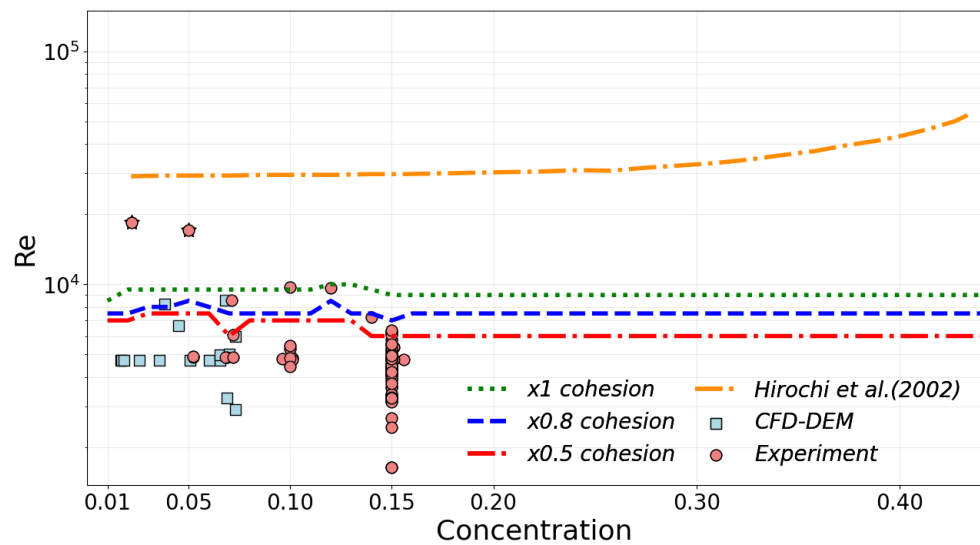


Figure 5. Flow map from the random forest classifier with three different cohesion values. The datapoints in the plot represent experimental [13] and the CFD-DEM cases where the blockage was detected. Experimental points excluded from training are labeled with star-like markers. Flow map from Hirochi et al. [14] shown for comparison. The lines present the boundaries of the plugging regime predicted by the ML-model and shown in Hirochi et al. [14].

It has to be noted that the time spent for every CFD-DEM case was about 3.0 hours when running on 30 cores AMD Ryzen Threadripper RO 3975WX (3.8 GHz), and a typical plugging experiment was run for 2.5-4.0 hours. The ML code was significantly faster, returning the entire flow map within 10 s of physical time using an ordinary laptop (Intel Core i5-1235U).

3. Conclusions

In this study, we applied the machine-learning tool, a random forest classifier, to predict the occurrence of blockage caused by cohesive particles in the multiphase flow loop. Our methodology combined experimental data from flow loop experiments and CFD-DEM simulations to train a predictive model. Evaluating the model's performance using precision, recall, and F1-score metrics showed its high accuracy in blockage prediction in given conditions, demonstrating a maximum precision score of 1 for the blockage case and 0.96 for the case without.

As the important contribution of the study, we presented the flow map detailing comparisons between the machine-learning predictions, CFD-DEM simulations, and experimental data. Our multi-parameter ML model allowed us to extend traditional flow maps to assess the blockage boundary's sensitivity to changes in cohesion. The secondary contributions include the developed ML methodology, the code, and the databases (available upon request).

The methodology's success highlights the potential for further advancements in predictive modelling. Exploring advanced machine learning techniques, refining datasets, and incorporating real-time data can lead to models capable of predicting and preventing blockages in diverse and dynamic flow systems.

Author Contributions:

Conceptualisation, data curation, formal analysis, investigation, methodology, and writing—original draft, N.S.; Investigation, methodology, experiments, editing, P.S.; Supervision, conceptualisation, data curation, formal analysis, investigation, methodology, software and writing—original draft, B.B.; Supervision, resources, conceptualisation, data curation, formal analysis, investigation, methodology, writing—review and editing, S.A.; Supervision and editing, T.R. All authors have read and agreed to the published version of the manuscript.

Funding:

This project was supported by the Research Council of Norway (project 300286).

Data Availability Statement:

The datasets used and/or analysed during the current study are available from the corresponding author on reasonable request.

References

1. Lal, B.; Bavoh, C.B.; Sayani, J.K.S. *Machine Learning and Flow Assurance in Oil and Gas Production*; Springer Nature, 2023.
2. Manikonda, K.; Hasan, A.R.; Obi, C.E.; Islam, R.; Sleiti, A.K.; Abdelrazeq, M.W.; Rahman, M.A. Application of Machine Learning Classification Algorithms for Two-Phase Gas-Liquid Flow Regime Identification. In Proceedings of the Abu Dhabi International Petroleum Exhibition and Conference. SPE, 2021, p. D041S121R004.
3. Hasan, A.R.; Kabir, C.S.; Sarica, C.; et al. *Fluid flow and heat transfer in wellbores*; Society of Petroleum Engineers Richardson, Texas, 2018.
4. Alhashem, M. Machine learning classification model for multiphase flow regimes in horizontal pipes. In Proceedings of the International Petroleum Technology Conference. IPTC, 2020, p. D023S042R001.
5. Chaari, M.; Seibi, A.C.; Hmida, J.B.; Fekih, A. An optimized artificial neural network unifying model for steady-state liquid holdup estimation in two-phase gas-liquid flow. *Journal of Fluids Engineering* **2018**, *140*, 101301.
6. Qin, H.; Srivastava, V.; Wang, H.; Zerpa, L.E.; Koh, C.A. Machine learning models to predict gas hydrate plugging risks using flowloop and field data. In Proceedings of the Offshore technology conference. OTC, 2019, p. D011S010R003.
7. Evans, J.H. Dimensional analysis and the Buckingham Pi theorem. *American Journal of Physics* **1972**, *40*, 1815–1822.
8. Wang, J.; Wang, Q.; Meng, Y.; Yao, H.; Zhang, L.; Jiang, B.; Liu, Z.; Zhao, J.; Song, Y. Flow characteristic and blockage mechanism with hydrate formation in multiphase transmission pipelines: In-situ observation and machine learning predictions. *Fuel* **2022**, *330*, 125669.
9. Muller, A.C.; Guido, S. *Introduction to machine learning with Python*; O'Reilly, 2017.
10. Kim, J.; Han, S.; Seo, Y.; Moon, B.; Lee, Y. The development of an AI-based model to predict the location and amount of wax in oil pipelines. *Journal of Petroleum Science and Engineering* **2022**, *209*, 109813.
11. Amar, M.N.; Ghahfarokhi, A.J.; Ng, C.S.W. Predicting wax deposition using robust machine learning techniques. *Petroleum* **2022**, *8*, 167–173.
12. Ahmadi, M. Data-driven approaches for predicting wax deposition. *Energy* **2023**, *265*, 126296.
13. Struchalin, P.G.; Øye, V.H.; Kosinski, P.; Hoffmann, A.C.; Balakin, B.V. Flow loop study of a cold and cohesive slurry. Pressure drop and formation of plugs. *Fuel* **2023**, *332*, 126061.
14. Hirochi, T.; Yamada, S.; Shintate, T.; Shirakashi, M. Ice/water slurry blocking phenomenon at a tube orifice. *Annals of the New York Academy of Sciences* **2002**, *972*, 171–176. <https://doi.org/10.1111/j.1749-6632.2002.tb04569.x>.
15. Saparbayeva, N.; Balakin, B.V. CFD-DEM model of plugging in flow with cohesive particles. *Scientific Reports* **2023**, *13*, 17188.
16. Saparbayeva, N.; Chang, Y.F.; Kosinski, P.; Hoffmann, A.C.; Balakin, B.V.; Struchalin, P.G. Cohesive collisions of particles in liquid media studied by CFD-DEM, video tracking, and Positron Emission Particle Tracking. *Powder Technology* **2023**, p. 118660.
17. Yang, S.o.; Kleehammer, D.M.; Huo, Z.; Sloan, E.; Miller, K.T. Temperature dependence of particle-particle adherence forces in ice and clathrate hydrates. *Journal of Colloid and Interface Science* **2004**, *277*, 335–341. <https://doi.org/10.1016/j.jcis.2004.04.049>.
18. Saeys, Y.; Abeel, T.; Van de Peer, Y. Robust feature selection using ensemble feature selection techniques. In Proceedings of the Machine Learning and Knowledge Discovery in Databases: European Conference, ECML PKDD 2008, Antwerp, Belgium, September 15-19, 2008, Proceedings, Part II 19. Springer, 2008, pp. 313–325.
19. Qi, Y. Random forest for bioinformatics. *Ensemble machine learning: Methods and applications* **2012**, pp. 307–323.
20. Menze, B.H.; Kelm, B.M.; Masuch, R.; Himmelreich, U.; Bachert, P.; Petrich, W.; Hamprecht, F.A. A comparison of random forest and its Gini importance with standard chemometric methods for the feature selection and classification of spectral data. *BMC bioinformatics* **2009**, *10*, 1–16.
21. Pedregosa, F.; Varoquaux, G.; Gramfort, A.; Michel, V.; Thirion, B.; Grisel, O.; Blondel, M.; Prettenhofer, P.; Weiss, R.; Dubourg, V.; et al. Scikit-learn: Machine Learning in Python. *Journal of Machine Learning Research* **2011**, *12*, 2825–2830.